Using biophysical analysis to study the regulation of the budding yeast kinetochore

Emily A. Scarborough

A dissertation

submitted in partial fulfillment of the

requirements for the degree of

Doctor of Philosophy

University of Washington

2019

Reading Committee:

Trisha N. Davis, Chair

Charles L. Asbury

Peter S. Brzovic

Program Authorized to Offer Degree:

Biochemistry

University of Washington

Abstract

Using biophysical analysis to study the regulation of the budding yeast kinetochore

Emily A. Scarborough

Chair of the Supervisory Committee:
Trisha N. Davis, Professor and Chair
Department of Biochemistry

Kinetochores are large macromolecular machines that serve to physically segregate the genomic material of a cell during mitosis. To achieve this, the kinetochore must make strong attachments to dynamic microtubules under force for long periods of time, but also be able to correct erroneous attachments. These complicated tasks require exquisite regulation within the kinetochore. The flexible outer kinetochore complex Ndc80 is essential to all of these functions. Previous studies have primarily focused on posttranslational modifications that affect regulation of the complex. I sought to determine how additional kinetochore components might regulate the microtubule binding capacity of the *Saccharomyces cerevisiae* Ndc80 complex, as well as if the complex's intrinsic flexibility (conformational changes) affects its function.

I and a previous member of the lab initially found that the conserved MIND complex, a central kinetochore component, and the Ndc80 complex are connected by an extensive network of contacts: an individual MIND complex enhances the microtubule-binding affinity of a single Ndc80 complex by fourfold. However, MIND binds Ndc80 complex far from the microtubule-binding domain. In addition, MIND activation is redundant with the effects of a mutation in Ndc80 that might alter its ability to adopt a tightly bent conformation. From these results, I hypothesized a previously unidentified allosteric mechanism for regulating microtubule binding

of an outer kinetochore component by a central kinetochore complex: the binding of MIND opposes the tightly bent (auto-inhibited) form of the Ndc80 complex, stabilizing the complex in a more open conformation which results in better microtubule binding.

To more directly test this hypothesis, I developed a single molecule FRET assay to examine conformational changes of the complex while simultaneously monitoring its microtubule-binding activity. I uncovered a novel mechanism of regulation of the Ndc80 complex that is intrinsic to its structure; tight bending of the complex inhibits its microtubule binding. I showed that the Ndc80 complex can fluctuate between straight and bent forms, and that binding of the complex to microtubules selects for straightened forms. In addition, the kinetochore complex MIND enhances microtubule binding by opposing the auto-inhibited conformation of Ndc80 complex. I suggest that prior to its assembly at the kinetochore, the Ndc80 complex interchanges between bent (auto-inhibited) and open conformations. Once assembled, its association with MIND stabilizes the Ndc80 complex in a straightened form for higher affinity microtubule binding.

TABLE OF CONTENTS

List of Figures

List of Tables

ACKNOWLEDGEMENTS

I would like to thank Dr. Trisha Davis for giving me independence and autonomy during my graduate career, yet always providing support, advice, and most importantly, positivity, when experiments became challenging. I would like to thank Dr. Eric Muller for his thought-provoking questions during lab meetings and continual enthusiasm in lab. I thank Dr. Charles Asbury for always being available to act as a co-mentor, his willingness to spend hours coding software for me, and showing me the importance of carefully crafted scientific writing. I would like to thank the Davis lab members as a whole for creating a positive scientific environment that encourages questions and asking help from others. I would like to especially thank Kim Fong for answering endless questions of mine in lab and listening to any and all of my stresses and neuroticisms during graduate school, and Jae ook Kim, King Yabut and Luke Helgeson for becoming good friends in and outside of lab. In addition to Jae ook Kim, classmates Brantley Coleman and Mark Kanow provided an initial support system in graduate school consisting of dark jokes, morbid humor and a reminder to not take things too seriously. Though my family really has no idea of what I do, I thank them for always being supportive and proud of my journey. Finally, I thank my boyfriend, Piero Lamelza, for most of my accomplishments in graduate school. From spending hours with me in cafes while studying for my general exam, to traveling to lab with me on the weekends, to listening to me complain and stress and cry when life became overwhelming, Piero made sure that I never suffered alone, all while balancing his own life in graduate school. More importantly, I always had someone to laugh with over really, really stupid stuff.

DEDICATION

To my good friend:

You made my experience in graduate school better in every single way.

Chapter 1. INTRODUCTION

1.1 A Brief History of Cell Division

Over 350 years ago, the natural philosopher Robert Hooke published a scientific bestseller where he coined the term "cell" to describe the repeating honeycomb shape he observed when looking at plant matter under a microscope (Hooke, 1665). This idea of a single, repeating unit within a living organism helped to lay the groundwork for future seminal ideas: the concept that cells are the basic unit of life (Schwann & Schleiden, 1847) and the discovery that the origin of cells is a result of the division of pre-existing cells (Remak R. Untersuchungen über die Entwicklung der Wirbeltiere. Berlin: G. Reimer; 1855). Eventually, the German biologist Walther Flemming used the word "mitosis" (from the Greek word for thread, due to the thread-like nature of the DNA as cells divide) to describe cell division (Flemming, 1882). He carefully characterized this process and observed many phenomena that we still know to be true today, such as the "doubling" of chromosomes when they appear in prophase (Flemming, 1882). Around the same time, Charles Darwin and Gregor Mendel both published their theories of evolution and inheritance, yet it was not until the early 1900s that Theodor Boveri and Walter Sutton formulated the chromosome theory of inheritance to offer a mechanistic explanation of the theories, finally providing insight into the importance of faithful chromosome segregation. The study of mitosis spans hundreds of year, but initial work was limited by its reliance on simple observations of cells. Recent advances in scientific instrumentation and tools, coupled with a push toward inter-disciplinary research, have resulted in a greater understanding of the mechanisms of cell division. However, many unknowns still persist.

1.2 MITOSIS

The cell cycle is a universal biological process that both duplicates a cell's genetic material and divides it equally between two daughter cells. Eukaryotes and prokaryotes, though they share little by way of cellular structure or complexity of DNA, share some cell cycle similarities (Margolin & Bernander, 2004). One of the more visually striking parallels occurs during M (mitotic) phase in eukaryotes, when chromosomes segregate to opposite poles. Recent evidence has shown that bacteria also use cytoskeletal elements to actively segregate genomic material to opposite ends of the cell during cell division (Polka, Kollman, Agard, & Mullins, 2009). In eukaryotes, this cytoskeletal machine driving chromosome segregation is called the mitotic spindle.

The mitotic spindle is a complex 3D structure (Fig. 1.1). Microtubules emanate from a microtubule-organizing center (MTOC) and attach to the DNA of the cell in order to pull it to opposite poles. The MTOC is responsible for organization and nucleation of microtubules and contributing to cell cycle timing. In animal cells, the MTOC is called the centrosome and is comprised of two centrioles deposited in an amorphous proteinaceous mass (Sapp, 1998). The budding yeast centrosome, called the spindle pole body, on the other hand, is a highly defined structure with layered plaques (Viswanath et al., 2017). Though structurally dissimilar, both the centrosome and spindle pole body are functionally equivalent (Gräf, 2018). Wacław Mayzel and Otto Bütschli originally observed the mitotic spindle in living cells, even before the term "mitosis" was conceived (Bütschli, 1876; Mayzel, 1875). The main conclusions of their work were drawn from fixed samples of cells, providing a static image of what we now know to be a highly dynamic process.

Microtubules are one of the principal components of the eukaryotic cytoskeleton, and thus, the mitotic spindle: they are cylindrical, polarized polymers that can contain anywhere from 11-15 protofilaments, growing up to many micrometers in length. The protofilaments are comprised of heterodimers containing α and β tubulin. Tubulin dimers hydrolyze GTP to GDP after addition to the growing microtubule lattice, which weakens affinity for adjacent dimers and favors disassembly (Chrétien, Fuller, & Karsenti, 1995; Mandelkow, Mandelkow, & Milligan, 1991). Microtubules undergo dynamic instability; this refers to the stochastic switch between the growing phase (through the addition of tubulin dimers) and the shrinking phase, or catastrophe (due to the loss of tubulin multimers, presumably) (Mitchison & Kirschner, 1984). The "minus end" is relatively stable, whereas the "plus end" is highly dynamic—the minus end is most commonly found at the MTOC (Doxsey, 2001). This persistent dynamicity creates a challenging scenario for the cell whereby chromosomes must stay attached to these microtubules for long periods of time (nearly one hour in HeLa cells). Large multi-protein structures called kinetochores mechanically attach the chromosomes of the cell to the microtubules within the mitotic spindle during this process.

1.3 The Budding Yeast Kinetochore

As previously highlighted, distantly related organisms share common characteristics of the cell cycle (e.g. actively partitioning the genome using the cytoskeleton). Independent of its ease of genetic manipulation, budding yeast is an exceptional model organism for studying mitosis because many proteins and complexes involved are highly conserved up to humans. Furthermore, budding yeast has the unique advantage in that only one microtubule attaches to one kinetochore, which greatly simplifies the system (Winey et al., 1995). In humans, up to 20 microtubules can attach to a single kinetochore (Rieder, 1982). For these reasons, we use

Saccharomyces cerevisiae as a model system, and thus, will focus on details specific to the budding yeast kinetochore.

The budding yeast kinetochore is an enormous macromolecular machine at a size of greater than 5 megadaltons, comprised of more than 40 proteins partitioned into distinct complexes (Biggins, 2013) (Fig. 1.2, Table 1.1). The kinetochore must coordinate these complexes to carry out vital functions during mitosis: tune microtubule-binding affinity when appropriate, bear load under force to maintain strong attachments to the microtubule and correct erroneous attachments. How all the parts of the kinetochore are coordinated to enact these complicated functions *in vivo* is an active area of research.

In budding yeast, the kinetochore assembles on a 125 base pair point centromere. Assembly begins with Cse4 (CENP-A), a histone H3 variant (Furuyama & Biggins, 2007). Cse4 incorporation within the chromatin requires the histone chaperone Scm3 (Shivaraju, Camahort, Mattingly, & Gerton, 2011). Scm3 interacts with CBF3, a complex that directly engages with the conserved centromeric DNA region CDEIII, which may explain the specificity of deposition of Cse4 only at centromeres (Camahort et al., 2007). The inner kinetochore then builds upon this foundation: 13 proteins aptly named "constitutive centromere associated network" (CCAN), and one additional protein, Mif2 (CENP-C) (Biggins, 2013). These complexes remain stably bound to the centromere throughout the course of mitosis, and the kinetochore only completely disassembles for a brief time in S phase, when DNA is replicated. Only Ame1, Okp1 and Mif2 are essential within the budding yeast inner kinetochore (Biggins, 2013). The specific roles of the other inner kinetochore proteins are less clear.

1.4 The Budding Yeast Outer Kinetochore

The budding yeast outer kinetochore contains those complexes essential for its microtubule binding ability. The flexible heterotetrameric complex, Ndc80, is primarily responsible for the microtubule binding and is highly conserved from yeast to humans (McCleland et al., 2003; Wang et al., 2008) (Fig. 1.3, Table 1.1). The yeast and human Ndc80 complex (comprised of the Ndc80 protein, Nuf2 protein, Spc24 protein and Spc25 protein) contains two important sites of interactions for microtubules: the disordered N-terminal tail of the Ndc80 protein and dual calponin homology (CH) domains located in the Ndc80/Nuf2 globular head (Alushin et al., 2012; Lampert, Mieck, Alushin, Nogales, & Westermann, 2013). The Ndc80 complex is a hub within the entire kinetochore, involved in all of its vital functions (Etemad, Kuijt, & Kops, 2015; Powers et al., 2009; Umbreit et al., 2012). There are numerous binding partners that interact with the complex, as well as multiple regulatory mechanisms, such as posttranslational modifications, to control its activity *in vivo* (Akiyoshi, Nelson, Ranish, & Biggins, 2009; Ciferri, Musacchio, & Petrovic, 2007; Zaytsev et al., 2015; Zhao et al., 2018). It has been observed *in vitro* that the budding yeast Ndc80 complex binds to stabilized microtubules for short periods of time and is diffuse on the lattice, though *in vivo*, it specifically binds the plus-ends of microtubules for long periods of time (Powers et al., 2009). This difference may highlight that additional factors and regulation exist in the cell that increase the affinity of the Ndc80 complex to microtubules.

The Dam1 complex is also found in the budding yeast outer kinetochore. Though only present in fungi, it is thought to be functionally homologous to the Ska complex in humans (van Hooff, Snel, & Kops, 2017). The decameric Dam1 complex assembles up to 16 copies to form oligomeric rings around the microtubule, while simultaneously binding the Ndc80 complex (Janke, Ortíz, Tanaka, Lechner, & Schiebel, 2002; Wang et al., 2007). It is generally accepted

that three sites of interaction exist between the Dam1 ring and the Ndc80 complex, but the exact stoichiometry (one vs. two rings per Ndc80 complex) is still debated (Aravamudhan, Goldfarb, & Joglekar, 2015; Joglekar, Bloom, & Salmon, 2009; Kim et al., 2017).

The yeast MIND complex exists as a bridge between those kinetochore components that directly bind DNA and those that directly bind the microtubule. It is comprised of four proteins (Mtw1, Dsn1, Nnf1 and Nsl1), forming a Y-shaped complex roughly 20 nm in length (Maskell, Hu, & Singleton, 2010). Within the "Y," a disordered tail on the one arm binds the other arm to auto-inhibit binding to the inner kinetochore until relieved through phosphorylation (Akiyoshi, Nelson, & Biggins, 2013; Dimitrova, Jenni, Valverde, Khin, & Harrison, 2016b). The bottom of the stalk of the "Y" directly binds the Ndc80 complex, and all eight proteins in both complexes form a stable 1:1 co-complex that can be purified through size exclusion chromatography (Kudalkar et al., 2015).

1.5 Diseases of Cell Division and Kinetochores

While studying mitosis using sea urchin embryos, Boveri noted that an abnormal number of chromosomes in cells (aneuploidy) appeared to be detrimental for the cell and the overall health of the organism (Boveri, 1902). He postulated that aneuploidy might be a contributing factor to tumorigenesis and cancer. Roughly one hundred years later, this hypothesis solidified into a concrete idea: that genome instability somehow aids in enabling cells to acquire the characteristics of cancer cells (Hanahan & Weinberg, 2011). Yet, even still, it is greatly debated what precisely is the relationship between aneuploidy and cancer (Naylor & van Deursen, 2016). The study of cell division is inextricably intertwined in this debate—we must understand how cells are able to accurately segregate genomic material before we can understand how they make mistakes in the process. The literature on mitosis and cancer is vast and exhaustive, largely

driven by the huge burden of cancer on human health (Brown, Lipscomb, & Snyder, 2001; Levine & Holland, 2018). In the brief following paragraphs, some more unique and novel human disorders related to errors in cell division are described.

Microcephaly and other disorders of growth have been previously characterized as defects in cell division (Papi et al., 1989). Originally, only mutations in centrosomal proteins were implicated in disease pathogenesis (Saade, Blanco-Ameijeiras, Gonzalez-Gobartt, & Martí, 2018). More recently, studies have identified additional mutations in kinetochore proteins that also result in primary growth failures. KNL1, CENP-E and CENP-T are all proteins of the human kinetochore that have been linked to causative mutations for primary microcephaly (KNL1) and primordial dwarfism (CENP-E and CENP-T) (Hung et al., 2017; Mirzaa et al., 2014; Omer Javed et al., 2018). However, it remains unclear how mutations in ubiquitously expressed proteins promote gross growth defects in only certain tissues, like the brain in microcephaly. Recent studies have aimed to answer this question. At least in the case of KNL1, it appears that disease mutations in the protein (which generate an alternative splice site) only lead to reduced protein levels (and consequently increased rates of aneuploidy) in neural progenitor cells, but not fibroblasts or neural crest cells. Neural progenitor cells have higher levels of splicing machinery, providing a possible explanation of why microcephaly is the only major phenotype of patients with this KNL1 mutation (Omer Javed et al., 2018).

Mosaic variegated aneuploidy (MVA) syndrome (OMIM 257300) is a rare recessive autosomal disorder caused by mosaic aneuploidy in cells. The syndrome is characterized by severe microcephaly, short stature and growth defects, physical and eye abnormalities and intellectual and developmental disability. Risk of cancer is also increased in these patients. Studies have shown that mutations in the spindle checkpoint protein BubR1 result in decreased

protein levels and consequently, abolishment of the checkpoint mechanism: cells progress through mitosis, regardless if all sister chromatids are properly attached and bioriented (Hanks et al., 2004; Matsuura et al., 2006). Interestingly, the fact that these patients are also at an increased risk of cancer supports the idea that aneuploidy is causative of cancer.

Though aneuploidy is generally thought to be only maladaptive for the cell (an-eu comes from the Greek language for "not good," after all), studies have shown that non-diseased human and mouse brain tissue have a high proportion of aneuploid mitotic and postmitotic neurons (Kingsbury, Yung, Peterson, Westra, & Chun, 2006; Rehen et al., 2001). It has been speculated that this cellular diversity in the developing brain leads to the necessary plasticity of complex functions, such as learning. Orchestrated aneuploidy has also been found to be present in the normal developing liver (Duncan et al., 2012). The model suggests that the selection of specific aneuploid karyotypes can result in an adaptive advantage when the liver is under chronic stress. It still remains unclear, and contested, whether aneuploidy has the potential to play positive roles in certain cellular contexts. Perhaps the brain and liver are anomalous outliers or, they hint at another beneficial side, of "incorrect" chromosome segregation (Knouse, Wu, Whittaker, & Amon, 2014). Ultimately, many mysteries persist in how errors in chromosome segregation result in specific human diseases.

1.6 Single Molecule Techniques

Biophysics is a discipline that aims to bridge the fields of physics and biology, applying the principles of physics to biological phenomena. In the following chapters, a variety of biophysical techniques are used to probe the mechanisms underlying the kinetochore-microtubule interface.

Carl Zeiss and Carl Reichart developed fluorescence microscopy at the beginning of the 20th century (Renz, 2013). Since the cloning of green fluorescent protein (GFP) in the early

1990s (and eventually many other spectral variants), development of microscopy techniques has exploded (Kremers, Gilbert, Cranfill, Davidson, & Piston, 2011; Prasher, Eckenrode, Ward, Prendergast, & Cormier, 1992). Total internal reflection fluorescence (TIRF) is a type of microscopy which exploits the difference in index of refraction between the glass (coverslip) and water (buffer/solution) (AMBROSE, 1956; Martin-Fernandez, Tynan, & Webb, 2013). When the angle of the laser light is directed at the coverslip such that it exceeds the critical angle, all light is completely reflected and an evanescent field of light is created over the coverslip, illuminating roughly 100 nm into the solution. Thus, only the fluorescent molecules very close to the coverslip are excited, and all others in solution are dark, greatly reducing background and enabling the tracking of individual fluorescence species (AMBROSE, 1956). This technique is used in Chapters 2 and 3 to measure the residence time of individual kinetochore components on stabilized microtubules.

Theodor Förster published his first paper on energy transfer in 1946, though foundational groundwork involving understanding of quantum mechanics and electromagnetism was laid beginning in the 1800s and early 1900s (Sun, Wallrabe, Seo, & Periasamy, 2011). Jean-Baptiste Perrin and his son first explained the process of energy transfer of two molecules in solution due to dipole-dipole interactions, but it was Förster who established the correct range of distances at which this energy transfer occurred and the equations to quantitatively describe the process. Thus, Förster resonance energy transfer (FRET) is a highly sensitive method to measure distances between fluorophores, and consequently, the biological molecules tagged by those fluorophores. Fluorophores generally have the potential to exhibit energy transfer when the emission spectrum of the donor molecule has significant overlap with the absorption spectrum of the acceptor molecule. FRET is amenable to both *in vivo* experiments and *in vitro* experiments

(in bulk and single molecule). In Chapter 3, FRET is combined with TIRF microscopy in order to measure intra-complex interactions of a single kinetochore complex *in vitro*. In Chapter 4, *in vivo* FRET is used to characterize the interactions of kinetochore components in live budding yeast.

Arthur Ashkin won the 2018 Nobel Prize in Physics for his invention of optical tweezers in the 1970s, a method that uses focused laser beams to manipulate micrometer-sized particles in 3-D (Ashkin, 1970). The highly focused lasers create an electric field at the "beam waist," i.e. the narrowest part of the laser beam, that attracts dielectric objects (such as polystyrene beads or cells) (Neuman & Block, 2004). Since then, optical tweezers have been used in numerous applications: to measure swimming force of sperm, to measure unfolding of proteins, and to measure force generation and motility of molecular motors (Block, Goldstein, & Schnapp, 1990; Kellermayer, Smith, Granzier, & Bustamante, 1997; Tadir et al., 1989). During mitosis, kinetochores and sister chromatids are under tension when properly aligned during metaphase. Thus, one measurable function of kinetochore complexes is their ability to bear load under force. Optical tweezers are able to measure force at the level of piconewtons, comparable to the magnitude of force a kinetochore and its components would experience in a cell (Chacón, Mukherjee, Schuster, Clarke, & Gardner, 2014). In Chapter 2, this technique is used to characterize and measure the load-bearing capabilities of budding yeast kinetochore components.

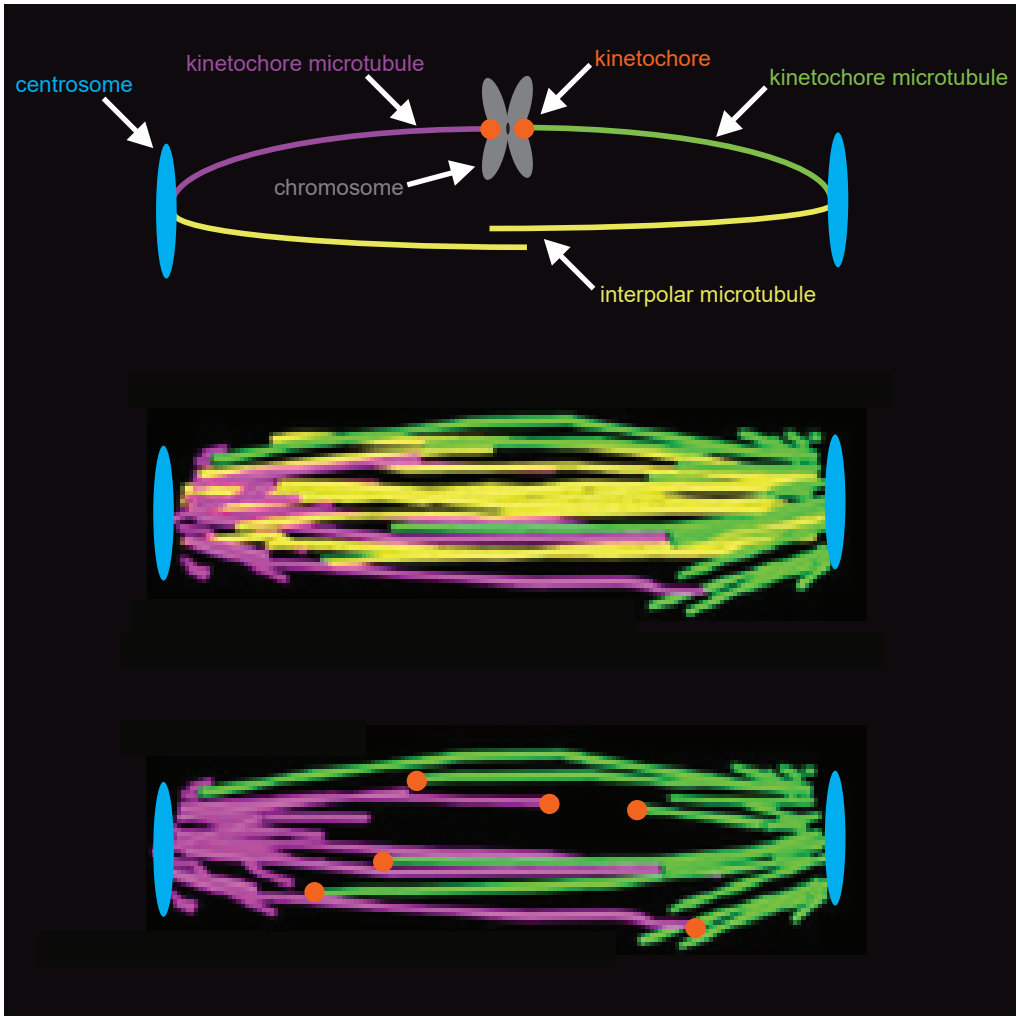

Figure 1.1. The yeast mitotic spindle is a complex molecular machine.
(Top) Cartoon of main components of the yeast mitotic spindle. Colors correspond to the 3-D electron tomography reconstructions of a yeast spindle below. (Middle) 3-D electron tomography reconstruction of a wild type yeast mitotic spindle, including interpolar microtubules. Figure adapted from (Nannas, O'Toole, Winey, & Murray, 2014). Spindle pole bodies (turquoise ellipses) are added for illustrative purposes. (Bottom) 3-D electron tomography reconstruction of the same wild type yeast mitotic spindle as above, excluding interpolar microtubules. Figure adapted from (Nannas et al., 2014). Kinetochores (orange balls) are added for illustrative purposes.

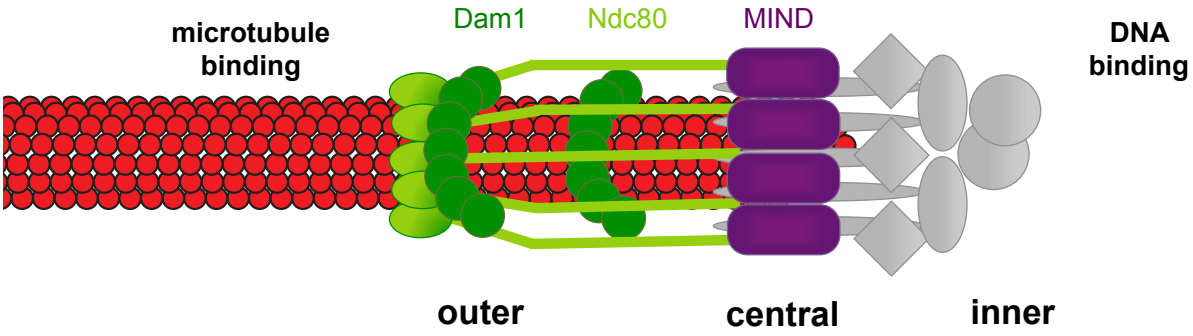

Figure 1.2. Hypothetical structure of a budding yeast kinetochore.
Cartoon detailing the hypothetical structure of a budding yeast kinetochore tip-bound to a microtubule (red). Outer kinetochore components are shown in green, central kinetochore components are shown in purple. Inner kinetochore components are shown in gray and unlabeled. Figure adapted from (Biggins, 2013).

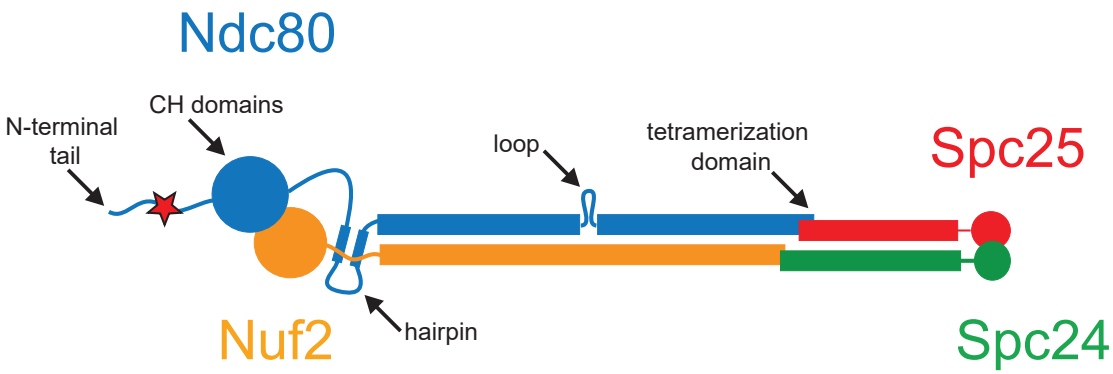

Figure 1.3. Architecture and key features of the Ndc80 complex.
Diagram of the Ndc80 complex. Black arrows point to key features of the Ndc80 complex, most which are involved in *in vivo* regulation of the complex or are interactions sites for binding partners. Red star on the N-terminal tail indicates general location of key phosphorylation sites that regulate the complex's microtubule binding.

Table 1.1. Subcomplexes and proteins within the yeast kinetochore

Yeast kinetochore subcomplex	Protein	Yeast kinetochore subcomplex	Protein
Dam1	Dam1	CCAN	Ctf19
	Duo1		Okp1
	Ask1		Mcm21
	Spc19		Ame1
	Spc34		Iml3
	Dad1		Chl4
	Dad2		Nkp1
	Dad3		Nkp2
	Dad4		Mcm16
	Hsk3		Ctf3
Ndc80	Ndc80		Mcm22
	Nuf2		Mhf1
	Spc24		Mhf2
	Spc25	Mif2	Mif2
MIND	Mtw1	Nucleosome	Cse4
	Nnf1		Hta2
	Nsl1		Htb2
	Dsn1		Hht1
Cnn1	Cnn1		Hhf1
	Wip1	Cbf3	Cbf2
Spc105	Spc105		Cep3
	Kre28		Ctf13
			Skp1
		Cbf1	Cbf1

Chapter 2. THE CENTRAL KINETOCHORE COMPONENT MIND INCREASES THE MICROTUBULE BINDING OF THE NDC80 COMPLEX[1]

2.1 INTRODUCTION

During mitosis, kinetochores coordinate the movement of replicated chromosomes into two daughter cells and ensure that the genome is equally segregated upon division. Kinetochores maintain a grip on dynamic microtubules that are constantly growing and shortening, and they also ensure that each chromatid is properly attached to microtubules emanating from only one pole. These attachments must be strong enough to withstand the mechanical tension associated with bipolar chromosome alignment, and yet they must be quickly released in response to signals that detect improper attachments (Biggins, 2013; Cheeseman, 2014). Each kinetochore is a macromolecular structure composed of 40 different types of proteins assembled into repeating subcomplexes that span from the centromeric DNA to the microtubule (Biggins, 2013). There is an intrinsic hierarchy, with few DNA-binding elements expanding out to multiple microtubule attachment complexes (Joglekar, Bouck, Molk, Bloom, & Salmon, 2006; Johnston et al., 2010). How subcomplexes are held together and function as a cohesive molecular unit is unclear. Assembling kinetochore proteins *in vitro* allows us to map their interconnectivity and directly probe how each component contributes to microtubule attachment strength. By systematically rebuilding a kinetochore *in vitro*, we aim to gain a clear understanding of force transmission throughout the kinetochore and to discern the precise role of each component in kinetochore function.

[1] This section is closely adapted from the published paper (Kudalkar et al., 2015). This section is based off of a project in collaboration with a previous Davis lab member, Emily Kudalkar.

Previous work focused on characterization of individual and combined activities of the outer microtubule-binding kinetochore complexes (Biggins, 2013; Cheeseman, 2014). How central kinetochore complexes contribute to establishing and maintaining microtubule attachment is less clear. Work from *Caenorhabditis elegans* identified a conserved core microtubule-binding "KMN" network composed of Knl1/Spc105, Mis12/MIND (Mtw1, Nsl1, Nnf1, Dsn1) complex, and Ndc80 (Ndc80, Nuf2, Spc24, Spc25) complex (Cheeseman, Chappie, Wilson-Kubalek, & Desai, 2006). *In C. elegans*, the 4-protein Ndc80 complex and Knl1 bind directly to microtubules, but MIND does not. Instead, MIND serves as a structural linker that connects DNA-binding components with the microtubule-binding complexes (Obuse et al., 2004; Screpanti et al., 2011). The KMN complex binds microtubules with a higher affinity than Ndc80 complex or Knl1 alone, demonstrating that MIND can facilitate the synergistic binding of outer kinetochore complexes. This finding highlighted the importance of cooperation between kinetochore complexes and suggested that central complexes can enhance kinetochore–microtubule attachment indirectly by acting through the microtubule-binding components. However, the mechanisms underlying this enhancement remain unknown.

Two hypotheses can explain how a central kinetochore complex could increase the microtubule binding activity of an outer kinetochore component. One possibility is that the outer kinetochore component oligomerizes to increase avidity. Another possibility is that the central kinetochore component induces structural changes in the outer component that enhance its binding to microtubules. Although MIND has been shown to enhance the microtubule binding of Knl1 in co-sedimentation assays (Cheeseman et al., 2006), this method cannot distinguish which mechanism is responsible. Whether MIND can similarly affect the Ndc80 complex (Ndc80c) by either mechanism has not been tested.

Within the kinetochore, outer components are present in higher copy numbers relative to central components, suggesting that oligomerization may be a mechanism to enhance microtubule binding. Additionally, substantial evidence suggests that the outer kinetochore Ndc80 complex undergoes conformational changes throughout mitosis (Aravamudhan, Felzer-Kim, Gurunathan, & Joglekar, 2014; Joglekar et al., 2009; Tien et al., 2014). The budding yeast Ndc80 complex hinges about a flexible "loop" region and exists in both a folded conformation and an elongated state, as measured using fluorescence microscopy and observed in negative stain electron micrographs (Joglekar et al., 2009; Wang et al., 2008). *In vivo* evidence supports the physiological significance of these conformational changes, underscoring the importance of different conformations of the Ndc80 complex (Maure et al., 2011; Tien et al., 2014). However, it is unknown whether these structural changes correlate with changes in microtubule affinity. The Ndc80 complex also interacts with a second kinetochore receptor, CENP-T/Cnn1 (Bock et al., 2012; Nishino et al., 2013; Rago, Gascoigne, & Cheeseman, 2015; Schleiffer et al., 2012). It is unclear how central kinetochore components influence the activity of the Ndc80 complex throughout mitosis.

Here, we have reconstituted the *Saccharomyces cerevisiae* MIND–Ndc80 (MN) co-complex using recombinant yeast components and have used cross-linking analysis to identify a network of interactions between the two complexes that is more extensive than previously recognized. Using single-molecule fluorescence microscopy, we found that MIND enhances the microtubule-binding activity of the Ndc80 complex. This enhancement does not require oligomerization of the Ndc80 complex. Instead, a single MIND complex binds a single Ndc80 complex far from its microtubule-binding domain and confers increased microtubule interaction of the co-complex. In addition, MIND activation is redundant with the effects of a mutation in

Ndc80 that hinders its ability to adopt a folded conformation, suggesting that MIND might promote an unfolded conformation of Ndc80 complex with higher affinity for microtubules. Finally, we used optical tweezers to show that the MIND–Ndc80 linkage can support the high levels of tension generated by the components of the kinetochore–microtubule interface, establishing the MIND complex as a key component of the force transmission pathway within the kinetochore.

2.2 Materials and Methods

Protein Expression and Purification.

Dsn1-His_6–tagged MIND complex was expressed from a polycistronic pRSF vector in BL21 cells and induced with 0.2 mM isopropyl β-D-1-thiogalactopyranoside (IPTG) for 14 h at 20 °C. Cells were lysed with a French press, and MIND-His was purified via a Ni-charged IMAC resin column (Bio-Rad) in 50 mM $NaPO_4$, 200 mM NaCl, pH 7.0, supplemented with protease inhibitors (Roche), 5 mM imidazole, and 1 mM PMSF, and then washed and eluted with 300 mM imidazole. The MIND complex was purified using a Superdex 200 column (GE Healthcare), and concentration was measured by bicinchoninic acid (BCA) (Sigma). For TIRF assays, Mtw1-GFP–tagged MIND complex was purified via a His_6-tag on Nnf1 as described previously in this section. Mtw1-SNAP–tagged Nnf1-His_6–MIND complex was expressed and purified as described previously in this section. The MIND–SNAP complex was labeled with SNAP-Surface 549 dye (New England Biolabs) at a 2:1 dye:protein molar ratio overnight at 4 °C. His_6-tagged Ndc80 and His_6-tagged Ndc80-121 complex were expressed and purified as described (Tien et al., 2014; Wei, Sorger, & Harrison, 2005). FLAG-Spc24 Ndc80 complex was expressed similarly to His_6-tagged complex, lysed using a French press in 50 mM Hepes, 200 mM NaCl,

pH 7.6, and bound to anti-FLAG M2 affinity gel (A2220; Sigma). The affinity gel was washed, and protein was eluted with 0.1 mg·mL^{-1} 3X FLAG Peptide (F4799; Sigma). The Ndc80–FLAG complex was purified using a Superdex 200 size exclusion column (GE Healthcare). The MIND/Ndc80 co-complex was prepared by combining nickel-purified MIND–His_6 and Ndc80–His_6 complexes in a 2.5:1 molar ratio and incubating for 15 min at room temperature. MIND-GFP/Ndc80-FLAG co-complex was prepared similarly. All resulting MIND/Ndc80 co-complexes were subsequently purified with a Sepharose 400 size exclusion column (GE Healthcare) in 50 mM $NaPO_4$, 100 mM NaCl, pH 7.0.

Velocity Sedimentation.

Sucrose gradients [5–30% (wt/vol)] were generated by layering 250 μL of 5%, 13.8%, 21.6%, and 30% sucrose in 50 mM $NaPO_4$, 100 mM NaCl, pH 7.0, and allowing a continuous gradient to form for 3 h at 4 °C. Then 1–2 μM purified MIND-His_6 and Ndc80-His_6 complex were mixed at 1:1 molar ratio for 15 min at room temperature before loading onto gradient. Reactions were ultracentrifuged at 166,000 × g at 4 °C for 5 h, and 16–18 sequential fractions were collected and analyzed by SDS/PAGE, staining with Coomassie Blue. Sedimentation coefficients were determined by comparing to elution of known standard proteins (BSA, catalase, and aldolase).

Plasmid Shuffle Assay.

Endogenous NSL1 or MTW1 was deleted in a diploid strain of *Saccharomyces cerevisiae* with a KanMX cassette and then transformed with a WT copy of NSL1 or MTW1 under its endogenous promoter on a URA3 plasmid. Cells were sporulated, and haploids were selected. Haploids containing both KanMX and URA3 markers were transformed with a WT or mutated gene (nsl1-4D or mtw1-220) under its endogenous promoters on a LEU2 plasmid. Positive colonies were

selected on SD-Leu for 3 d at 30 °C. Individual clones were grown to log phase in SD-Leu media and then plated in 10-fold dilutions on synthetic complete and 1 mg·mL^{-1} 5-FOA plates. Growth was assessed after 48 h at 30 °C.

Cross-Linking of Recombinant MIND/Ndc80 Complex and Mass Spectrometry Analysis.

The MIND/Ndc80 co-complex (26 μg in 133 μL of either 100 mM NaCl or 300 mM NaCl, 50 mM $NaPO_4$ buffer, pH 7) was cross-linked for 2 min at room temperature with disuccinimidyl suberate (0.3 mM final; Pierce). The reaction mix was quenched with 10 μL of 500 mM NH_4HCO_3, and the buffer was exchanged to HB500 (40 mM Hepes, 500 mM NaCl, pH 7.5) using protein desalting spin columns (Pierce) according to the manufacturer's protocol. Cross-linked proteins were subsequently reduced with 10 mM DTT for 30 min at 37 °C, alkylated with 15 mM iodoacetamide for 30 min at room temperature, and digested with trypsin (at a substrate to enzyme ratio of 60:1) overnight at room temperature with shaking. Samples were acidified with 5 M HCl and stored at −80 °C.

Samples (0.75 μg) were loaded onto a fused-silica capillary tip column (75-μm i.d.) packed with 40 cm of Reprosil-Pur C18-AQ (3-μm bead diameter; Dr. Maisch). Peptides were eluted from the column at 250 nL·min^{-1} using a gradient of 2–35% acetonitrile (in 0.1% formic acid) over 120 min, followed by 35–60% acetonitrile over 10 min. Mass spectrometry was performed on a Q-Exactive (Thermo Scientific), operated using data-dependent acquisition where a maximum of six MS/MS spectra were acquired per MS spectrum (scan range of m/z 400–1,600). At m/z 200, the resolution for MS and MS/MS was 70,000 and 35,000, respectively.

Cross-linked peptides were identified using the Kojak cross-link identification software (www.kojak-ms.org). The results of Kojak were exported directly to Percolator to produce a

statistically validated set of cross-linked peptide identifications at a false discovery rate threshold of 5% (Sarangapani, Akiyoshi, Duggan, Biggins, & Asbury, 2013).

Immunoprecipitation.

Anti-FLAG M2 affinity gel (Sigma) was prepared according to the manufacturer's instructions and then incubated with purified 600 nM Ndc80c–FLAG complex for 1 h at 4 °C. Beads were subsequently washed 3 × 5 min with Tris-buffered saline (TBS) plus 0.1% Nonidet P-40, and 1 μm Dsn1-His_6–tagged purified MIND complex was added. Reactions were incubated for 1 h at 4 °C and washed 3 × 5 min with TBS plus 0.1% Nonidet P-40. Protein was eluted with 50 μL of TBS plus 0.1 $mg{\cdot}mL^{-1}$ 3X FLAG peptide (Sigma) at room temperature for 30 min with gentle agitation. Eluate was removed and boiled with sample buffer and then run on SDS/PAGE and subjected to Western blot analysis using anti-His (Genscript) and anti-Ndc80 (a gift from Arshad Desai, Ludwig Cancer Research Center, University of California, San Diego). Total MIND complex binding was measured using Dsn1-His_6 band intensity normalized over Ndc80 band intensity for each reaction. Binding of mutant MIND complexes to the Ndc80 complex was calculated as a percentage of WT MIND complex binding.

TIRF Microscopy.

Custom instrumentation and flow cells were prepared as previously described (Gestaut, Cooper, Asbury, Davis, & Wordeman, 2010; Powers et al., 2009). For assays, coverslips were rinsed twice with ddH_20 and then incubated with "rigor" kinesin in standard BB80 assay buffer (80 mM PIPES [piperazine-N,N′-bis(2-ethanesulfonic acid)], pH 6.9, 1 mM $MgCl_2$, 1 mM EGTA, 8 $mg{\cdot}mL^{-1}$ BSA) for 5 min (Rice et al., 1999). Alexa Fluor-568–labeled taxol-stabilized bovine microtubules were adhered to coverslips and rinsed with BB80. All protein complexes were

purified via gel filtration before TIRF microscopy. Dilutions of the protein complex of interest in BB80 supplemented with 1 mg·mL^{-1} κ-casein and oxygen scavengers (200 μg·mL^{-1} glucose oxidase, 35 μg·mL^{-} catalase, 25 mM glucose, 5 mM DTT) were flowed in and immediately imaged. GFP and Alexa Fluor-568 channels were imaged simultaneously using a cooled camera (iXon 887-BI; Andor) at 10 frames·s^{-1} for 200 s. Controls assaying MIND-GFP alone, Dam1c alone, and Dam1c-GFP plus MIND maintained the same TIRF microscopy assay conditions as the experimental assays. Dam1c-GFP and MIND were combined immediately before imaging.

For imaging at 37 °C, an objective heater controller (Bioptechs Inc.) was used. Flow cells were preheated to 37 °C for at least 5 min before flowing in protein and imaging as described previously in this section. Type 37 immersion oil was used to compensate for the change in temperature. The laser power of the GFP channel was increased 2.7-fold to maintain the same GFP brightness as 25 °C reactions.

For disassembling microtubule assays, solutions were prepared as in ref. (Tien et al., 2010). Briefly, flow cells were washed and prepared with rigor kinesin as described previously in this section and then Alexa Fluor-568–labeled GMPCPP microtubule seeds were bound to coverslips and washed with BB80. Microtubule growth buffer (BB80 with 1 mM GTP and oxygen scavengers) containing ~2 mg·mL^{-1} Alexa Fluor-647–labeled tubulin was introduced to the chamber and incubated with seeds for 10 min until extensions were present. The protein of interest was then introduced in BB80 with 1 mg·mL^{-1} κ-casein and oxygen scavengers, and imaging began immediately as the microtubules depolymerized upon buffer exchange.

TIRF Microscopy Analysis.

Single-particle tracking and analysis were done using custom Labview (National Instruments) and Igor Pro (Wavemetrics) software as previously described (Gestaut et al., 2010; Powers et al.,

2009). Briefly, kymographs were generated from 2,000-frame movies, and individual events were traced recording tracking position, total binding time, and GFP fluorescence. Binding events lasting less than 0.2 seconds or exhibiting a fluorescence signal less than 20% over background noise were excluded from analysis. Bootstrapping analysis was used to determine mean residence time and the error of the mean. The mean squared displacement of each complex was plotted against time, and a one-dimensional diffusion constant was calculated using a weighted linear fit. Histograms of GFP fluorescence intensity were generated and fit with a Gaussian to determine average fluorescence of single particles.

Microtubule tip-tracking analysis was performed by overlaying kymographs of GFP and 647 channels and then measuring the distance of GFP-particle tracking using Photoshop (Adobe).

Optical Trapping Bead Motility Assay.

Streptavidin-coated 0.44-μm polystyrene beads were coated with biotinylated anti-His_5 (Qiagen) and 11-pM beads were incubated with 40 nM His_6-tagged Ndc80 or MIND complex as described such that each bead was decorated with ~1,800 protein complexes (Franck, Powers, Gestaut, Davis, & Asbury, 2010; Umbreit et al., 2012; Umbreit et al., 2014). Flow cells were prepared using double-sided tape and plasma-cleaned coverslips and incubated with 30 μL of 1 $mg{\cdot}mL^{-1}$ biotinylated BSA (Vector Laboratories) for 10 min at 50 °C, followed by BRB80 (80 mM PIPES, pH 6.9, 1 mM $MgCl_2$, 1 mM EGTA) wash, 30 μL of 1 $mg{\cdot}mL^{-1}$ avidin DN (Vector Laboratories) for 2 min at room temperature, and another BRB80 wash. GMPCPP biotinylated tubulin seeds in BRB80 were bound for 2 min and washed with 37 °C growth buffer (BB80 plus 1 mM GTP). Protein-coated beads were introduced into the flow chambers in growth buffer with 1.4 $mg{\cdot}mL^{-1}$ tubulin, 200 $\mu g{\cdot}mL^{-1}$ glucose oxidase, 35 $\mu g{\cdot}mL^{-1}$ catalase, 25 mM glucose, 1 mM

DTT. For MIND/Ndc80c assays, His_6-tagged MIND and FLAG-tagged Ndc80 complex were preassembled into a co-complex and subjected to size exclusion gel filtration as described under Protein Expression and Purification. For assays with MIND, Ndc80, and Dam1 complexes, 20 nM His_6-tagged MIND beads were prepared as described previously in this section, and then 40 nM free FLAG-tagged Ndc80 complex and 2 nM free Dam1 complex were added. For controls (i.e., MIND decorated beads with no protein in solution and GFP decorated beads and undecorated beads, both with Ndc80c in solution), all beads and soluble proteins were maintained at the concentrations used in the experimental reactions. For each condition, a bead was manipulated to make contact with a microtubule. If the bead–microtubule contact could not withstand any amount of force, then it was considered to be a nonbinder.

Optical trap assays were performed at 26 °C using custom instrumentation to capture and manipulate beads as described (Franck et al., 2010).

Constant force assays using His_6-Ndc80c beads and MIND-His/Ndc80c-FLAG beads were performed as described (Franck et al., 2010). Then, 2.5 pN of force was applied in the direction of microtubule growth through rounds of assembly and disassembly. Bead position vs. time was analyzed using custom Igor Pro software, and attachment lifetime was calculated. Rupture force assays were performed as described (Akiyoshi et al., 2010; Sarangapani et al., 2013; Tien et al., 2010). Once beads were bound to microtubule tips, a test force of 1 pN was applied, and only beads that tracked with ∼100 nm of tip growth were subjected to ramping force of 0.25 $pN \cdot s^{-1}$ until detachment. Records of force vs. time were collected, and maximum rupture force was determined using custom Igor Pro software.

2.3 RESULTS

The MIND and Ndc80 complexes are connected by an extensive interaction network

To study the interaction between the MIND and Ndc80 complexes in vitro, we assembled a stable MIND–Ndc80 (MN) co-complex with a 1:1 stoichiometry (Hornung et al., 2011; Maskell et al., 2010) (Fig. 2.1 A and Fig. 2.2). By pairing gel filtration and velocity sedimentation experiments, we found that MN exhibits a frictional ratio of 2.7, consistent with its extremely elongated conformation as seen previously by negative-stain electron microscopy (Erickson, 2009; Maskell et al., 2010; Petrovic et al., 2010) (Fig. 2.2).

We generated a comprehensive map of interactions between the two complexes by treating MN with the cross-linking agent disuccinimidyl suberate and identifying the cross-linked peptides by mass spectrometry (Tien et al., 2014) (Fig. 2.1 B). The C-terminal regions of Mtw1, Nsl1, and Dsn1 interface with two highly conserved amphipathic helices of Spc24 (Fig. 2.1 B and C). Specifically, Nsl1 seems to bind a hydrophobic pocket between the α2-helices of Spc24 and Spc25, previously recognized as a putative interaction site (Wei et al., 2006) (orange circles, Fig. 2.1 C) but for which no binding partner had been identified. Mtw1 binds the α1-helix on the opposite side of Spc24, in the same region shown to interact with another Ndc80c receptor, CENP-T/Cnn1 (yellow circle, Fig. 2.1 D. CENP-T/Cnn1 provides an additional pathway of assembly for the Ndc80 complex at the kinetochore. Though this pathway is not essential in yeast, recent research suggests that it might be necessary for viability when the MIND complex pathway is weakened by phosphorylation events (Lang, Barber, & Biggins, 2018; Malvezzi et al., 2013). Because Spc25 contains only three lysines (Fig. 2.1 B), our lysine-specific cross-linker provided limited information about MIND–Spc25 interactions. Previous work identified the C-terminal region of Dsn1 as being important for interaction with Spc24 and

Spc25 and suggested that it also shares the binding site with Cnn1 (Malvezzi et al., 2013; Petrovic et al., 2010). Our cross-linking results support this interaction although we detected far fewer cross-links between Dsn1 and Spc24 than between Nsl1 or Mtw1 and Spc24. Small regions of Nsl1, Mtw1, and Dsn1 also cross-linked to disordered segments of Spc24 (138–154) and Spc25 (128–132) not depicted in the crystal structure (Fig. 2.1 C) (Wei et al., 2006). Our cross-linking analysis demonstrates that, whereas MIND and Cnn1 share an overlapping binding site within the Ndc80 complex, MIND also forms a second distinct connection to Ndc80c.

Using our cross-links as a guide, we generated three sets of mutations within Dsn1, Nsl1, and Mtw1 to determine whether these regions are required to form the MN co-complex (Fig. 2.1 A). Lysines K198, K205, and K207 of Nsl1 lie within a predicted amphipathic helix and displayed multiple cross-links to the Spc24 pocket. Therefore, we mutated hydrophobic residues V199, Y201, V203, and V206 to aspartic acid to disrupt the hydrophobic side of the putative Nsl1 amphipathic helix (nsl1-4D). Second, we truncated the 62 C-terminal residues of Mtw1 (mtw1-220), from which multiple cross-links to Spc24 were identified. Third, we analyzed the effects of the L562D/L563D mutation in Dsn1 (dsn1-2LD) that was previously suggested to disrupt the interaction between the MIND and Ndc80 complexes in vivo (Malvezzi et al., 2013). None of these mutations interfered with the assembly of the MIND complex, as indicated by the normal migration of all three mutant complexes in size-exclusion chromatography experiments (Fig. 2.4).

The ability of mutant MIND complexes to bind the Ndc80 complex was quantified in vitro by immunoprecipitation (Fig. 2.3). Relative to WT MIND, all three mutant versions of the MIND complex were impaired in co-immunoprecipitation with the Ndc80 complex (Fig. 2.3 B, Right). dsn1-2LD was previously shown to cause lethality, and we tested whether nsl1-4D

or mtw1-220 was also detrimental to cell growth (Malvezzi et al., 2013). We deleted the endogenous copy of NSL1 or MTW1 and asked whether a mutated allele (nsl1-4D or mtw1-220) could support growth. Cells containing only nsl1-4D or mtw1-220 alleles failed to grow whereas those also containing WT copies of NSL1 or MTW1 grew normally (Fig. 2.3 C). Thus, the Mtw1 C terminus and a predicted amphipathic helix in Nsl1 are essential for the formation of the MN co-complex. Together, these results reveal an extensive protein interaction network, centered on a conserved binding pocket on the Spc24-Spc25 heterodimer, that connects the MIND and Ndc80 complexes.

MIND Activates Microtubule Binding by Ndc80c via a Mechanism Distinct from Dam1c Activation.

We next used the MIND-GFP/Ndc80 co-complex to determine whether MIND influences the microtubule-binding properties of the Ndc80 complex. The KMN network binds synergistically to microtubules, and MIND can directly affect the activity of Knl1 in vitro (Cheeseman et al., 2006). It is unknown whether MIND can similarly influence the behavior of the Ndc80 complex. In nematodes, the MIND and Ndc80 complexes do not directly interact without Knl1, but they do form a stable co-complex in many other organisms, including yeast and humans (Hornung et al., 2011; Maskell et al., 2010; Petrovic et al., 2010). We therefore assessed how the MIND complex influences Ndc80 complex microtubule binding at the single-molecule level using total internal reflection fluorescence (TIRF) microscopy. As shown previously, Ndc80c-GFP alone has a relatively weak affinity for microtubules and exhibited a mean residence time of 2.5 ± 0.1 s on the microtubule lattice (Powers et al., 2009)(Fig. 2.5 A and B). Previous work found that addition of the 10-member outer kinetochore Dam1 complex increased the residence time of Ndc80c 2.6-fold, to 6.4 ± 0.2 s (Fig. 2.5 A and B) (Tien et al., 2010). Surprisingly, we found that

MIND also dramatically affected the microtubule binding of Ndc80c because the residence time of MIND-GFP/Ndc80c complexes was 10.4 ± 0.6 s, fourfold longer than that of Ndc80c-GFP (Fig. 2.5 B). By contrast, MIND-GFP alone did not interact with microtubules, even when added at high concentrations (Fig. 2.6), indicating that MIND activates the microtubule-binding activity of the Ndc80 complex (Cheeseman et al., 2006). The effects of MIND and Dam1c on the ability of Ndc80c to bind microtubules are additive. The average residence time for MIND-GFP/Ndc80c increases 1.5-fold in the presence of Dam1 complex to 16.5 ± 0.7 s (Fig. 2.5 A and B). This combinatorial effect suggests that Dam1c and MIND influence Ndc80c via independent mechanisms.

The observation that MIND and Dam1c influence Ndc80c independently was further supported by their disparate effects on the motility of Ndc80c along microtubules. MIND showed a milder effect on the diffusion of Ndc80c than does the Dam1 complex (Fig. 2.7). We also found that MIND and Dam1c differ in their ability to enhance the tracking of Ndc80c with disassembling microtubule tips. Dynamic microtubule extensions were assembled off of GMPCPP-stabilized microtubule seeds, and their disassembly was initiated by the removal of free tubulin from solution. Ndc80c-GFP alone tracks poorly with disassembling microtubule ends but can track robustly when artificially oligomerized by antibodies, or in the presence of Dam1c (Powers et al., 2009; Tien et al., 2010) (Fig. 2.8). By contrast, MIND did not enhance the ability of Ndc80c to track disassembling microtubule ends (Fig. 2.8). Therefore, Dam1c and MIND have different effects on the microtubule binding, diffusion, and tip tracking of Ndc80c. These observations indicate that MIND and Dam1c do not simply influence the behavior of Ndc80c by differing degrees, but do so by distinct mechanisms.

The MIND–Ndc80c Interface Can Bear Substantial Levels of Mechanical Load.

In vivo, kinetochores transmit tension from the microtubule interface to the centromeric DNA. Beyond the Ndc80 and Dam1 complexes (Tien et al., 2010), it is not known which kinetochore components participate in the force transmission pathway. We therefore asked whether MIND could directly support mechanical load transmitted through Ndc80c. Indeed, when bound to polystyrene beads via a His tag on MIND, MIND-His/Ndc80c-FLAG was able to couple beads to both assembling and disassembling microtubule tips against an applied load of ∼2.5 pN (Fig. 2.9 A). Beads failed to couple to microtubules against force when decorated with the MIND–His complex in the absence of Ndc80c-FLAG (n = 30). Likewise, no coupling was observed when beads lacking MIND–His were incubated with Ndc80c-FLAG alone (GFP-His–coated beads, n = 79 and uncoated beads, n = 60) (Fig. 2.10). These controls rule out direct microtubule binding by MIND and/or nonspecific adsorption of Ndc80-Flag to the beads. Therefore, the applied load must be transmitted through the MIND–Ndc80c interface. To probe the strength of the MIND–Ndc80 linkage, we used a rupture force assay (Akiyoshi et al., 2010). MIND-His/Ndc80c-FLAG–coated beads were coupled to assembling microtubule tips and briefly subjected to a test force of ∼1 pN. Then, the load was increased at a constant rate (0.25 pN·s^{-1}) until the bead detached from the microtubule. On average, MIND-His/Ndc80c-FLAG–mediated attachments ruptured at 3.8 ± 0.2 pN, comparable with the strength afforded by coupling Ndc80 complex directly to the bead, 4.5 ± 0.2 pN (not significantly different, P = 0.26) (Fig. 2.9 B). When Dam1c-FLAG was added to the assay, the average rupture force of MIND-His/Ndc80c-FLAG beads increased to 9.0 ± 0.6 pN (Fig. 2.9 B). Altogether, these results indicate that the linkage between MIND and Ndc80c can support substantial levels of tension, suggesting that MIND complex is a key participant in force transmission through the kinetochore.

A Single MIND Activates a Single Ndc80 Complex.

The Dam1 and Ndc80 complexes form a unit on microtubules that increases the number of microtubule-binding contacts. Unlike Dam1c, MIND does not form additional direct contacts with the microtubule but instead contributes to microtubule binding indirectly through Ndc80c. How might MIND activate microtubule binding by Ndc80c? One possible explanation is that MIND promotes oligomerization of Ndc80c on microtubules, thereby increasing avidity. MIND could drive oligomerization of Ndc80c by binding two or more Ndc80 complexes and/or by binding other MIND complexes.

First, we tested for oligomerization directly by performing a dual-label TIRF experiment to compare the residence time of GFP-tagged Ndc80 complexes alone to those that colocalized with MIND-SNAP, a MIND complex fused with a small protein which allows for specific, covalent tagging of a fluorescent dye (Alexa Fluor 647) (Fig. 2.11 A-C). By measuring fluorescence intensity, we found that Ndc80c-GFP remained monomeric when alone or bound to MIND-SNAP, but its residence time was significantly increased when in complex with MIND (Fig. 2.11 B and C). Second, we added excess Ndc80c in our TIRF assay in an attempt to both drive the association of MIND with multiple Ndc80c complexes and maximize the occupancy of Ndc80-binding sites within the MIND complex. Supplementing up to a 267-fold molar excess of Ndc80c did not affect the residence time of MN on microtubules (Fig. 2.11 D). Third, under assay conditions where MIND enhanced microtubule binding by Ndc80c, MIND oligomerization was rare; the average fluorescence intensity of GFP-tagged MIND within MN co-complexes bound to microtubules was similar to that of monomeric GFP-tagged Ndc80 complexes (Fig. 2.5 C). Altogether, these data demonstrate that, in our assay, MIND does not enhance Ndc80c

microtubule binding by oligomerization. Instead, a single MIND complex directly enhances microtubule attachment by a single Ndc80 complex.

We hypothesized that MIND induces a conformational change in the Ndc80 complex that favors microtubule coupling by activation of the microtubule-binding domains. The Ndc80 complex binds microtubules primarily through the Ndc80 calponin homology (CH) domains and the Ndc80 N-terminal tail (Fig. 2.12 A) (Alushin et al., 2010; Ciferri et al., 2008; Lampert et al., 2013; Wei, Al-Bassam, & Harrison, 2007). We first tested whether MIND activation requires the N-terminal tail of Ndc80. In our cross-linking analysis, the disordered Ndc80 N-terminal tail interacted with portions of Ndc80, Nuf2, Spc24, and Spc25 (Fig. 2.13 A) (Tien et al., 2014). The presence of the MIND complex reduced cross-linking of the tail, potentially restricting its position in the complex (Fig. 2.13 B). As previously demonstrated, tail-less Ndc80 complex (Δtail-Ndc80c-GFP) bound poorly to microtubules (Lampert et al., 2013; Wei et al., 2007). Due to its extremely short interactions with microtubules at the single-molecule level, we were unable to accurately measure its residence time in the TIRF assay. However, MIND increased the residence time of Δtail-Ndc80c, yielding an average of 5.2 ± 0.7 s, indicating that the tail domain is not required for MIND-mediated enhancement (Fig. 2.11 E).

An alternative possibility is that MIND influences larger scale conformational changes in the Ndc80 complex. We recently identified a temperature-sensitive mutant of Ndc80 (ndc80-121) that harbors two mutations near the loop domain, far from the microtubule and MIND-binding domains (Tien et al., 2014) (Fig. 2.12 A). Based on previous genetic analysis, it was hypothesized that this mutant adopts a conformation at 37 °C that enhances its microtubule binding. Consistent with this view, the Ndc80-121–GFP complex bound at the restrictive temperature (37 °C) to microtubules 1.5-fold longer than the WT complex (Fig. 2.12 B). We then

asked whether MIND can further enhance the ability of the Ndc80-121 complex to bind microtubules by measuring the residence time of a MIND-GFP/Ndc80-121 co-complex via TIRF. MIND-GFP/Ndc80-121c assembled as a stoichiometric complex and exhibited a similar gel filtration profile as MIND-GFP/Ndc80c, indicating that the ndc80-121 mutations did not affect interaction with MIND (Fig. 2.14). At 37 °C, MIND-GFP/Ndc80c also exhibited an average residence time 1.5-fold longer than Ndc80c-GFP alone, similar to the behavior of Ndc80-121–GFP (Fig. 2.12 B). By contrast, MIND did not further enhance the binding of Ndc80-121c; MIND-GFP/Ndc80-121c residence time was indistinguishable from Ndc80-121 complex alone (not significantly different, P = 0.58) (Fig. 2.12 B). These results suggest that both MIND and the ndc80-121 mutations alter the behavior of the Ndc80 complex by the same mechanism, which may involve promoting conformational activation of the Ndc80 complex.

2.4 DISCUSSION

MIND was previously identified as part of the core microtubule-binding KMN network in higher eukaryotes, yet how MIND facilitates microtubule attachment has remained unclear. By reconstituting the yeast MIND/Ndc80 co-complex and using cross-linking analysis, we have identified an intricate set of interactions involving five of the eight proteins within the two complexes. In addition to the previously identified Spc24–Spc25 interface recognized by both MIND and Cnn1, we found a unique connection between Nsl1 and a hydrophobic Spc24/Spc25 cleft (Malvezzi et al., 2013; Nishino et al., 2013). This identification of a second unique interface suggests that the Ndc80 complex may differentially interact with MIND and Cnn1, raising the possibility that each receptor might distinctly regulate Ndc80c function. Furthermore, Nsl1 has been identified as a link between human Mis12 and Ndc80 complexes, and our identification of

its important contribution to the yeast MIND/Ndc80 interface establishes the structural conservation of this connection (Petrovic et al., 2010).

Using single-molecule techniques, we show that the MIND complex promotes the binding of Ndc80c to microtubules. This effect is additive, with the enhancement conferred by the Dam1 complex, providing further evidence that kinetochore components act cooperatively to form robust microtubule attachments. Finally, we demonstrate that the MIND/Ndc80c interface can withstand substantial load, implicating MIND as an integral component of the force transmission pathway of the kinetochore.

How does MIND enhance microtubule attachments? MIND binds Ndc80c far from its microtubule-binding domain (Hornung et al., 2011; Maskell et al., 2010; Petrovic et al., 2010). Consistent with this placement, we show here that MIND does not directly bind microtubules. Furthermore, MIND does not seem to enhance binding by organizing the Ndc80 N-terminal tail domain nor is oligomerization of Ndc80c required. Instead, we demonstrate that an individual MIND complex enhances the microtubule binding of a single Ndc80 complex. We show that MIND binding to the Spc24/Spc25 terminus of the Ndc80 complex confers increased affinity of the microtubule-binding domain.

The Ndc80 complex hinges about a flexible loop region, and in vitro and in vivo evidence supports the existence of both a folded conformation and an elongated state (Joglekar et al., 2009; Wang et al., 2008). Here, we show that a temperature-sensitive NDC80mutant (ndc80-121) that has been previously suggested to affect the stability of a folded complex at 37 °C exhibits increased microtubule affinity at 37 °C compared with the WT complex. Because addition of MIND does not further increase the affinity of the Ndc80-121 complex for

microtubules, MIND and Ndc80-121c increase affinity by a redundant mechanism. We propose that both favor formation of an open, high-affinity conformation of the Ndc80 complex.

The physiological relevance of different conformational states of the Ndc80 complex has remained unclear. Deleting the loop domain of Ndc80 causes lethality, suggesting that flexibility of the complex is necessary in vivo (Maure et al., 2011). Additional in vivo evidence suggests that a folded Ndc80 complex is important during early mitosis whereas an elongated conformation exists at metaphase (Aravamudhan et al., 2014; Joglekar et al., 2009; Tien et al., 2014). We propose that the Ndc80 complex adopts different conformations to modulate the strength of its microtubule attachment. A folded Ndc80 complex that interacts less stably with microtubules might be favorable in prometaphase when erroneous attachments must be corrected by Ipl1/Aurora B kinase (Biggins & Murray, 2001; T. U. Tanaka et al., 2002). The Ndc80 complex adopts an elongated conformation during metaphase, which could promote strong microtubule interaction when kinetochore tension is highest (Joglekar et al., 2009). Folding of the complex at the Ndc80 loop domain positions Spc24 and Spc25 near the microtubule-binding domains of Ndc80, potentially obstructing full contact with microtubules. Indeed, it was previously demonstrated using C. elegans components that the Nuf2/Ndc80 dimer bound more tightly to microtubules than the four-member complex, suggesting intracomplex inhibition (Cheeseman et al., 2006). This autoinhibitory conformation is reminiscent of kinesins and myosin V, which fold into inhibited states that prevent interaction between motor domains and the cytoskeleton in the absence of cargo (Coy, Hancock, Wagenbach, & Howard, 1999; Donovan & Bretscher, 2015; D. S. Friedman & Vale, 1999; Verhey & Hammond, 2009). We propose that MIND binding to Spc24/Spc25 relieves this auto-inhibition via steric hindrance or allosteric

activation, by interfering with the intracomplex interactions that stabilize the folded state of Ndc80c, and thus promotes its binding to microtubules.

Auto-inhibition of the Ndc80 complex could help during S-phase, when premature microtubule binding might interfere with kinetochore assembly. MIND-dependent relief of this auto-inhibition could ensure that Ndc80 is activated only after it is successfully incorporated into the kinetochore. It could also explain why Ndc80 is detected only at the kinetochore whereas other microtubule binding components of the kinetochore are also detected all along the spindle microtubules (He, Rines, Espelin, & Sorger, 2001). Cnn1 provides a distinct Ndc80 receptor during anaphase (Bock et al., 2012; Nishino et al., 2013; Rago et al., 2015; Schleiffer et al., 2012). It will therefore be interesting to learn whether and how Cnn1 affects Ndc80's microtubule affinity.

Altogether, our results highlight the previously unidentified regulation of the microtubule-binding activity of an outer kinetochore component by a central kinetochore complex. We propose that modulating the conformation of microtubule couplers is a way to regulate the strength of microtubule attachments throughout mitosis.

2.5 Acknowledgements

Emily Kudalkar (Mazanka) originally developed and spearheaded this work, as published in (Kudalkar et al., 2015). We thank Andrew Franck, Andrew Powers, Krishna Sarangapani, and Austin Kim for technical assistance and advice. We also thank the members of the T.N.D. laboratory, C.L.A. laboratory, and Seattle Mitosis Club for helpful discussions.

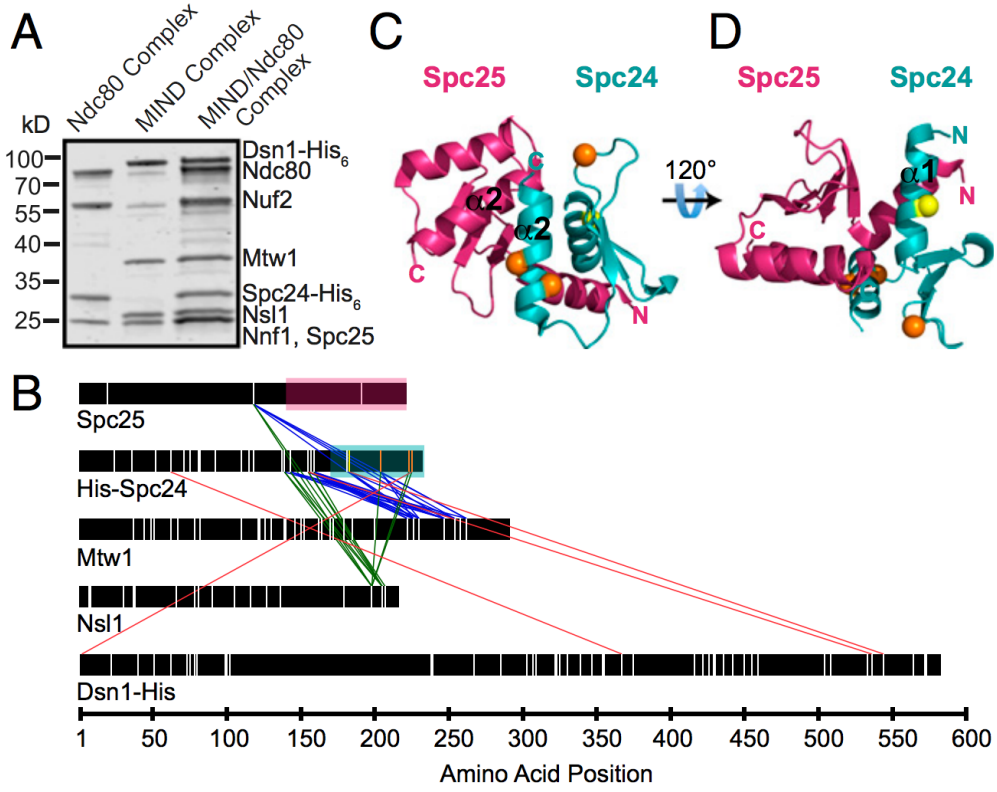

Figure 2.1. Cross-linking analysis identifies previously unidentified regions of interaction between the MIND and Ndc80 complexes.
(A) Coomassie-stained gel showing Ndc80 complex (left lane), MIND complex (middle lane), and MIND/Ndc80 co-complex (right lane). (B) Cross-links between Ndc80 and MIND complexes are shown as colored lines. Lysine residues within each protein are marked as vertical white lines with four exceptions: cross-linked Spc24 lysines highlighted in yellow and orange in C and D are color-coded to match. Regions of Spc25 and Spc24 corresponding to the crystal structure in C and D are highlighted with magenta or teal boxes, respectively. For clarity, only cross-links between Ndc80 complex and MIND are shown; all others are omitted. (C and D) Spc24/Spc25 globular domain crystal structure depicting cross-linked lysines. Spc25 amino acids133–221 are shown in magenta, and Spc24 amino acids 155–213 are shown in teal. Visible N and C termini are marked. (C) The predicted binding pocket for the Ndc80 complex formed by the α2-helices (labeled) of Spc24 and Spc25. Nsl1 cross-links to two lysines (orange) in the Spc24 α2-helix, suggesting it may bind within the hydrophobic pocket. Nsl1 also cross-links to a third lysine (orange) in the disordered Spc24 loop. (D) A 120° rotation of C depicting the lysine residue (yellow) within the α1-helix of Spc24 that cross-links to both Mtw1 and Dsn1.

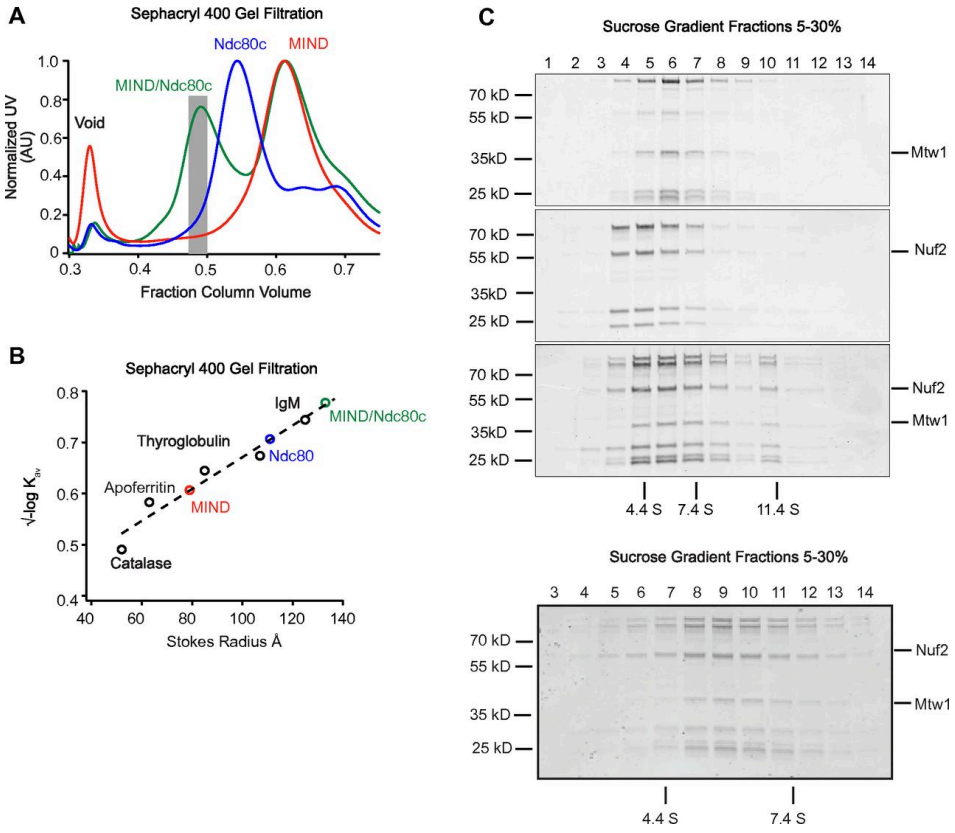

Figure 2.2. MIND/Ndc80c co-complex associates with 1:1 stoichiometry.
(A) Representative Sephacryl 400 gel filtration elution profiles for Ndc80c (green), MIND (blue), and MIND/Ndc80c co-complex (red). Note that, for the MIND/Ndc80c experiment, complexes were mixed in a 2.5:1 molar ratio (MIND:Ndc80c); therefore, excess MIND can be seen eluting as a separate peak. Gray bar indicates fractions pooled and used for subsequent MIND/Ndc80c experiments. (B) Stokes radius vs. √–logKav plotted for indicated standard proteins (catalase, 52 Å; apoferritin, 63 Å; thyroglobulin, 85 Å; fibrinogen, 107 Å; IgM, 130 Å) and fit with a linear regression. Stokes radii for Ndc80c, MIND, and MIND/Ndc80c were calculated using the equation derived from the linear fit: Ndc80c = 111 Å, MIND = 79 Å, MIND/Ndc80c = 134 Å. (C) Velocity sedimentation analysis of Ndc80c, MIND, and MIND/Ndc80c run on a 5–30% sucrose gradient split into 16 sequential fractions; n = 2. Representative elution fractions for each complex across gradient are shown in Coomassie-stained gel; fraction 1 corresponds to the top of the gradient. Some stoichiometric MIND/Ndc80c oligomers are visible in later fractions. BSA (4.4 S), aldolase (7.4 S), and catalase (11.4 S) were run as standards (positions indicated by vertical lines), and a linear fit was determined to find the S values for experimental complexes: Ndc80c = 4.24 S, MIND = 5.42 S, MIND/Ndc80c = 5.89 S. Using the S value and stokes radius, the molecular mass of the MIND/Ndc80c complex was determined to be 331.8 kDa, within 0.04% of the expected molecular mass of a stoichiometric MIND/Ndc80c complex (333 kDa). The frictional ratio of MIND/Ndc80c was also calculated using the S value and stokes radius. MIND/Ndc80c exhibits a frictional ratio of 2.7, indicating that it is highly elongated. (Below) A sucrose gradient from a repeat experiment split into 18 sequential fractions to more clearly visualize the MIND/Ndc80c peak centered at 5.89 S.

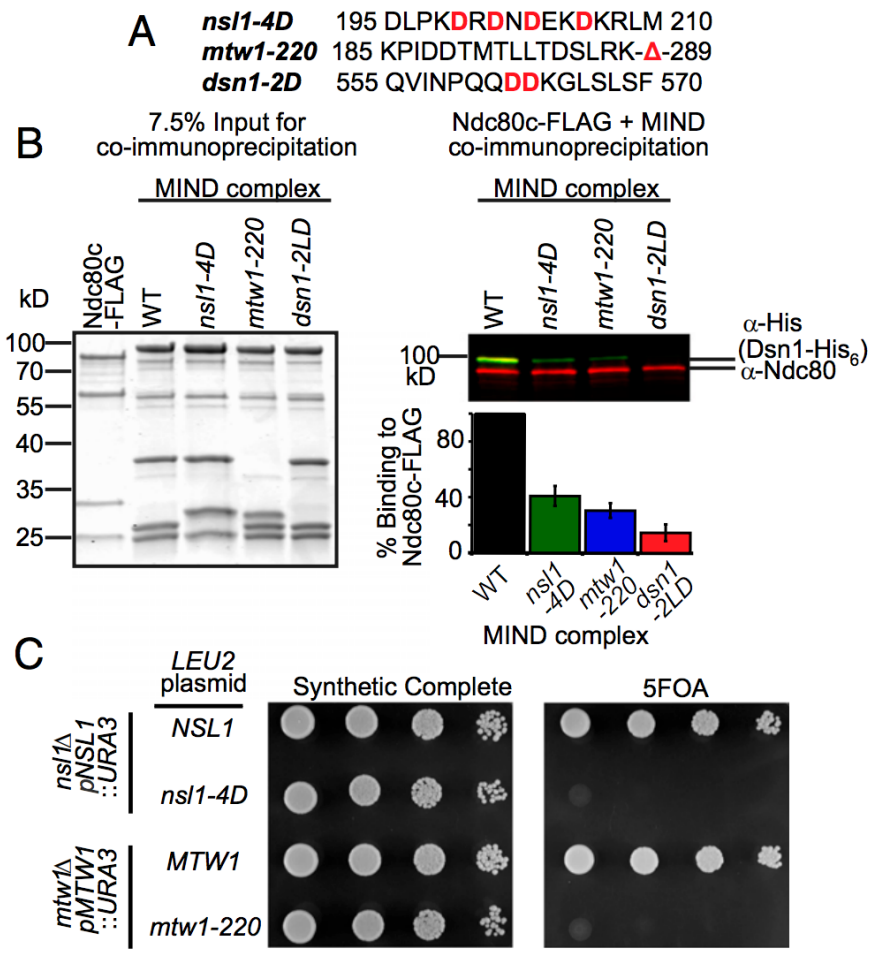

Figure 2.3. The Mtw1 C terminus and a putative alpha-helix in Nsl1 are required for in vitro binding to the Ndc80 complex and are essential in vivo. (A) MIND complex protein sequences, with mutated amino acids shown in red. (B) Immunoprecipitation assays with FLAG–Ndc80 complex immobilized on antiFLAG beads and the indicated MIND–His6 complexes (WT, nsl1-4D, mtw1- 220, and dsn1-2LD) added in solution. (Left) Coomassie-stained gel shows 7.5% input of protein complexes used in immunoprecipitation. (Right) Western blot of immunoprecipitation assay. Copurifying MIND complex was visualized by anti-His (staining Dsn1-His6, green); Ndc80 complex was detected with anti-Ndc80 (red). (Below Right) Quantification of immunoprecipitation experiments. WT MIND binding was normalized to 100% for each experiment, and MIND mutant binding is shown as a percentage of WT binding (n = 2 and error bars denote SEM.) (C) Plasmid shuffle assay of cells spotted in 10-fold dilutions on synthetic complete (SC) media (Left) or SC media supplemented with 5-FOA (Right). (Top spots) nsl1Δ cells containing WT NSL1 on a URA3 plasmid and either WT or nsl1-4D on a LEU2 plasmid. WT NSL1 fully supports growth on 5-FOA media whereas nsl1-4D is lethal. (Bottom spots) mtw1Δ cells with WT MTW1 on a URA3 plasmid and either WT or mtw1-220 on a LEU2 plasmid. mtw1-220 cannot support growth on 5-FOA whereas MTW1 is viable.

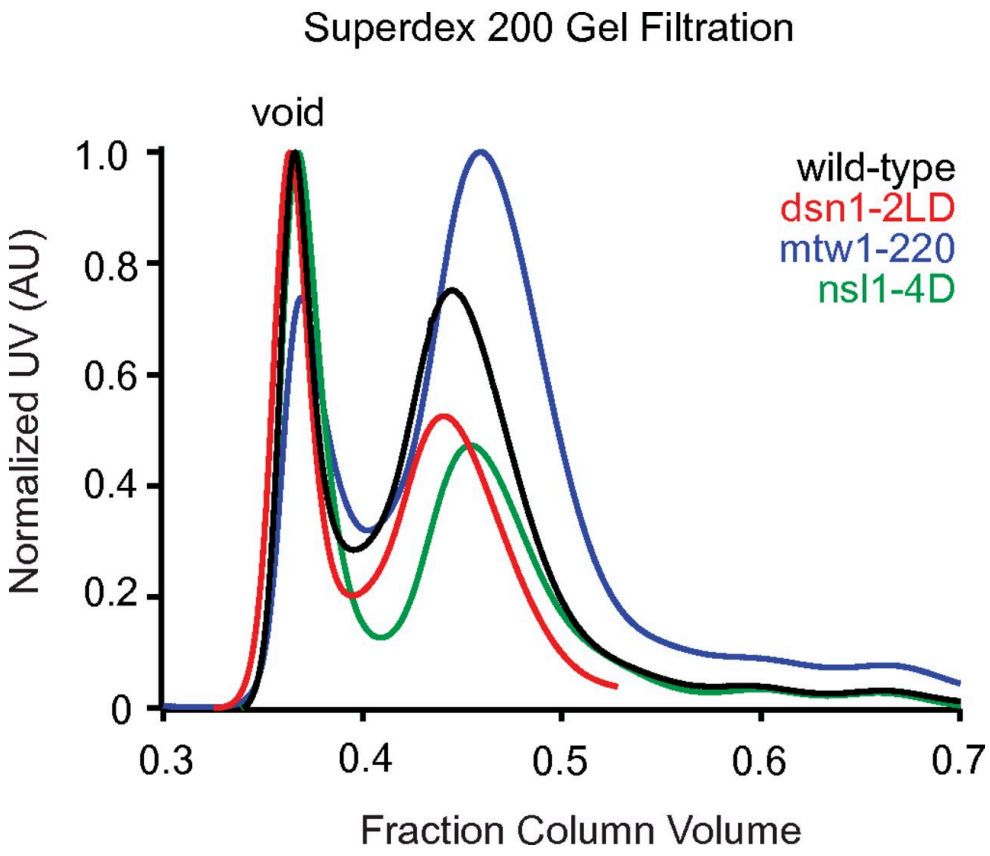

Figure 2.4. Gel filtration profiles of MIND complex mutants.
Gel filtration elution profiles of MIND–His complex mutants run on a Superdex 200 column. Each complex elutes as a distinct peak (wild-type, black; dsn1-2LD, red; mtw1-220, blue; nsl1-4D, green).

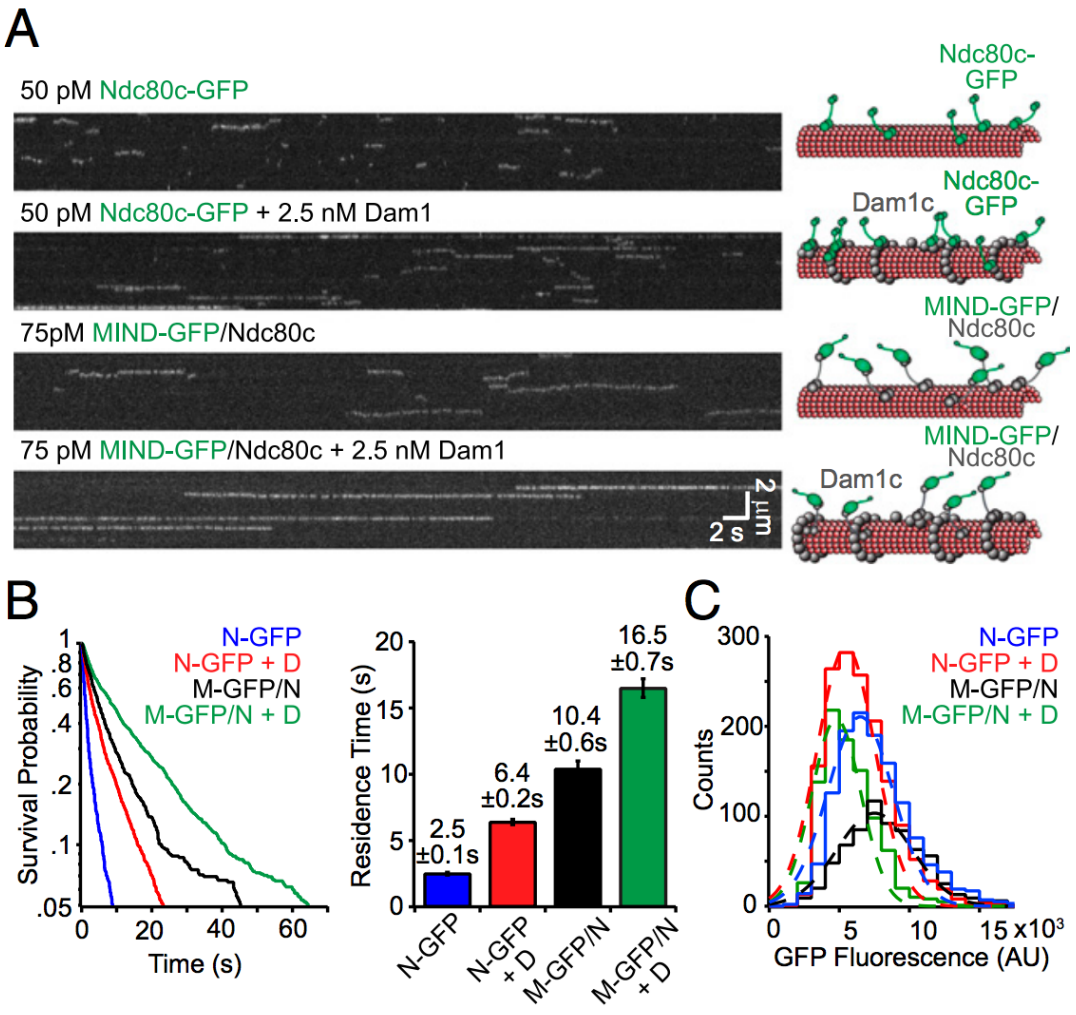

Figure 2.5. MIND and Dam1c individually and additively enhance the binding of Ndc80 complex to microtubules.

(A) Representative TIRF kymographs of Ndc80c-GFP, Ndc80c-GFP plus Dam1c, MIND-GFP/Ndc80c, and MIND-GFP/ Ndc80c plus Dam1c. Concentrations are noted and scale bars are indicated in white. Diagrams on right denote each GFP tagged complex (green) and untagged complex (gray) binding to microtubules (red) in kymograph on left. (B, Left) Survival probability vs. time is plotted for each complex, quantified from individual binding events. Ndc80c-GFP (N-GFP, n = 1,278), Ndc80c-GFP + Dam1c (N-GFP + D, n = 1,525), MIND-GFP/Ndc80c (M-GFP/N, n = 706), and MIND-GFP/Ndc80c + Dam1c (M-GFP/N + D, n = 924). (Right) Average residence time for each complex derived from distribution on left; error bars denote SD. (C) GFP fluorescence distribution for each GFP-tagged complex shown as histograms. Gaussian fits are shown with dotted lines and used to quantify the mean GFP fluorescence for each complex. The number of events is the same as in B. The mean fluorescence values for each complex are as follows: N-GFP = 7,000 ± 2,300 arbitrary units (AU), N-GFP + D = 6,000 ± 2,100 AU, M-GFP/N = 8,000 ± 2,700 AU, M-GFP/N + D = 5,300 ± 1,800 AU.

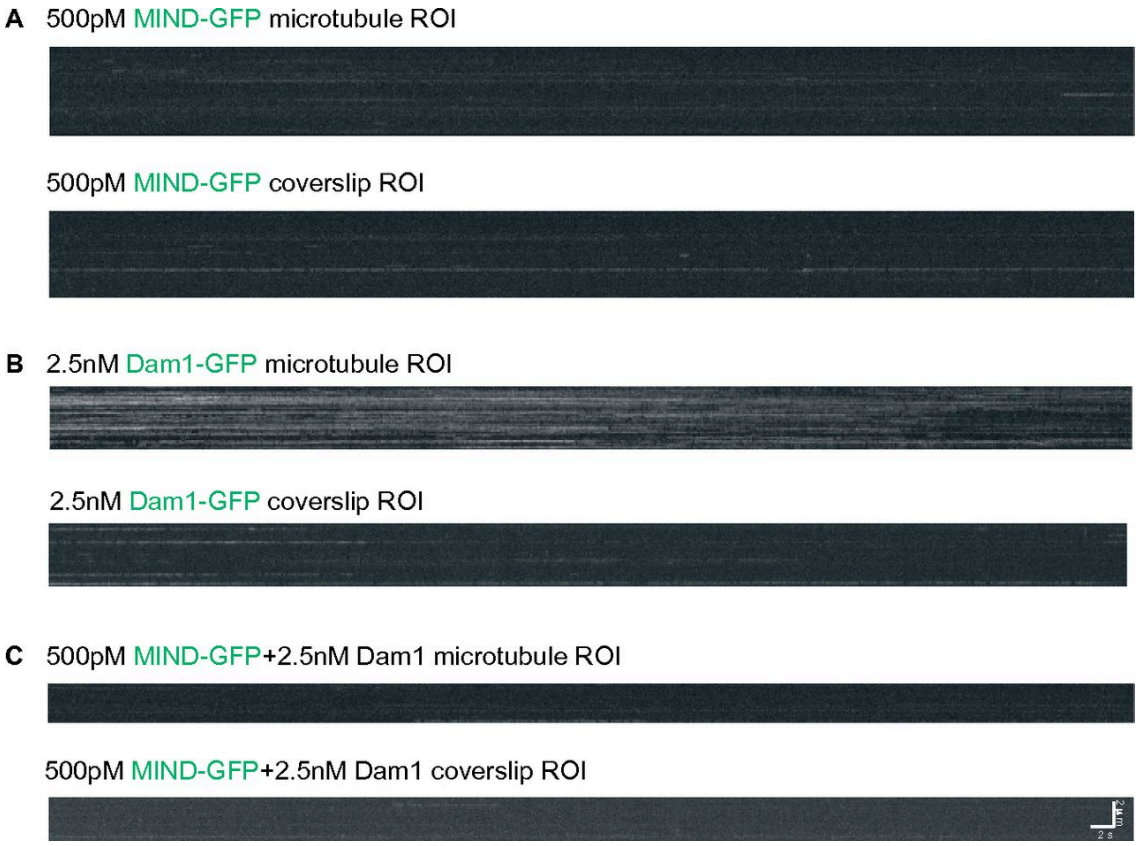

Figure 2.6. MIND-GFP does not bind to microtubules and does not affect Dam1c binding to microtubules.

Representative TIRF kymographs of MIND-GFP (A), Dam1-GFP (B), or MIND-GFP plus Dam1c (C). Binding to region of interest (ROI) with microtubules or coverslip (random ROI, no microtubules) is shown. (A) MIND-GFP shows no binding preference between microtubules (Top) and coverslip (Bottom). (B) Dam1-GFP specifically binds to microtubules (Top) and shows little nonspecific binding to the coverslip (Bottom). (C) MIND-GFP shows no difference between microtubule (Top) and coverslip (Bottom) in the presence of excess Dam1.

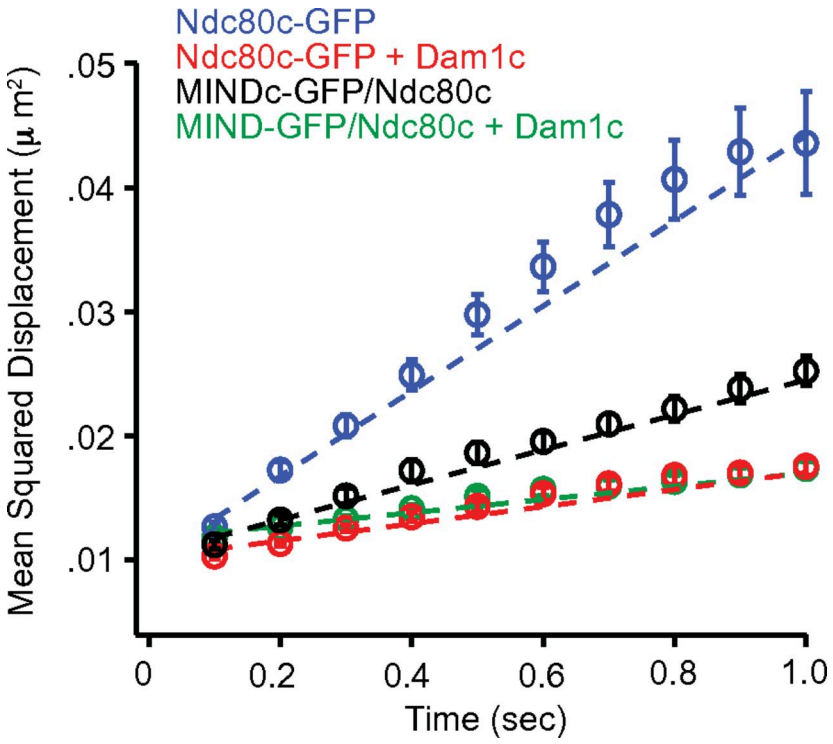

Figure 2.7. MIND and Dam1c have different effects on the diffusion of Ndc80c.

Mean squared displacement of indicated complexes plotted vs. time. Dotted lines show weighted linear fits used to calculate average diffusion constants, with error bars denoting SD. Diffusion constants for each complex are as follows: (blue) Ndc80c-GFP = 0.0343 ± 0.0012 μm2·s−1, (red) Ndc80c-GFP + Dam1c = 0.0069 ± 0.0002 μm2·s−1, (black) MIND-GFP/Ndc80c = 0.0141 ± 0.0004 μm2·s−1, (green) MIND-GFP/Ndc80c + Dam1c = 0.0053 ± 0.0002 μm2·s−1.

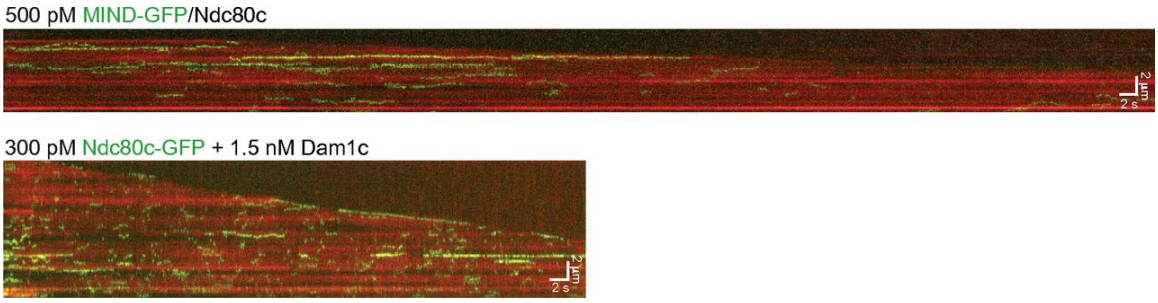

Figure 2.8. Unlike Dam1c, MIND does not enhance the ability of the Ndc80 complex to track with depolymerizing microtubule tips.
Representative two-color TIRF kymograph of MIND-GFP/Ndc80c (Top) or Ndc80c-GFP plus Dam1c (Bottom) with depolymerizing microtubules (red). Ndc80c-GFP efficiently tracks with depolymerizing tips in the presence of Dam1c, with a mean tracking distance of 780 ± 120 nm (n=16) whereas MIND-GFP/Ndc80c failed to track with depolymerizing microtubule tips. Error bars denote SEM. Scale bars are shown in white.

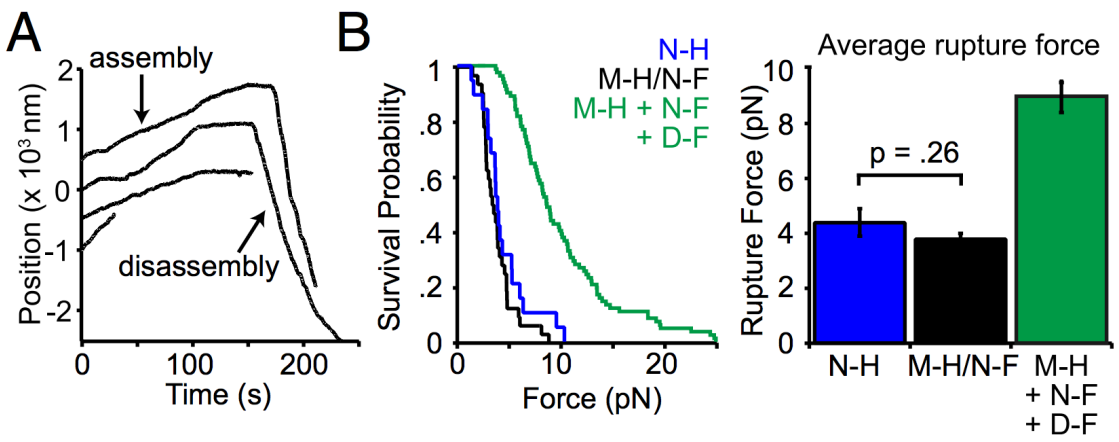

Figure 2.9. The MIND/Ndc80c linkage can withstand substantial load.
(A) Representative traces of bead position versus time for 20 nM MIND-His/Ndc80cFLAG beads tracking with assembling and disassembling microtubule tips under 1.7–2.5 pN of force applied in the direction of microtubule assembly. Traces are arbitrarily offset on the y axis for visual clarity. (B, Left) Survival probability vs. force for 20 nM Ndc80c-His (N-H, n = 20), 20 nM MIND-His/ Ndc80c-FLAG (M-H/N-F, n = 32), and 20 nM MIND-His beads with 40 nM Ndc80c-FLAG and 2 nM Dam1c-FLAG (M-H + N-F + D-F, n = 50). (Right) Average rupture force derived from the distributions on the Left. Ndc80c-His and MIND-His/Ndc80c-FLAG were not significantly different, P = 0.26, twotailed Student's t test. Error bars denote SEM.

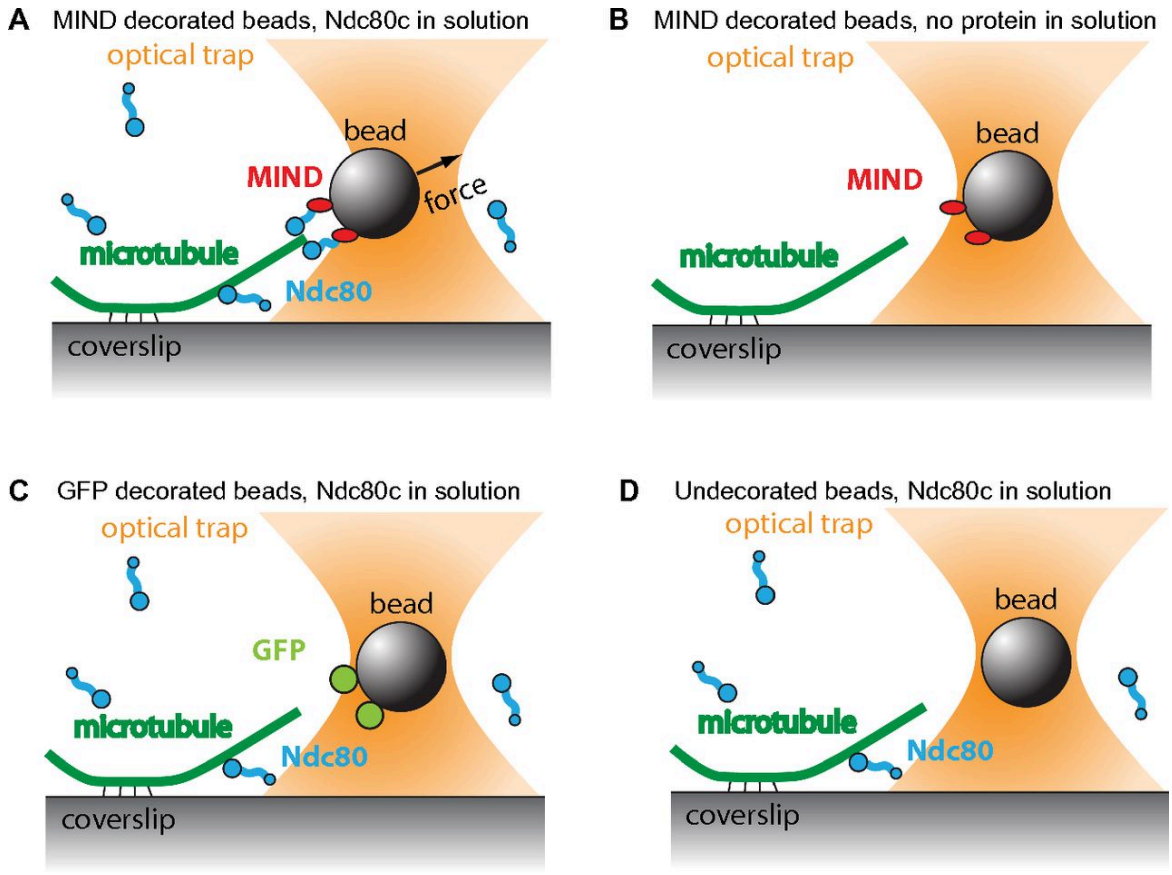

Figure 2.10. The Ndc80 complex and MIND form a specific load-bearing linker in vitro.

(A) MIND-His decorated polystyrene beads form a specific load-bearing linkage to Ndc80c-Flag and can withstand an applied load of ~2.5 pN (n = 32). (B) MIND-His decorated beads cannot form load-bearing attachments to microtubules without Ndc80c-Flag in solution (n = 30). (C) Beads decorated with GFP-His are unable to couple to free Ndc80c-Flag in solution to create force-bearing attachments to microtubules (n = 79). (D) Undecorated beads do not interact with Ndc80c-Flag in solution to form microtubule attachments (n = 60).

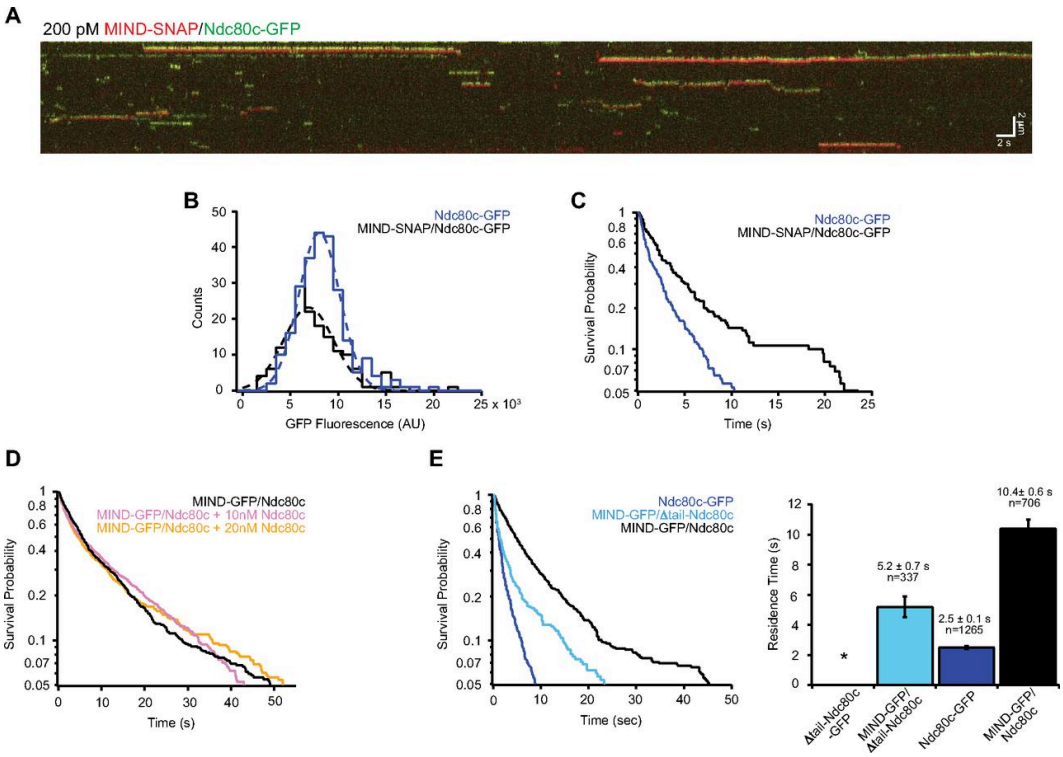

Figure 2.11. MIND does not enhance Ndc80 complex via oligomerization and does not require the Ndc80 N-terminal tail.

(A) Representative two-color TIRF kymograph of individual MIND-SNAP/Ndc80c-GFP complexes binding to microtubules. MIND-SNAP is shown as red and Ndc80c-GFP shown as green. Note: Kymographs for each channel were overlaid with a slight vertical offset to visualize dually fluorescent complexes. Scale bars are shown in white. (B) GFP fluorescence distribution of individual events. Dotted lines show Gaussian fits used to determine mean GFP fluorescence for each complex. MIND-SNAP/Ndc80c-GFP, black histogram, n = 160 events, mean = 7,400 ± 2,600 AU; Ndc80-GFP, blue histogram, n = 248 events, mean = 8,500 ± 2,100 AU. Note that Ndc80c-GFP only events were measured from the same kymographs as MIND-SNAP/Ndc80c-GFP events. (C) Survival probability vs. time for Ndc80c-GFP and MIND-SNAP/Ndc80c-GFP. Ndc80c-GFP, blue line, n = 248 events, average residence time = 2.5 ± 0.2 s; MIND-SNAP/Ndc80c-GFP, black line, n = 160 events, average residence time = 6.2 ± 0.8 s. Error bars denote SD. As in B, the Ndc80c-GFP only events and MIND-SNAP/Ndc80c-GFP events were measured from the same kymographs. (D) Survival probability vs. time for 75 pM MIND-GFP/Ndc80c alone (black line), or with the addition of excess Ndc80c [10 nM (pink line) or 20 nM (gold line)] in solution. The mean residence times were as follows: MIND-GFP/Ndc80c, 12.1 ± 0.7 s, n = 604 events; MIND-GFP/Ndc80c plus 10 nM Ndc80c, 12.1± 0.9 s, n = 464 events; MIND-GFP/Ndc80c plus 20 nM Ndc80c, 11.9 ± 0.7 s, n = 610 events. (E, Left) Survival probability vs. time quantified from individual binding events for each complex noted in the legend. Note: Traces for Ndc80c-GFP and MIND-GFP/Ndc80c are repeated here (from Fig. 3B) for comparison. (Right) Average residence time with error bars denoting SD. For Δtail-Ndc80c-GFP, the * indicates no binding.

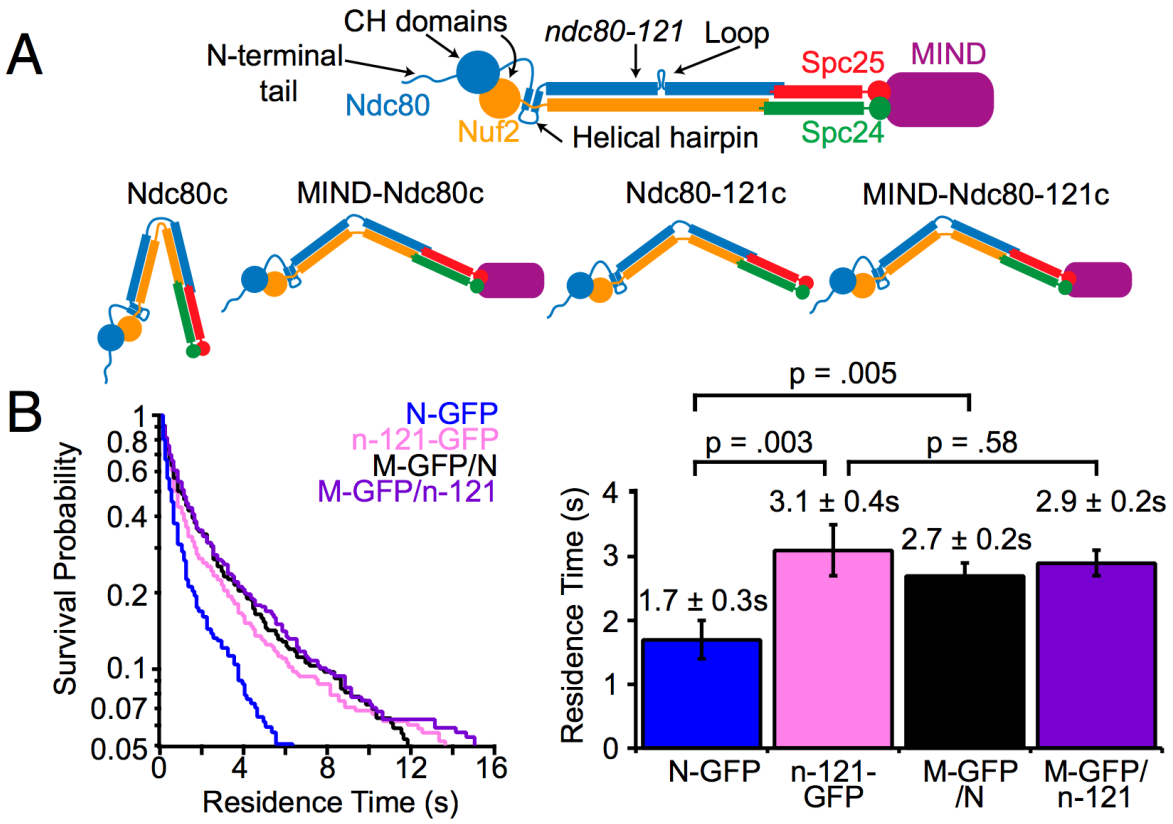

Figure 2.12. MIND activates Ndc80 complex binding via the same mechanism as ndc80-121.

(A, Top) Diagram of Ndc80 complex denoting Ndc80 microtubulebinding domains (CH domain, N-terminal tail) and position of ndc80-121 mutation (Y465C/I469Q) near the loop domain. Modified from ref. 10 with permission from the Genetics Society of America. (Bottom) Diagram depicting proposed conformational changes of MIND-Ndc80c vs. MIND-Ndc80-121c. (B, Left) Survival probability vs. time quantified from individual binding events for Ndc80c-GFP (N-GFP, n = 355), ndc80-121c-GFP (n-121-GFP, n = 481), MIND-GFP/Ndc80c (M-GFP/N, n = 359), and MIND-GFP/ndc80-121 (M-GFP/n-121, n = 426) at the restrictive temperature (37 °C). (Right) Average residence times derived from distributions on Left; error bars denote SD. Ndc80c-GFP is statistically different from Ndc80-121c-GFP, P = 0.003 and MIND-GFP/Ndc80c, P = 0.005 (two-tailed Student's t test). Ndc80-121c-GFP and MIND-GFP/Ndc80-121c are not statistically different (two-tailed Student's t test, P = 0.58).

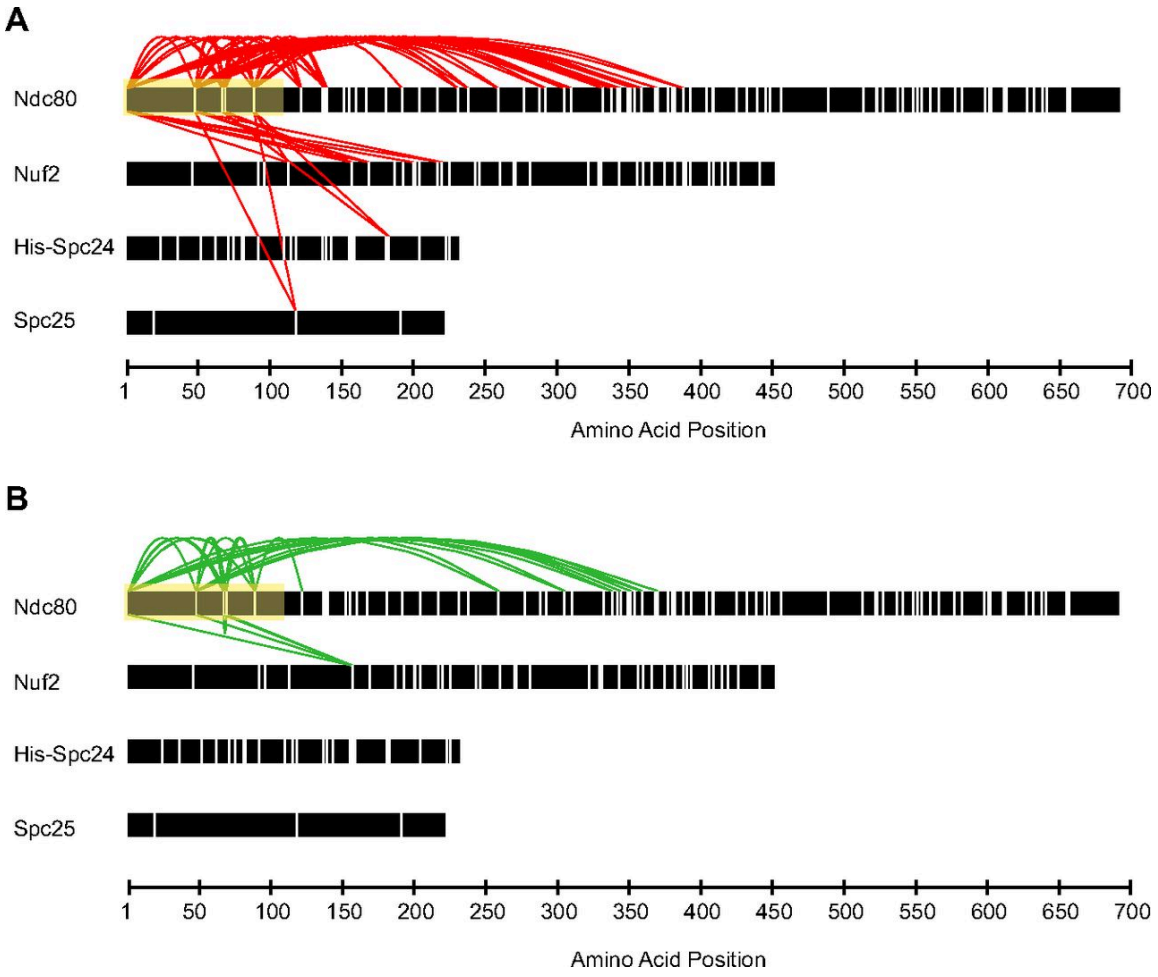

Figure 2.13. The disordered N-terminal Ndc80 tail cross-links extensively within the Ndc80 complex.

Comparison of Ndc80 tail domain (amino acids 1–113, highlighted in yellow) cross-linking to proteins in Ndc80 complex alone (A) or when bound to MIND complex (B). The positions of lysine residues within each protein are marked as vertical white lines. For simplicity, cross-links not involving the tail domain are omitted from diagrams.

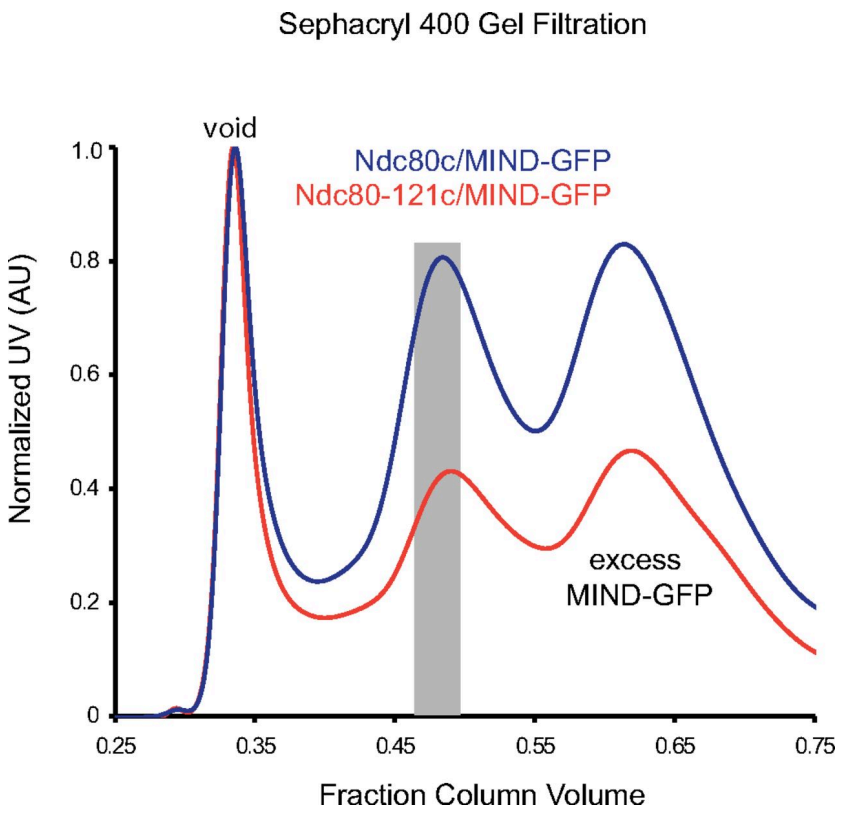

Figure 2.14. Gel filtration profiles of MINDc-GFP/Ndc80c and MINDc-GFP/Ndc80-121c.

Representative Sephacryl 400 gel filtration elution profiles for MINDc-GFP/Ndc80c co-complex (blue) and MINDc-GFP/Ndc80-121c (red). The gray-shaded bar indicates peaks that samples were taken from for experiments. Note that MIND-GFP/Ndc80c and MIND-GFP/Ndc80-121c elute at the same volume, indicating that the mutations in Ndc80-121c do not influence formation of higher order structures.

.

Chapter 3. TIGHT BENDING OF THE NDC80 COMPLEX PROVIDES INTRINSIC REGULATION OF ITS BINDING TO MICROTUBULES[2]

3.1 INTRODUCTION

The highly conserved kinetochore complex Ndc80 (Lampert et al., 2013; McCleland et al., 2003; Tien et al., 2013; Umbreit et al., 2012) is a hub of function within the kinetochore. It is directly involved in kinetochore-microtubule attachment, in bearing mechanical load at the kinetochore-microtubule interface, and in correction of erroneous attachments (Etemad et al., 2015; Powers et al., 2009; Umbreit et al., 2012). The Ndc80 complex specifically localizes only to kinetochores and binds the plus-ends of microtubules *in vivo*. Even in instances of Ndc80 overexpression in yeast or mammalian cells, excess Ndc80 is not found along the microtubule lattice in the mitotic spindle (Diaz-Rodríguez, Sotillo, Schvartzman, & Benezra, 2008; Tang & Toda, 2015). This specific localization to the tips of microtubules mirrors the localization of +TIPs, which often require multiple modes of regulation to ensure accurate targeting to the microtubule plus-end as well as appropriate function (Gireesh, Shine, Lakshmi, Vijayan, & Manna, 2018). Thus, there are likely multiple regulatory mechanisms to ensure both proper localization and function of the Ndc80 complex in cells.

The Ndc80 complex is an elongated and flexible heterotetramer, with two globular ends connected by a coiled coil, which displays a variety of conformations in negative stain electron micrographs (Wang et al., 2008; Zhang et al., 2012) and in crystallized forms (Ciferri et al., 2008; Valverde, Ingram, & Harrison, 2016). Studies suggest that its flexibility is important *in*

[2] This section is closely adapted from a manuscript currently under review in eLife. The work in this section was performed independently.

vivo (Joglekar et al., 2009; Maure et al., 2011; Tien et al., 2014; Wang et al., 2008). For example, the ability of the Ndc80 complex to adopt both straightened and bent conformations is necessary for the proper progression of mitosis (Tien et al., 2014). Cross-linking data suggest that this flexibility is extreme in its range: the Ndc80 complex not only bends, but also has the capacity to adopt a tightly bent conformation (Tien et al., 2014). However, the effect that these conformational changes have on the Ndc80 complex's microtubule-binding activity is unknown. Several studies have shown that microtubule binding by the Ndc80 complex is auto-inhibited (Cheeseman et al., 2006; Kudalkar et al., 2015). But it remains unclear whether the underlying mechanism of auto-inhibition depends on conformational changes of the complex, or how such regulation might influence Ndc80 complex function *in vivo*.

The MIND/Mtw1 complex forms a bridge between the inner and outer kinetochore, directly binding the Ndc80 complex and tethering it to the DNA-binding kinetochore components (Maskell et al., 2010). *In vitro,* the addition of MIND to the Ndc80 complex increases its residence time on the microtubule lattice by nearly four fold (Kudalkar et al., 2015). Based on this and other observations, we previously proposed an allosteric mechanism by which the Ndc80 complex interconverts between a more open form when bound to the MIND complex, and a bent, auto-inhibited state with decreased microtubule binding when unbound from MIND (Kudalkar et al., 2015).

Direct evidence implicating tight bending in the auto-inhibition of Ndc80 complex is lacking, as no study has yet examined conformational changes of the complex while simultaneously monitoring its microtubule-binding activity. To do so, we used single molecule techniques including total internal reflection fluorescence (TIRF) microscopy and single molecule FRET. We found that the Ndc80 complex is auto-inhibited, can tightly bend, and that

the addition of MIND opposes the tightly bent conformation. The ability of the Ndc80 complex to change conformations, and thus tune microtubule affinity, might play an important role for proper localization within the cell. Our work reveals a previously unstudied mode of inherent regulation at the kinetochore.

3.2 Materials and Methods

Protein expression and purification

All protein complexes were expressed in *E. coli* and purified in essentially two steps, beginning with His6- or FLAG-based immuno-precipitation, followed by size exclusion chromatography. The full, heterotetrameric Ndc80 complexes each carried a single His6 tag on either the N- or C-terminus of Spc24 (i.e., Spc24-His6-tagged or His6-Spc24-tagged complex). Likewise, the hetero*dimeric sub*complexes (i.e., His6-Spc24/Spc25 and the 'Broccoli' construct, His6-Ndc80/Nuf2-GFP) each carried an N-terminal His6 tag on one subunit. Each heterodimeric subcomplex was encoded on a separate, dicistronic vector (petDuet and pRSF, for Ndc80/Nuf2 and Spc24/Spc25, respectively), both of which were co-transfected into BL21 cells for purification of the full, heterotetrameric complexes. For purification of subcomplexes alone, single dicistronic vectors were transfected individually. Expression was induced with 0.2 mM isopropyl β-D-1-thiogalactopyranoside (IPTG) for 14 h at 20 °C, cells were lysed with a French press in buffer H (50 mM HEPES, 200 mM NaCl, pH 7.6) supplemented with protease inhibitors (Roche; Basel, Switzerland), 5 mM imidazole, 0.5 uL benzonase and 1 mM PMSF. The cell lysate was then immuno-precipitated onto a 5 mL Ni-charged IMAC resin column (Bio-Rad; Hercules, CA), washed with buffer H, and eluted with 400 mM imidazole in buffer H. The eluate was loaded onto a Superdex 200 16/60 column (GE Healthcare; Chicago, IL) for size-exclusion chromatography. Fractions containing the complex were identified by UV-absorption and

Coomassie blue-stained SDS-PAGE, pooled, and protein concentration was measured using bicinchoninic acid (BCA) (Sigma; St. Louis, MO).

MIND complex carrying an N-terminal FLAG tag on Nsl1 and a C-terminal GFP on Mtw1 was encoded on a single, IPTG-inducible polycistronic vector. Transfected BL21 cells were induced and lysed using a French press, essentially as described above, with the following changes: lysis, immuno-precipitation, and chromatography were all carried out in buffer N (50 mM $NaPO_4$, 200 mM NaCl, pH 7.0). Immuno-precipitation used an anti-FLAG M2 affinity gel (A2220; Sigma; St. Louis, MO). Protein was eluted from the anti-FLAG gel using 0.1 mg/ml 3X FLAG Peptide (F4799; Sigma; St. Louis, MO) in buffer N, and then size exclusion chromatography was performed as described above, but in buffer N.

MIND-GFP/Ndc80 co-complex was prepared by combining two nickel-purified complexes (MIND-GFP and Ndc80) and then performing size-exclusion chromatography. In this case, the MIND complex carried a C-terminal His6 tag on Dsn1 and a C-terminal GFP tag on Mtw1. Expression, lysis, and immuno-purification were performed as described above, using buffer H for Ndc80 and buffer N for MIND. Then the nickel-purified complexes were mixed in a 2.5:1 molar ratio (MIND:Ndc80), incubated for 15 min at room temperature, and purified with a Sepharose 400 size exclusion column using buffer S (50 mM $NaPO_4$, 100 mM NaCl, pH 7.0) (GE Healthcare; Chicago, IL).

Protein labeling for FRET studies

For bulk FRET measurements, the two heterodimeric subcomplexes of the Ndc80 complex were expressed separately, using the methods described above, from dicistronic vectors that were mutated to remove all eight native cysteines and to add the new cysteines required for site-directed labeling with thiol-reactive dyes. After the ‘cysteine-light’ His6-Spc24/Spc25

subcomplex was bound to nickel resin and washed, it was incubated overnight with ~30 mM Cy3 maleimide (GE Healthcare; Chicago, IL). The resin was then washed again, to remove free Cy3, and added to cleared lysate from cells expressing the (cysteine-light) Ndc80/Nuf2 subcomplex, to allow formation of the full heterotetrameric Ndc80 complex. The resin was then washed and incubated overnight with ~30 mM Cy5 maleimide (GE Healthcare; Chicago, IL). Proteins were eluted with 400 mM imidazole in buffer H and then purified by size exclusion chromatography (using the Superdex 200 column, as described above). Labeling efficiency was estimated to be 1:1 Cy3:Spc45/Spc25 dimer and 0.8:1 Cy5:Ndc80/Nuf2 dimer by calculating protein concentration (using a NanoDrop and BCA assay) and calculating dye molecule concentration (using a NanoDrop).

For single molecule FRET assays, the two cysteine-light heterodimeric subcomplexes were co-expressed together, according to the methods described earlier. After the full heterotetrameric Ndc80 complex was bound to the nickel resin and washed, it was incubated overnight with an equimolar combination of ~15 mM Cy3 maleimide and ~15 mM Alexa Fluor 647 maleimide (Thermo Fisher; Waltham, MA). The complex was eluted with 400 mM imidazole in buffer H and then purified by size exclusion chromatography (Superdex 200). Labeling with both dyes simultaneously during purification decreased the duration of the protocol relative to the bulk FRET protocol (where dyes were added sequentially), thereby avoiding degradation of the N-terminal Ndc80 tail (Figures 3.9 A and B). Our labeling protocol was adapted from (Joo & Ha, 2012).

Bulk FRET measurement

Dye-labeled oligonucleotides were purchased (from IDT; Coralville, IA) with the sequences 5'-GCTATGACCATGATATAC-Cy5-3' and 5'-Cy3-AGCGCGCAATTAACCC-3' (Tsuji et al.,

2001). To create a positive control, the dye-labeled oligos were annealed in buffer T (10 mM TRIS buffer pH 7.5, 50 mM NaCl) onto a complementary unlabeled target strand, 5'-GGGTTAATTGCGCGCTTGGCGTAATCATGGTCATAGC-3', by mixing 10 uM of the target strand with 5 uM each of the single-stranded, labeled oligonucleotides, heating at 95˚C for 2 min, and then allowing the mixture to cool to room temperature for one hour. For the negative control, the two labeled oligos were mixed together without the target strand. To determine bulk FRET levels, oligo controls or end-labeled Ndc80 complexes were diluted to 0.25 uM in buffer H and fluorescence emission spectra were measured from 560 to 730 nm in a spectrofluorometer (Spex Fluorolog-3, Horiba Jobin Yvon; Edison, NJ), under 550 nm excitation and using a 2 nm bandwidth. Relative FRET efficiency, E_{FRET}, was calculated using the equation,

$$E_{FRET} = \frac{I_A}{I_A + I_D} \quad (3.1)$$

where I_D and I_A represent the background-subtracted intensities of donor (Cy3) and acceptor (Cy5) dyes, measured at their peak emission wavelengths (565 and 670 nm, respectively).

Preparation of oligo controls and flow channel setup for single molecule FRET.

For tethering onto streptavidin-coated coverslip surfaces, a biotinylated oligonucleotide target strand was purchased with the sequence, 5'-Biotin-GGGTTAATTGCGCGCTTGGCAAAAGTATCATGGTCATAGC-3'. The positive control was created in this case with two additional dye-labeled oligos, purchased with the sequences 5'-GCTATGACCATGATATAC-AF647-3' and 5'-Cy3-AGCGCGCAATTAACCC-3'. When both of these are annealed to the target strand, the donor and acceptor dyes (Cy3 and Alexa Fluor 647, respectively) are held in very close proximity (< 10 nm). For the negative control, the same two oligos were ordered but with the dyes moved to opposite ends, 5'-AF647-GCTATGACCATGATATAC-3' and 5'-AGCGCGCAATTAACCC-Cy3-3'. When

both of these are annealed to the target strand, the two dyes are held far apart (> 10 nm). Annealing was performed in buffer T using the same method described above for bulk FRET. Alexa Fluor 647 was used as the acceptor dye for all single molecule FRET measurements (i.e., on oligonucleotide controls as well as on the Ndc80 complexes) because of its greater photostability compared to Cy5.

Control, surface-tethered oligos were observed in flow channels created using double-stick tape adhered to plasma-cleaned glass slides and coverslips (Deng & Asbury, 2017). Briefly, dry channels were assembled and then warmed for at least 3 hours at 50˚C, to promote adherence of the tape to the glass. Biotinylated bovine serum albumin (Vector Laboratories; Burlingame, CA) was introduced first and incubated for 5 minutes. After a wash in buffer TE (100 mM Tris, pH 8, 10 mM EDTA, 100 mM KCl), avidin-DN (Vector Laboratories; Burlingame, CA) was introduced and incubated for 5 minutes. The channel was re-washed with buffer TE supplemented with 8 mg/ml BSA, and then the oligos were introduced and incubated for 3 minutes, to allow binding to the surface. Untethered oligos were removed by a final wash with buffer TE supplemented with 8 mg/ml BSA plus an oxygen scavenging system (2 μM glucose oxidase, 10 μM catalase, 10 mM Trolox, 1mM glucose). The channels were sealed with nail polish and imaged in a TIRF microscope, as described below (under Single molecule FRET TIRF microscopy).

Surface-tethered Ndc80 complexes were observed in flow channels created as described above but using PEGylated coverslips. After warming at 50° C for 3 h, the dry channels were first filled with buffer HN (25 mM HEPES buffer pH 7.6, 150 mM NaCl) and then small unilamellar vesicles (0.1% BioPE lipids in POPC lipids, Avanti Polar Lipids, Inc; Alabaster, AL) were introduced and incubated for 5 minutes, to coat the glass surfaces with a supported lipid bilayer

that included a small fraction (0.1%) of biotinylated lipids (Deng & Asbury, 2017). After washing with buffer HN, avidin-DN was introduced and incubated for 5 minutes. The channel was then washed with BRB80 (80 mM piperazine-N,N′-bis(2- ethanesulfonic acid), pH 6.9, 1 mM $MgCl_2$, 1 mM EGTA) supplemented with blocking proteins, 6.9 mg/ml BSA and 0.04 mg/ml κ-casein. Anti-penta-His antibody (Qiagen; Venlo, Netherlands) was then introduced and incubated for 5 min, and the channel was washed again with BRB80 plus blocking proteins. The end-labeled Ndc80 complexes, diluted into BRB80 plus blocking proteins, were then introduced and incubated for 5 minutes to allow binding to the surface. Untethered Ndc80 complex was removed by a final wash of BRB80 plus blocking proteins and an oxygen scavenging system (2 μM glucose oxidase, 10 μM catalase, 1 mM glucose). The channels were sealed and imaged in a TIRF microscope as described below (under Single molecule FRET TIRF microscopy).

To observe surface-tethered Ndc80 complexes in co-complex with GFP-MIND, the end-labeled Ndc80 complex and GFP-MIND complex were pre-incubated in a 1:10 ratio for 15 min at room temperature, and then tethered to lipid-coated coverslips exactly as described in the previous paragraph.

To observe FRET from individual Ndc80 complexes on microtubules, Alexa Fluor 488-labeled, taxol-stabilized microtubules were tethered to coverslips, as previously described (Powers et al., 2009). The end-labeled Ndc80 complex was diluted in BRB60 buffer (60 mM piperazine-N,N′-bis(2- ethanesulfonic acid), pH 6.9, 1 mM $MgCl_2$, 1 mM EGTA), introduced and allowed to bind the tethered microtubules for 1 min before imaging. We used BRB60 rather than BRB80 for this experiment, because the reduction in ionic strength increases the residence time and slows the

diffusion of the Ndc80 complexes on the microtubules (Powers et al., 2009), thereby facilitating collection of longer-duration records of fluorescence intensity from individual complexes.

Single molecule FRET microscopy

All samples were imaged in a custom TIRF microscope, with three cameras that simultaneously recorded images in green (500 to 550 nm wavelengths), yellow (575 to 625 nm), and red (660 to 740 nm) color-bands, as described in detail in (Deng & Asbury, 2017). In the following description of methods, we refer to each camera by the central wavelength of its color-band: 525-nm for green, 600-nm for yellow and 700-nm for red. Each prepared slide had up to three flow channels with different experimental conditions. One of the flow channels, containing all assembly reagents but lacking labeled oligonucleotides or protein, was always included as a check for background fluorescence. Movies lasting 30 or 40 s were recorded at 10 frames per second, with roughly 50 to 150 particles imaged per field of view, while the sample was illuminated in four distinct intervals: (i) first FRET was measured by exciting the donor (Cy3) and acceptor dyes (AF647) with 561-nm laser illumination (at a nominal power of 25 mW), (ii) then the acceptor dyes (AF647) were directly excited with 641-nm illumination (at 25 mW), (iii) then the 641-nm illumination power was increased (to 100 mW) in order to photobleach the acceptor dyes, and (iv) finally the donor dyes were measured alone with (25 mW) 561-nm illumination. This illumination sequence, which is shown in Supplemental Figure 4C, allowed verification that both donor and acceptor dyes were present on every molecule analyzed, that donor fluorescence was enhanced after acceptor photobleaching, and that the correction of acceptor signals for cross-excitation and spillover was accurate. (The method of correcting for cross-excitation and spillover is described below.) For some experiments, an additional brief

488-nm laser illumination was added at the beginning and end of the sequence to record fluorescence from GFP-MIND or from Alexa Fluor 488-labeled microtubules.

Single molecule FRET analysis

Analysis was done using custom, semi-automated software written in Labview (National Instruments; Austin, TX) and Igor Pro (Wavemetrics; Lake Oswego, OR). For each movie (corresponding to a single field of view), the first 10 frames from each camera were averaged to create initial static images (at emission wavelengths around 525 nm, 600 nm, and 700 nm) that were used to identify the properly labeled Ndc80 complexes carrying both donor and acceptor dyes, according to a previously described method (Deng & Asbury, 2017). (Because of the method of labeling concurrently with both dyes, the Ndc80 complexes used for single molecule FRET experiments were a mixture of those with one or two donor dyes, one or two acceptor dyes, or one of each at either cysteine residue location.) Records of fluorescence versus time from each camera over the entire duration of the movie were generated by integration of the intensities within 7x7 pixel regions of interest centered on the particles. For analysis of Ndc80 complexes in co-complex with GFP-MIND, the three-color particles carrying an end-labeled Ndc80 complex (with both Cy3 and AF647) that colocalized with a GFP-MIND were identified and distinguished from the two-color particles consisting of end-labeled Ndc80 complex alone. For analysis of FRET exhibited by Ndc80 complexes attached to microtubules, only non-diffusing, two-color Ndc80 complex particles that remained bound to the microtubules over the entire duration of the movie were included. Before the calculation of FRET levels, raw records of fluorescence versus time were first corrected for background, spillover, and cross-excitation. Background was measured on a slide-to-slide basis and subtracted from the corresponding records.

Estimation of spillover. While most of the fluorescence emission from the donor Cy3 dyes fell onto our 600-nm camera, their spectrum is broad enough that a fraction of their emission 'spilled over' onto the 700-nm camera. To quantify this spillover effect, we imaged single oligonucleotides labeled with Cy3 alone (under 561-nm excitation) and measured the ratio of their emission at 700 nm divided by their emission at 600 nm,

$$\boldsymbol{S} = \frac{\boldsymbol{I}_{561}^{700}}{\boldsymbol{I}_{561}^{600}} \qquad (3.2)$$

where $\boldsymbol{S}$ represents the spillover ratio, $\boldsymbol{I}_{561}^{700}$ represents the intensity measured at 700-nm emission under 561-nm excitation, and $\boldsymbol{I}_{561}^{600}$ represents the intensity measured at 600-nm emission under 561-nm excitation. For Cy3 molecules in our microscope, $\boldsymbol{S}$ = 0.13 ± 0.01 (mean ± sdev from N = 63 molecules).

Estimation of cross-excitation. The 561-nm laser excitation used during our single molecule FRET measurements is near the peak absorption for the donor Cy3 dyes. While this wavelength is considerably shorter than the peak absorption for the acceptor AF647 dyes, it nevertheless directly excites some fluorescence in AF647. To quantify this 'cross-excitation' effect, we imaged single oligonucleotides labeled with AF647 alone and measured the ratio of their emission (at 700 nm) when cross-excited at 561 nm divided by their emission (again at 700 nm) when excited with nominally identical power at 641 nm,

$$\boldsymbol{X} = \frac{\boldsymbol{I}_{561}^{700}}{\boldsymbol{I}_{641}^{700}} \qquad (3.3)$$

where $\boldsymbol{X}$ is the cross-excitation ratio, $\boldsymbol{I}_{561}^{700}$ is the intensity measured at 700-nm emission under 561-nm excitation, and $\boldsymbol{I}_{641}^{700}$ is the intensity measured at 700-nm emission under 641-nm excitation. For AF647 molecules in our microscope, $\boldsymbol{X}$ = 0.37 ± 0.07 (mean ± sdev from N = 46 molecules).

Correction for spillover and cross-excitation. For FRET measurements with the end-labeled Ndc80 complexes or oligonucleotide controls, intensity versus time at emission wavelengths around 600 nm and 700 nm was measured initially with 561-nm laser illumination (at a nominal power of 25 mW), which after background-subtraction yielded records of donor and acceptor emission versus time, $\boldsymbol{I}_D(t)$ and $\boldsymbol{I}_A^*(t)$, respectively. Illumination was then switched to 641 nm (at 25 mW) to measure acceptor intensities at 700-nm emission under direct excitation, $\boldsymbol{I}_{641}^{700}$. After photobleaching the acceptors (with 100 mW at 641 nm), the illumination was switched back to 561 nm (at 25 mW) to measure intensities of the donors alone at 600-nm emission, $\boldsymbol{I}_{561}^{600}$. Each record of acceptor emission was then corrected for spillover and cross-excitation using the equation,

$$\boldsymbol{I_A(t) = I_A^*(t) - \ S \cdot I_{561}^{600} \ - \ X \cdot I_{641}^{700}} \qquad (3.4)$$

where $\boldsymbol{I_A(t)}$ represents the corrected acceptor emission versus time.

FRET calculation. Single molecule FRET efficiency versus time, $\boldsymbol{E}_{FRET}(t)$, was calculated using the equation,

$$\boldsymbol{E}_{FRET}(t) = \frac{\boldsymbol{I}_A(t)}{\boldsymbol{I}_A(t)+\boldsymbol{I}_D(t)} \qquad (3.5)$$

Histograms of FRET efficiency were generated using concatenated $\boldsymbol{E}_{FRET}(t)$ records from at least 41 individual molecules. The no-FRET peak of the histogram generated from negative control molecules was fit with a Gaussian function to determine a threshold two standard deviations above the center of the Gaussian. Values above this threshold (0.30) were considered high-FRET. To examine the kinetics of switching between no- and high-FRET states, the numbers of upward and downward threshold-crossings in FRET records from 207 individual

Ndc80 complexes were counted and the total times spent above and below the threshold were summed. An estimated rate of 'opening', $k_{opening}$, was determined from the total number of downward crossings divided by the total time spent above the threshold. Likewise, an estimated rate of 'closing', $k_{closing}$, was determined from the total number of upward crossings divided by the total time spent below the threshold.

Estimating how tight bending affects the affinity of Ndc80 complex for microtubules.

We envision a four-state reaction scheme in which the closed (tightly bent) and open conformations of the Ndc80 complex are in equilibrium with each other, both on and off the microtubule, as depicted in Figure 5E. In order to satisfy the principle of microscopic reversibility, the following relation must hold,

$$\boldsymbol{K}_d^{closed} = \boldsymbol{K}_d^{open}\left(\frac{\boldsymbol{K}_{eq}^{bound}}{\boldsymbol{K}_{eq}^{free}}\right) \qquad (3.6)$$

where $\boldsymbol{K}_d^{closed}$ and $\boldsymbol{K}_d^{open}$ are the equilibrium constants for dissociation from the microtubule by the closed and open conformations, respectively, and where $\boldsymbol{K}_{eq}^{bound}$ and $\boldsymbol{K}_{eq}^{free}$ are equilibrium constants for opening (straightening) of the Ndc80 complex when it is microtubule-bound and free, respectively. Our observation that 6% of microtubule-attached Ndc80 complexes exhibit high FRET implies that $\boldsymbol{K}_{eq}^{bound} \cong 19$. Our observation that 25% of Ndc80 complexes alone exhibit high FRET suggests that $\boldsymbol{K}_{eq}^{free} \cong 3$. (Here we assume that tethering to the coverslip does not alter the energetics of the opening-closing transition.) Inserting these values into the above equation indicates that $\boldsymbol{K}_d^{closed} \cong 6 \cdot \boldsymbol{K}_d^{open}$, implying a 6-fold weaker affinity for microtubules when the Ndc80 complex is tightly bent.

3.3 RESULTS

Microtubule binding by the Ndc80 complex is auto-inhibited by its Spc24/Spc25 end

Previous work (Cheeseman et al., 2006; Kudalkar et al., 2015) suggested the possibility of an intra-molecular, auto-inhibitory interaction in which the tetrameric Ndc80 complex bends tightly, allowing its Spc24/Spc25 end to associate closely with, and reduce the microtubule-binding of its Ndc80/Nuf2 end (Figure 3.1 A). To test directly for inhibition of Ndc80/Nuf2 by Spc24/Spc25, we measured the microtubule binding of a shortened dimeric construct, called 'Broccoli' (Schmidt et al., 2012) consisting of just the Ndc80 and Nuf2 proteins truncated to remove their C-termini (Ndc80 1-556, Nuf2 1-339), through which they would normally tetramerize with Spc24 and Spc25 (Wei et al., 2005). A Broccoli construct with GFP fused C-terminally to Nuf2 was purified (Broccoli-GFP; Figure 3.6 A) and its binding to taxol-stabilized microtubules was observed using single molecule total internal reflection fluorescence (TIRF) microscopy. Full-length, GFP-tagged Ndc80 complex was also examined as a control. Consistent with previous studies (Kudalkar et al., 2015; Powers et al., 2009), individual full-length Ndc80 complexes bound transiently and relatively weakly to microtubules, with a mean residence time of 2.9 ± 0.3 s (Figures 3.1 B and C). Individual Broccoli-GFP bound longer, with a mean residence time of 5.6 ± 0.7 s, roughly twice as long as full-length Ndc80-GFP, suggesting that removal of the Spc24/Spc25 end of the complex relieves an auto-inhibitory effect (Figures 3.1 B and C).

We reasoned that if the Spc24/Spc25 end is responsible for auto-inhibition within the full-length complex, then free Spc24/Spc25 dimer added *in trans* might be sufficient to inhibit microtubule binding. Indeed, when free Spc24/Spc25 dimer was purified (Figure 3.6 C) and added in 60-fold excess to Broccoli-GFP, the mean residence time of Broccoli-GFP on microtubules was reduced to 3.3 ± 0.4 s, which is statistically indistinguishable ($p = 0.4$) from

the residence time of full-length Ndc80 complex alone. Adding MIND-GFP to full-length Ndc80 complex increased its residence time on microtubules more than 3-fold, from 2.9 ± 0.3 s to 9.8 ± 1.1 s (Figure 3.1 B and C), consistent with previous measurements (Kudalkar et al., 2015). This MIND-dependent increase was almost completely abolished by addition of a 10-fold excess of Spc24/Spc25 dimer, which brought the residence time for the Ndc80-MIND-GFP co-complex down to 4.1 ± 0.5 s (Figures 3.1 B and C), similar to that of full-length Ndc80 alone. Free Spc24/Spc25 dimer does not detectably bind microtubules by itself (Wei et al., 2007).

We also tested whether full-length Ndc80 complex without MIND could be further inhibited by excess free Spc24/Spc25 dimer. For this test, we increased the dynamic range of our measurements by replacing our standard BRB80 buffer with BRB60, which lowers the concentration of cations and thereby raises the mean residence time for full-length Ndc80 complex up to 5.7 ± 0.7 s (Figure 3.6 B). Addition of free Spc24/Spc25 dimer under these conditions decreased the mean residence time of Ndc80-GFP complex in a concentration-dependent manner (Figure 3.6 B). Together these observations show that the Spc24/Spc25 dimer can interact with Ndc80/Nuf2 independently of the tetramerization domain, and that this secondary interaction is sufficient to inhibit the microtubule binding of Ndc80/Nuf2, of the full-length Ndc80 complex, and of the MIND-Ndc80 co-complex.

Acidic residues in Spc25 are important for auto-inhibition

Electrostatic interactions are crucial for binding of the Ndc80 complex to microtubules. Basic residues located on the globular (calponin homology) domains of the Ndc80 and Nuf2 subunits have been shown to interact with acidic patches on the surface of the microtubule to enable microtubule binding (Ciferri et al., 2008). Additionally, charge-charge interactions between the N-terminal ‘tail’ of Ndc80 and the microtubule lattice tune this microtubule binding through

phosphorylation (Zaytsev et al., 2015; Zaytsev, Sundin, DeLuca, Grishchuk, & DeLuca, 2014). Considering the central role of electrostatic interactions in microtubule-binding of the Ndc80 complex, we hypothesized that similar electrostatic effects might also contribute to the intra-complex interactions underlying its auto-inhibition. Sequence alignment revealed three acidic residues located on one face of the Spc25 subunit that are highly conserved, suggesting functional importance (Figure 3.6 E). To probe whether negative charges on this face of Spc25 contribute to inhibitory intra-complex interactions, we mutated a total of 7 acidic residues – including the 3 identified by sequence conservation plus 4 others located nearby on the same face – to lysine residues. We then purified a charge-reversal mutant dimer of Spc24/Spc25 carrying the lysine substitutions (hereafter referred to as Spc24/Spc25-7K) (Figures 3.6 C and D). When added in 60-fold excess, Spc24/Spc25-7K failed to detectably inhibit the microtubule-binding activity of Broccoli-GFP (mean residence time of 6.9 ± 0.6 s with versus 5.6 ± 0.7 s without the addition Spc24/Spc25-7K; $p = 0.16$), in contrast to the wild-type Spc24/Spc25 dimer (3.3 ± 0.4 s with versus 5.6 ± 0.7 s without; $p = 0.006$) (Figures 3.1 B and C). This observation indicates that electrostatic interactions play a role in auto-inhibition of the complex.

The Ndc80 complex can bend tightly

Electron micrographs of purified, negatively stained samples of Ndc80 complex show that the coiled-coil can adopt a variety of conformations, with a tendency to bend at or near the 'loop,' an unstructured region of 50-60 residues within the Ndc80 protein (Wang et al., 2008; Zhang et al., 2012). Genetic evidence suggests the complex must bend tightly to function properly (Tien et al., 2014), but the propensity of the complex for tight bending has not been directly examined. To monitor bending of the Ndc80 complex, we used Förster resonance energy transfer (FRET). We first created plasmids encoding a cysteine-free version of the complex by mutating all eight of its

native cysteine codons to serine codons. Then two new cysteines were introduced, replacing native surface-exposed serines at either end of the complex, near the N-terminus of Nuf2 (S2C) and on the RWD domain of Spc25 (S154C) (Figures 3.2 A and B). Sequential labeling with cysteine-reactive dyes during purification created a homogenous population of complexes, each with a Cy3 dye on the Spc24/Spc25 end and a Cy5 dye on the Ndc80/Nuf2 end, which bound to microtubules with an affinity similar to that of Ndc80-GFP (Figure 3.2 C, and Figure 3.8). At these locations, the two dyes should not come into close enough proximity for FRET (i.e., < 10 nm apart) unless the complex adopts a tightly bent configuration (Figure 2D).

To test for tight bending of the Ndc80 complex in solution, we began by measuring the end-labeled complex in a bulk FRET assay (Figure 3.2 E). For comparison, we also examined positive and negative controls made from two single-stranded DNA oligonucleotides labeled with Cy3 and Cy5. For the positive control, the labeled oligos were annealed to a target strand, creating a double-stranded DNA assembly with the dyes held in close proximity (L. J. Friedman, Chung, & Gelles, 2006). For the negative control, the same oligos were mixed together without the target strand. Fluorescence emission spectra were measured for the three samples and FRET efficiency was estimated from the peak donor and acceptor intensities (at 565 and 670 nm, respectively; see Materials and Methods). The end-labeled Ndc80 complex exhibited a FRET efficiency of 0.29 (Figure 3.2 E), a value intermediate between the positive and negative controls (0.53 and 0.10, respectively). This observation indicates that in solution, the Ndc80 complex can adopt a tightly bent conformation, which brings its two ends in close proximity.

The Ndc80 complex fluctuates between tightly bent and more open conformations

Simple bulk fluorescence measurements cannot distinguish between a single population of Ndc80 complexes exhibiting moderate FRET or a mixture of complexes including both low- and

high-FRET subpopulations, nor can they provide information about dynamics of the underlying conformational changes. We therefore turned to single molecule FRET to examine bending of individual complexes. End-labeled Ndc80 complexes (Figures 3.9 A and B) were specifically tethered to coverslip surfaces and imaged by multi-color TIRF microscopy (Figures 3.3 A and B). Emission from individual donor (Cy3) and acceptor (Alexa Fluor 647) dyes was measured simultaneously from brief, ~2 s time-lapse recordings during excitation of the donor (i.e., at a wavelength of 561 nm). FRET versus time for each complex was computed from the donor and acceptor signals, I_D and I_A, after subtracting background levels and correcting for spillover and cross-excitation (Roy, Hohng, & Ha, 2008; Selvin & Ha) (Figure 3C). Following each measurement, the acceptor was excited directly (at 641 nm) until it photobleached, to confirm the presence of a single acceptor dye on every analyzed complex (Figure 3.9 C).

Donor and acceptor signals recorded from individual end-labeled Ndc80 complexes were anti-correlated; their FRET levels fluctuated between low values around zero and higher values approaching unity (Figure 3.3 C). The distribution of FRET levels was broad, with a large fraction (25%) of high-FRET values more than two standard deviations above the mean of the no-FRET population (Figure 3.3 E). In contrast, FRET from positive and negative control oligos was more stable, with only small deviations from unity and zero, respectively (Figure 3.3 E and Figures 3.9 D and F). Likewise, FRET from a positive control Ndc80 complex, which carried donor and acceptor dyes close together on the same face of Spc25 (Figure 3.9 E), remained stably high (Figure 3.9 F). Based on a simple two-state threshold-crossing analysis, switching of the end-labeled Ndc80 complexes from low to high FRET occurred at a rate of $k_{closing} = 0.23 \pm 0.024\ s^{-1}$. Switching from high to low FRET was about 4-fold faster, occurring at a rate of $k_{opening} = 0.96 \pm 0.094\ s^{-1}$ (Figure 3.3 D). The high-FRET fluctuations were eliminated when intra-

complex interactions were competitively inhibited by adding a 100-fold excess of free Spc24/Spc25 (Figures 3.3 F and 3.3 G). Altogether, these single molecule observations confirm that the Ndc80 complex can adopt a tightly bent conformation, with both ends interacting closely together, in agreement with our bulk measurements, and they show that the complex fluctuates dynamically between tightly bent and more open conformations.

The loop region of Ndc80 contributes to tight bending of the complex

A flexible region of 50-60 residues within the Ndc80 protein interrupts the coiled-coil of Ndc80/Nuf2 to form a loop (Ciferri et al., 2005), which has been implicated in flexibility of the Ndc80 complex (Wang et al., 2008). To determine whether this region also contributes to tight bending, we measured FRET levels for a mutant Ndc80 Δ490-510 complex lacking part of the loop (Figure 3.4 A). In budding yeast cells, this partial loop deletion confers temperature sensitivity (Maure et al., 2011), indicating functional importance. FRET levels from purified individual Ndc80 Δ490-510 complexes were relatively low. The percentage of high-FRET values was only 5.6%, which is 4-fold less than the percentage measured from wild-type complexes (Figures 3.4 B and C). Thus, as expected, the loop contributes to tight bending, presumably because it confers flexibility to the complex.

We also examined which areas on the globular ends of the Ndc80 complex come close together in the tightly bent conformation by creating an additional three end-labeled Ndc80 complexes. We chose two new sites within the complex to mutate to cysteine residues (Nuf2 Q74C and Spc24 N185C), and along with the two original dye locations (Nuf2 S2C and Spc25 S154C), engineered pairwise combinations, each with one dye on the Ndc80/Nuf2 end and one dye on the Spc24/Spc25 end (Figure 3.10 A). Retaining one dye at the original location on Nuf2 S2C and moving the other to Spc24 N185C did not significantly change the FRET levels (25 ±

6.6% high-FRET values versus 25 ± 5.2% for the original locations) (Figures 3.10 B and C). However, moving the dye from Nuf2 S2C to Nuf2 Q74C, regardless of the dye location on Spc24/Spc25, reduced the fraction of high-FRET values more than 2-fold (Figures 3.10 C and D). These results suggest that, in the tightly bent configuration, the Spc24/Spc25 end of the complex associates closely with one face of the Ndc80/Nuf2 end, near the N-terminus of Nuf2.

Tight bending of the Ndc80 complex is inhibited by binding to either microtubules or the MIND complex

According to our model, tight bending of the Ndc80 complex enables its Spc24/Spc25 and Ndc80/Nuf2 ends to interact in a manner that inhibits microtubule binding. Consequently, when Ndc80 complexes are bound to microtubules they should be found primarily in the more open conformation (i.e., binding to microtubules should 'select' for the open complexes). To test this prediction, we measured FRET levels for individual end-labeled complexes bound to taxol-stabilized microtubules (Figure 3.5 A). As expected, FRET from the microtubule-bound complexes was low, with only a small fraction of high-FRET values, 6.2% (Figures 3.5 B and D). Assuming a simple four-state equilibrium between closed and open configurations (Figure 3.5 E), the high-FRET fractions measured for microtubule-attached (Figure 3.5 D) and 'free' Ndc80 complexes (coverslip-tethered, Figures 3.3 D, 3.4 C and 3.5 D) imply that the tightly bent conformation has a 6-fold lower affinity for microtubules than the open conformation (see Materials and Methods).

Association of the Ndc80 and MIND complexes together creates a co-complex with enhanced affinity for microtubules relative to Ndc80 complex alone (Kudalkar et al., 2015). Genetic evidence suggests this enhancement might occur because MIND prevents the Ndc80 complex from adopting the tightly bent, auto-inhibited state (Tien et al., 2014). Evidence

suggests that the Ndc80 complex of *C. elegans* might also be activated by the Mis12 complex, which is the worm counterpart of MIND (Cheeseman et al., 2006). To test directly whether MIND prevents tight bending, we added free GFP-MIND to the end-labeled Ndc80 complexes (which were tethered sparsely to coverslips, as above). Using three-color TIRF microscopy, the end-labeled Ndc80 complexes that formed co-complexes with MIND were first distinguished from those that did not by assessing co-localization of the GFP signal with both Cy3 and Alexa Fluor 647 dyes (Figure 3.5 C). Then FRET between donor and acceptor dyes on the Ndc80 complexes was measured. With a 10-fold excess of free GFP-MIND, 33% of the end-labeled Ndc80 complexes formed co-complexes with MIND. FRET levels from these Ndc80-MIND co-complexes were low, with only 4.9% of values significantly above the no-FRET population (Figures 3.5 B and 3.5 D). In contrast, FRET levels from Ndc80 complexes in the same fields of view but lacking MIND-GFP were higher, with a 5-fold larger fraction of high-FRET values, 29%, which is statistically indistinguishable from the high-FRET fraction measured for Ndc80 complexes alone, in the absence of GFP-MIND (Figures 3.11 A and B). These observations show that association of the Ndc80 complex with MIND inhibits tight bending of the Ndc80 complex.

3.4 DISCUSSION

In this study, we examined the functional significance of conformational changes of the Ndc80 complex. By using single molecule techniques, we show that the Ndc80 complex dynamically fluctuates around its hinge region, adopting both open and closed conformations. Tight bending leads to an auto-inhibited state that decreases microtubule affinity. We also show that MIND-binding relieves this auto-inhibition of the Ndc80 complex, which explains how MIND enhances its binding to microtubules. Our data uncovers a previously uncharacterized mechanism of

regulation of the Ndc80 complex that is distinct from the more well-known phospho-regulation of the complex.

We established that MIND opposes the tightly bent form of the Ndc80 complex, but precisely how this translates to increased microtubule binding, when MIND binds far away from the microtubule binding domains, is less clear. It is possible that the mechanism is similar to the auto-inhibition of kinesin-1: kinesin-1 bends around its loop to bring its tail in close proximity to its heads, thereby inhibiting motor activity of the heads (Kaan, Hackney, & Kozielski, 2011). Binding of the tail to cargo blocks its interaction with the heads, thereby relieving auto-inhibition and enabling processive motility. Like the cargo of kinesin-1, MIND binding to one end of the Ndc80 complex could simply block its interaction with the other end. However, our data suggest that MIND may be doing more than simply relieving auto-inhibition: while the Broccoli construct (which lacks the Spc24/Spc25 dimer and is not auto-inhibited) resides on the microtubule lattice longer than the full-length Ndc80 complex, the Ndc80-MIND co-complex has a residence time still roughly two-fold higher than Broccoli. This additional enhancement suggests that MIND might propagate a specific molecular reorganization to the Ndc80/Nuf2 end, through the coiled coil, to establish some preferred arrangement for microtubule binding. Allosteric communication through a coiled-coil has been seen, for example, in dynein (Carter et al., 2008).

Though previous literature determined that the Ndc80 complex is flexible (Wang et al., 2008) due to its internal loop region (Zhang et al., 2012) and can exist in both a bent and more open state (Tien et al., 2014), our data now show directly that it can readily adopt an extremely bent state, in which the two ends of the complex come within a few nanometers of each other. The loop region is required for this tight bending. The Ndc80 complex is commonly drawn as a

rigid rod containing a single, distinct hinge point that coincides with the loop region, which is located roughly 20 nm from the Ndc80/Nuf2 end and 40 nm from the Spc24/Spc25 end of the complex (Wang et al., 2008). Given these distances, a simple hinging about the loop region would not bring the two ends close enough together to explain the high FRET values we observed (Wang et al., 2008). Thus, additional sites of flexibility must exist within the complex. Flexibility at the junction between the calponin homology domains and the hairpin/coiled coil region has been suggested based on the different configurations of this region seen in crystal structures (Ciferri et al., 2008; Valverde et al., 2016). Additional hinging at this second region might be sufficient to bring the two ends close enough to explain the high FRET.

Tight bending of the Ndc80 complex is important for its function *in vivo* (Tien et al., 2014) and our observations now show that this conformation is auto-inhibited. However, the physiological role of auto-inhibition remains uncertain. One attractive possibility is that it might prevent newly expressed Ndc80 complexes from interacting with microtubules prematurely, before the Ndc80 complexes are anchored at a kinetochore, thereby avoiding delay or potentially persistent mis-localization. Another, not mutually exclusive, idea is that auto-inhibition might ensure stepwise assembly of the outer kinetochore. Kinetochores are thought to assemble hierarchically, with the inner-most components assembling first and then outer components building sequentially upon them, according to their spatial arrangement (Musacchio & Desai, 2017). Such stepwise assembly would not occur if all components were continuously able to bind their partners with high affinity. However, it could be explained by a sequential relief of auto-inhibition as each component assembles onto a nascent kinetochore. Previous work shows that tight binding of MIND to its kinetochore receptors, Ame1 and Mif2, is prevented by auto-inhibition, presumably until MIND binds a nascent kinetochore, where its auto-inhibition can be

relieved by Aurora phosphorylation. Similarly, the auto-inhibition of Ndc80 complex might prevent it from recruiting the Dam1 complex until it is bound to kinetochore-anchored MIND. Sequential relief of auto-inhibition might be a general mechanism that encodes stepwise construction at various sites within the kinetochore (Dimitrova, Jenni, Valverde, Khin, & Harrison, 2016a; Petrovic et al., 2016a).

Some Ndc80 complex is localized to kinetochores independently of the MIND complex and anchored instead via Cnn1/CENP-T (Malvezzi et al., 2013). Determining whether or not Cnn1 binding promotes opening of the Ndc80 complex and relieves its auto-inhibition could be an interesting area for future work. If some kinetochore-anchored Ndc80 complexes can adopt the tightly bent state, then their conformation might be sensitive to kinetochore tension, potentially contributing to the mechanosensory feedback mechanisms that are thought to control error correction and checkpoint signaling at kinetochores.

3.5 Acknowledgments

We thank Kimberly Fong, Eric Muller, King Yabut, Amanda Clouser and the Zagotta Lab for technical assistance and advice. We thank Simon Jenni of the Harrison Lab for sharing the Ndc80 complex model. We also thank the members of the T.N.D. laboratory, C.L.A. laboratory, and Seattle Mitosis Club for helpful discussions.

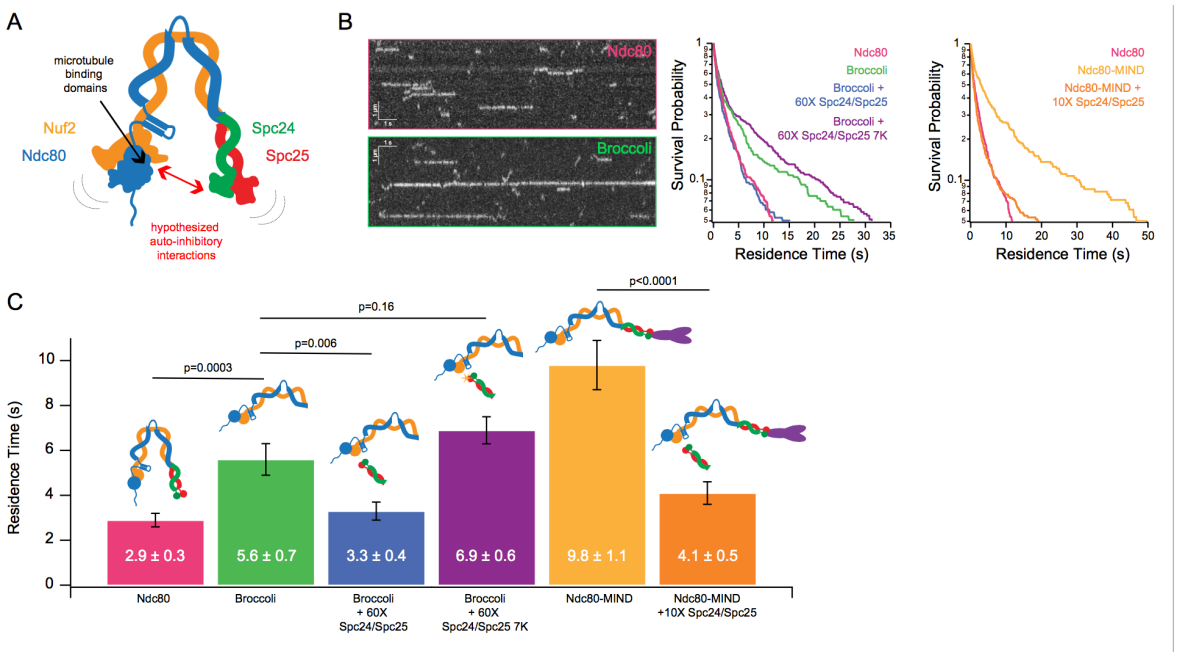

Figure 3.1. Ndc80 complex microtubule binding is auto-inhibited by the Spc24/Spc25 dimer.

A. Schematic of hypothesized model of auto-inhibition of the Ndc80 complex. Red arrow indicates hypothesized regions of intra-complex interactions. Black arrow indicates calponin homology domains on the Ndc80/Nuf2 dimer responsible for microtubule binding. B. (Left) Representative kymographs of Ndc80 and Broccoli. (Right) Survival probability curves of residence times of the Ndc80 complex (n=537), Broccoli (n=315), Broccoli+60X Spc24/Spc25 (n=398), Broccoli+60x Spc24/Spc25 7K (n=586) and the Ndc80 complex (repeated), Ndc80-MIND (n=279), Ndc80-MIND+10X Spc24/Spc25 (n=674). C. Bar graph of average residence times of the data represented in survival probability curves in Figure 1 B. Error was calculated using bootstrapping analysis. p values were calculated using a two-tailed Student's *t* test.

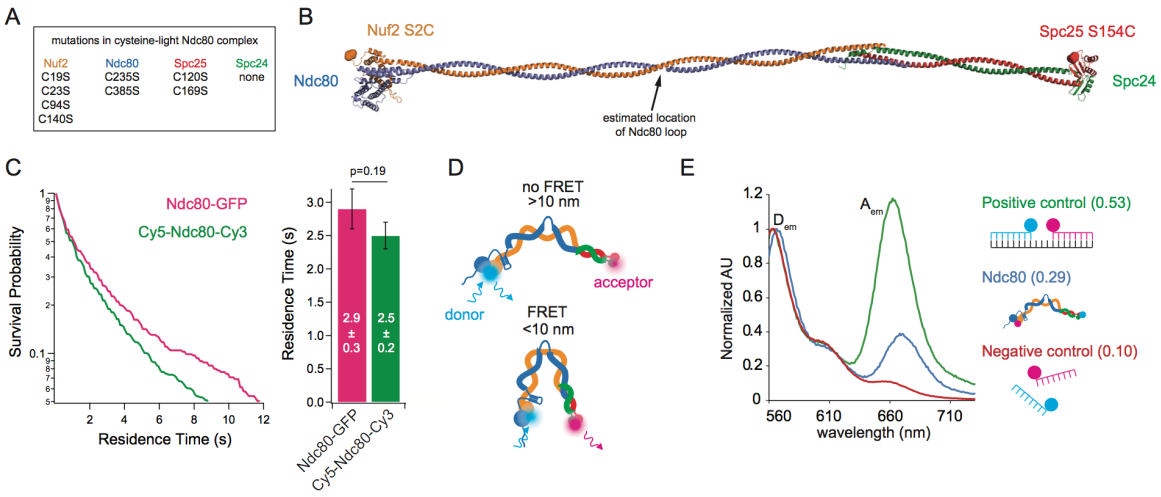

Figure 3.2. The Ndc80 complex can tightly bend.

A. List of mutations made in the wild type Ndc80 complex to generate cysteine-light construct. B. Model of the Ndc80 complex using the dwarf tetramer structure (DOI: 10.2210/pdb5TCS/pdb) plus inserted coiled coil between the tetramerization domain and globular domain of each dimer. Break in coiled coil indicates estimated location of Ndc80 loop, indicated by black arrow. Colored balls on each globular domain of the model indicate location of the cysteine residues (Nuf2 S2C, Spc25 S154C) used for dual end-labeling. C. (Left) Survival probability curves of residence times for Ndc80-GFP (data repeated from Figure 1 B) (pink trace) and end-labeled Cy5-Ndc80-Cy3 (green trace). (Right) Bar graph of average residence times of the data at left. Error was calculated using bootstrapping analysis. p value was calculated using a two-tailed Student's *t* test. D. Cartoon of approximate dye locations on the Ndc80 complex illustrating that in a more open conformation (Top), FRET would not occur. In a tightly bent conformation (Bottom), the dyes would be in close proximity and exhibit FRET. E. Bulk FRET spectra of positive control double-stranded, dually-labeled oligonucleotide, negative control single-stranded singly-labeled oligonucleotides or end-labeled Ndc80 complex Nuf2 S2C Spc25 S154C. Displayed is the emission spectra of each construct from 560 nm to 730 nm under 550 nm (Cy3, donor) excitation. D_{em} and A_{em} denote the emission peaks of the donor (Cy3) and acceptor (Cy5). Values in parentheses indicate calculated relative FRET efficiency.

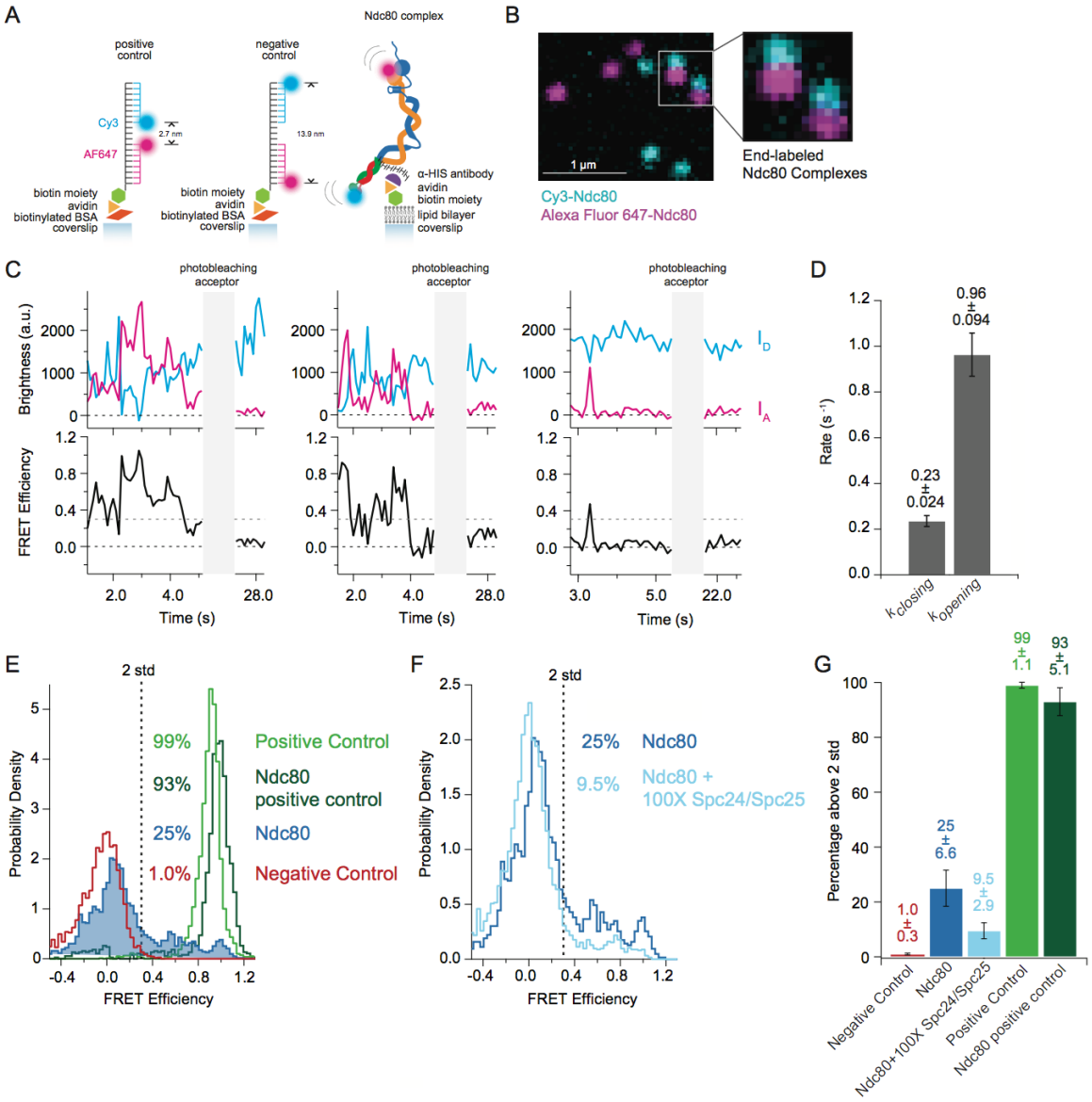

Figure 3.3. The Ndc80 complex fluctuates between tightly bent and more open conformations.

A. (Left) Cartoon depicting method of tethering labeled control oligonucleotides to glass coverslip. (Left and middle) Cartoons show the distance in nanometers between FRET pair dyes for positive and negative control oligonucleotides. (Right) Cartoon depicting method of tethering end-labeled Ndc80 complex to coverslip via lipid bilayer. B. Fluorescence image showing coverslip decorated with end-labeled Ndc80 Nuf2 S2C Spc25 S154C complexes. Zoom-in shows two Ndc80 complexes with both dyes present. Colors are off-set vertically. C. (Top) Fluorescence traces for three examples of end-labeled Ndc80 complexes (first two panels, Ndc80 Nuf2 S2C Spc24 N185C, last panel Ndc80 Nuf2 S2C Spc25 S154C) before and after acceptor (Alexa Fluor 647) photobleaching. (Bottom) Corresponding traces of FRET efficiency before and after photobleaching acceptor for each top example. Black dotted line indicates 0.0 FRET efficiency. Gray dotted line indicates threshold (0.30) used for two-state thresholding analysis.

D. Bar graph of switching rates calculated for Ndc80 complex Nuf2 S2C Spc25 S154C from a two-state thresholding analysis. E. Histograms of FRET values for positive oligonucleotide control (n=2699, 75 particles), Ndc80 Spc25 S154C G177C positive control (n=1275, 60 particles), Ndc80 complex Nuf2 S2C Spc25 S154C (n=2099, 85 particles) and negative oligonucleotide control (n=3833, 154 particles). Percentage values represent the percentage of FRET values 2 standard deviations away from the mean of a Gaussian fit to the negative oligonucleotide data. “n” refers to each 0.1 second FRET measurement for each condition. F. Histograms of FRET values for Ndc80 complex Nuf2 S2C Spc25 S154C (n=2099, 85 particles) (repeated from Figure 3E) and Ndc80 complex Nuf2 S2C Spc25 S154C + 100X Spc24/ Spc25 (n=4137, 152 particles). Percentage values represent the percentage of FRET values 2 standard deviations away from the mean of a Gaussian fit to the negative oligonucleotide data. “n” refers to each 0.1 second FRET measurement for each condition. G. Bar graph of the percentage of FRET values above 2 standard deviations away from the mean of a Gaussian fit to the negative oligonucleotide data. Error calculated as standard error of the mean of day to day variability of percentage above two standard deviations.

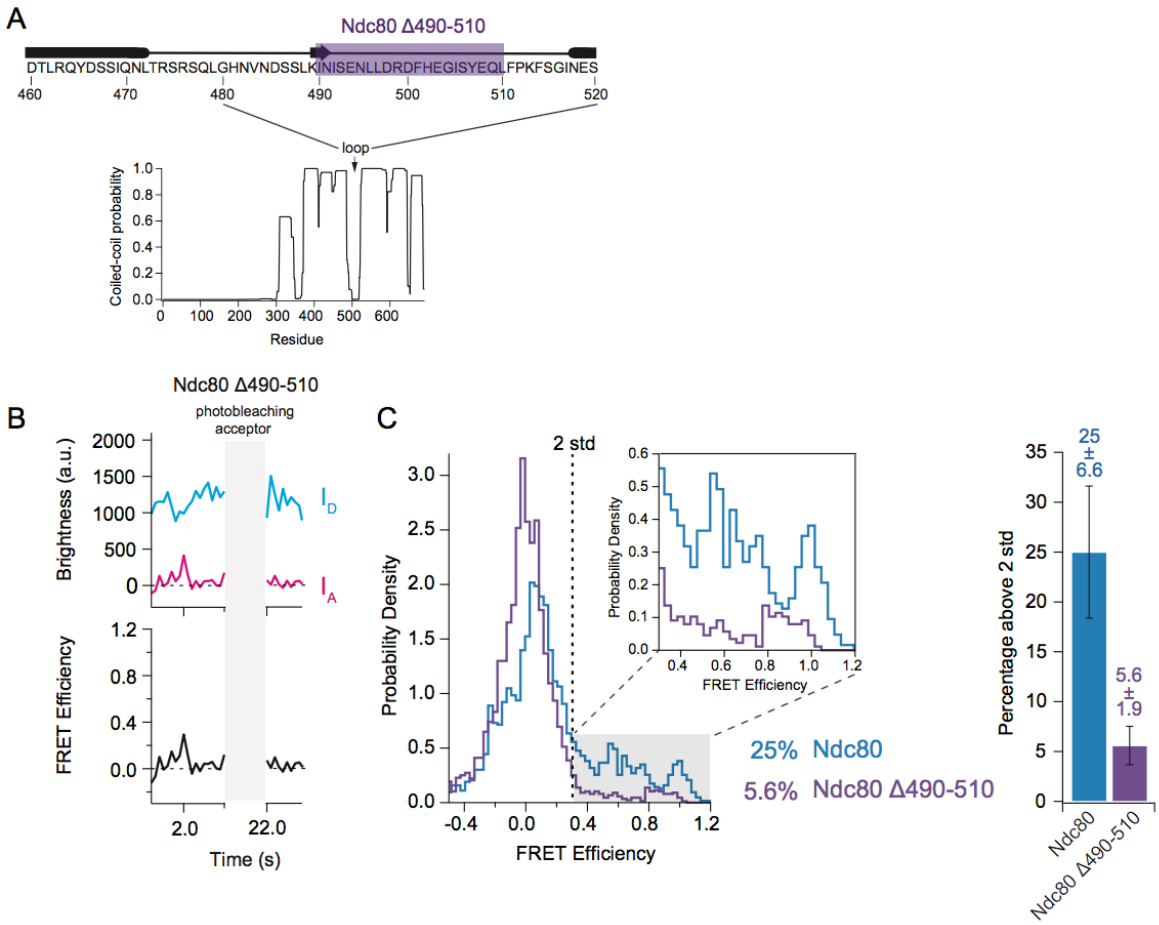

Figure 3.4. The loop region of Ndc80 contributes to tight bending of the complex.

A. (Top) Primary sequence of Ndc80 protein amino acids 460-520. The purple bar highlights the region of the loop deleted for the following experiment. (Bottom) Graph of probability of coiled-coil as predicted by PCOILS of the Ndc80 protein. B. (Top) Fluorescence traces of one representative example of an end-labeled Ndc80 complex in Figure 4C before and after photobleaching acceptor (Alexa Fluor 647). (Bottom) Corresponding traces of FRET efficiency before and after acceptor photobleaching for the top example. C. (Left) Histograms of FRET values for Ndc80 complex Nuf2 S2C Spc25 S154C (n=2099, 85 particles) (data repeated from Figure 3E, 3F) and Ndc80 complex Ndc80 Δ490-510 Nuf2 S2C Spc25 S154C (n=2926,143 particles). Percentage values represent the percentage of FRET values 2 standard deviations away from the mean of a Gaussian fit to the negative oligonucleotide data. “n” refers to each 0.1 second FRET measurement for each condition. Zoom in of histograms depicting FRET values over two standard deviations. (Right) Bar graph of the percentage of FRET values above two standard deviations. Error calculated as standard error of the mean of day to day variability of percentage above two standard deviations.

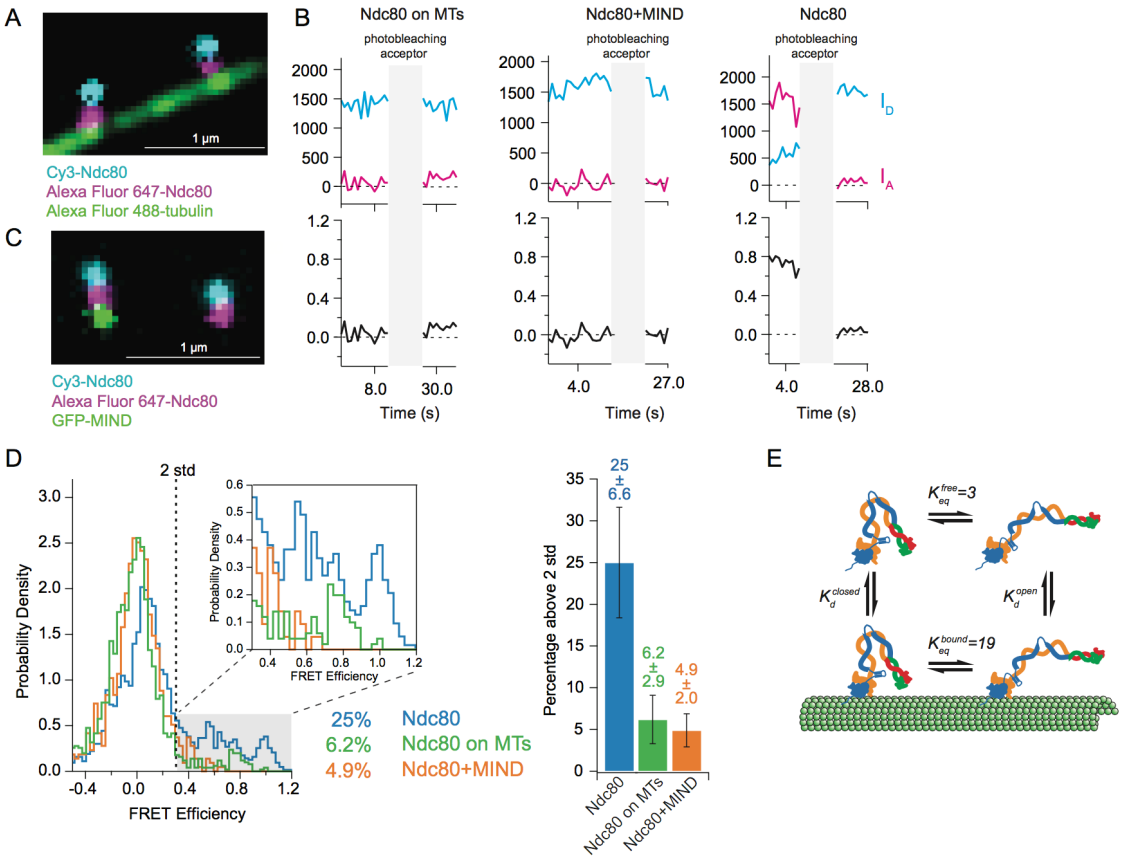

Figure 3.5. Tight bending of the Ndc80 complex is opposed by binding to either microtubules or the MIND complex

A. Fluorescence image of two end-labeled Ndc80 complexes (Nuf2 S2C Spc25 S154C) on Alexa Fluor 488 labeled-microtubules. Colors are off-set vertically. B. (Top) Fluorescence traces of one representative example of an end-labeled Ndc80 complex in each condition shown in Figure 5D before and after photobleaching acceptor (Alexa Fluor 647). (Bottom) Corresponding traces of FRET efficiency before and after acceptor photobleaching for each top example. C. Fluorescence image of two end-labeled Ndc80 complexes (Nuf2 S2C Spc25 S154C) next to each other on one coverslip, colocalized with MIND-GFP on the left, but not on the right. Colors are off-set vertically. D. (Left) Histograms of FRET values for Ndc80 complex Nuf2 S2C Spc25 S154C (n=2099, 85 particles) (data repeated from Figure 3E, Figure 4C), Ndc80 complex Nuf2 S2C Spc25 S154C on microtubules (n=1682, 91 particles) and Ndc80 complex Nuf2 S2C Spc25 S154C bound to MIND (n=718, 41 particles). Percentage values represent the percentage of FRET values 2 standard deviations away from the mean of a Gaussian fit to the negative oligonucleotide data. "n" refers to each 0.1 second FRET measurement for each condition. Zoom in of histograms depicting FRET values over two standard deviations. (Right) Bar graph of the percentage of FRET values above two standard deviations. Error calculated as standard error of the mean of day to day variability of percentage above two standard deviations. E. Diagram of equilibrium between open and closed conformations of the Ndc80 complex, on and off the microtubule. Estimation of K_{eq} values described in Materials and Methods.

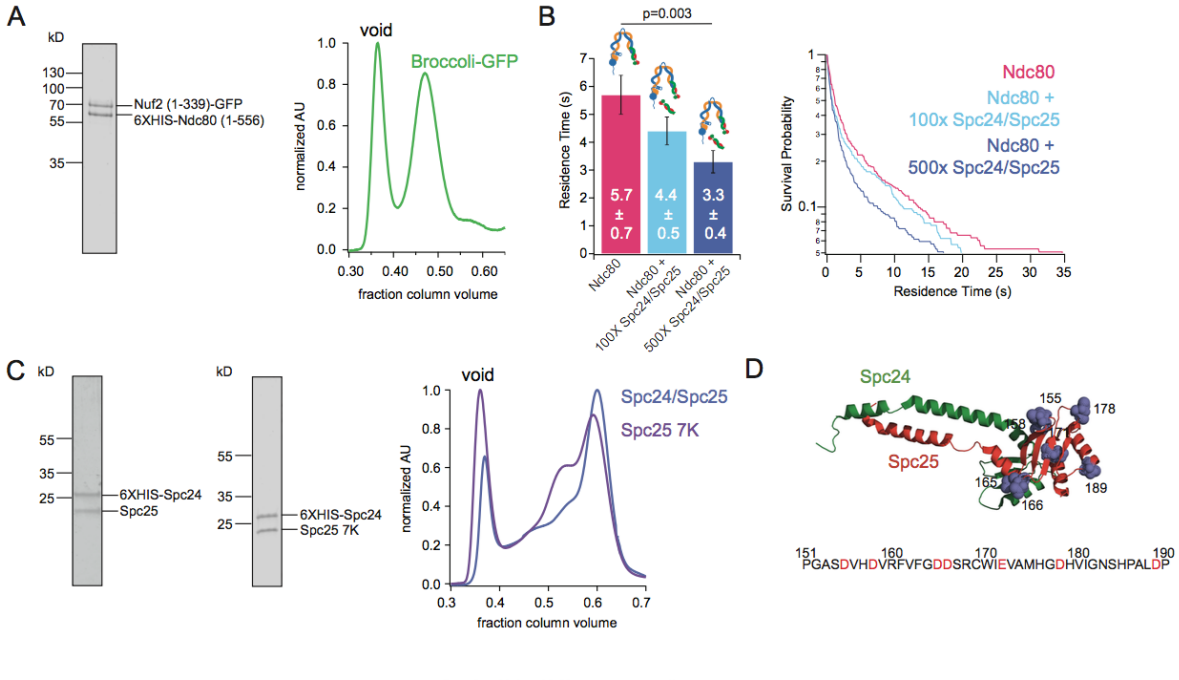

E

Spc25 (147-198) sequence alignment

```
                                   166                 178       189
Saccharomyces cerevisiae  LRVLPGASDVHDVRFVFGD-DSR-------CWIEVAMHGDHVIGNSHPALDPKSRATLEH
Homo sapiens              IRKIYG----EKLQFIFTNIDPKNPESPFMFSLHLNEARDYEVSDSAPHLE--GLAEFQE
Mus musculus              IRKIHG----NKLQFIFTSIDPKNPESPYMFSMSINEAKEYEVYDSSPHLE--CLAEFQE
Xenopus laevis            IRKLRG----DKLQFVFRCINPKDLDQPYSCIISLNAEGDYEVAGCDPPLE--CIAEFQE
Gallus gallus             IRRIHN----EQLQFIFRHIDHKDPDKPYMFTLSINEQGDYEVTSCTPPLD--CISEFQL
                          :* : .     .:.*:*   : .       : :    :: : .. * *:    : ::
```

Figure 3.6. Purification of Ndc80 complex constructs

A. (Left) Coomassie blue-stained gel showing Broccoli-GFP. (Right) Representative Superdex 200 16/60 elution profile of Broccoli-GFP, normalized to highest peak. B. (Left) Bar graph of average residence times of the Ndc80 complex (n=537), Ndc80 complex+100X Spc24/Spc25 (n=370) and Ndc80 complex+500X Spc24/Spc25 (n=427). Error was calculated using bootstrapping analysis. (Right) Survival probability curves of the data represented in the bar graph to left. C. (Left) Coomassie blue-stained gel showing Spc24/Spc25. (Right) Representative Superdex 200 16/60 elution profiles of Spc24/Spc25 and Spc24/Spc25 7K, normalized to highest peak. D. (Top) Mutations made for Spc24/Spc25 7K shown as lilac space-filling models at position of corresponding amino acid on the structure of the budding yeast Spc24/Spc25 dimer (DOI: 10.2210/pdb5TCS/pdb). (Bottom) Primary sequence of budding yeast Spc25 from amino acid 151 to 190 with residues in red indicating those mutated to lysine. E. Multiple sequence alignment of Spc25 generated using EMBL-EBI MUSCLE. *Saccharomyces cerevisiae* Spc25 primary amino acid sequence shown from 147-198, with alignments below. Red bars and amino acid number indicate subset of acidic residues mutated to lysine in Supplemental Figure 1 D that are highly conserved between organisms. " * " indicates positions with fully conserved residue. " : " indicates conservation between groups of strongly similar properties. " . " indicates conservation between groups with weakly similar properties.

A

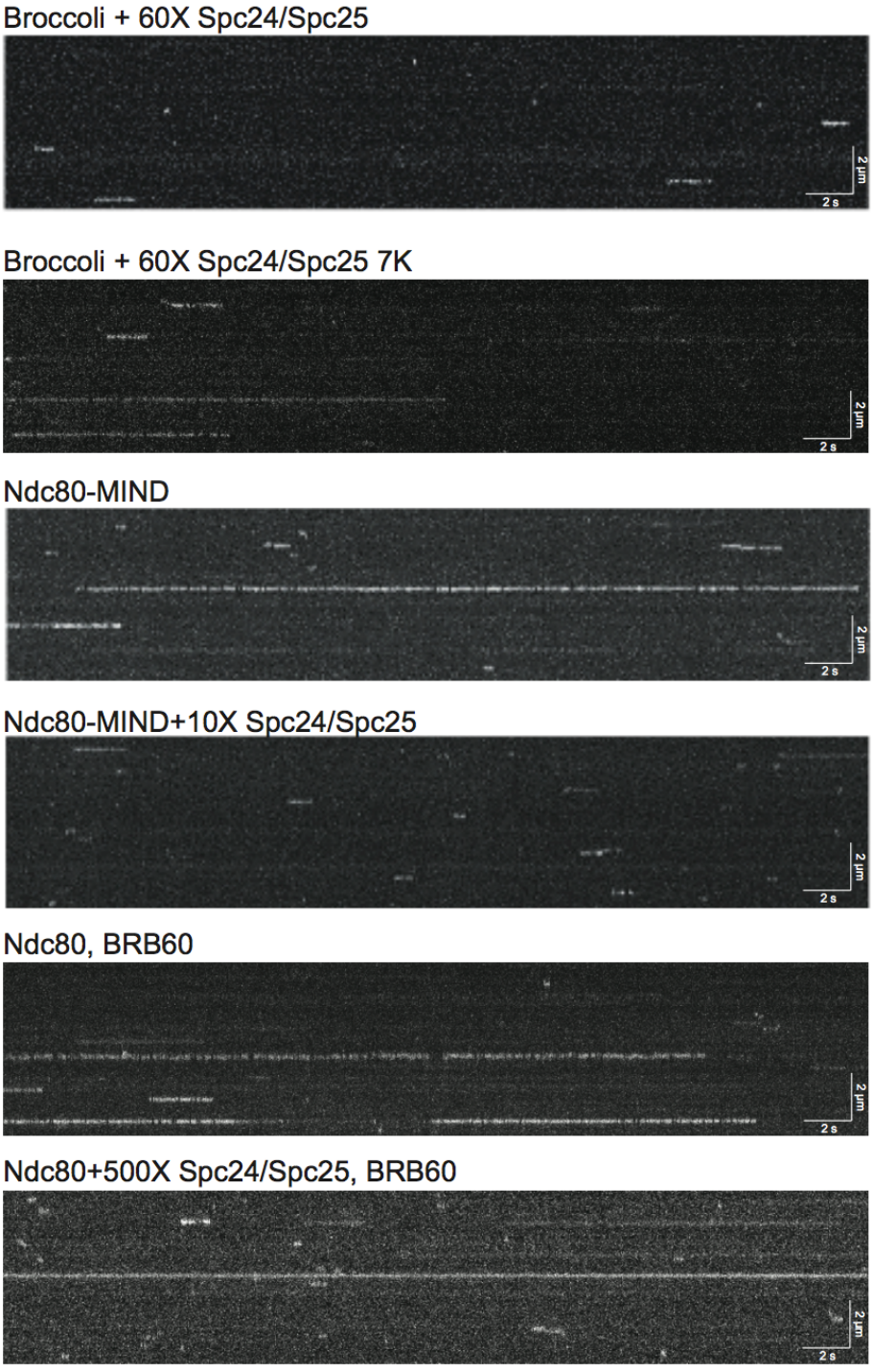

Figure 3.7. Representative kymographs of TIRF microscopy assays

A. Representative kymographs of each condition measured in Figure 1 B, C. Brightness and contrast have been adjusted separately for each image for best visualization.

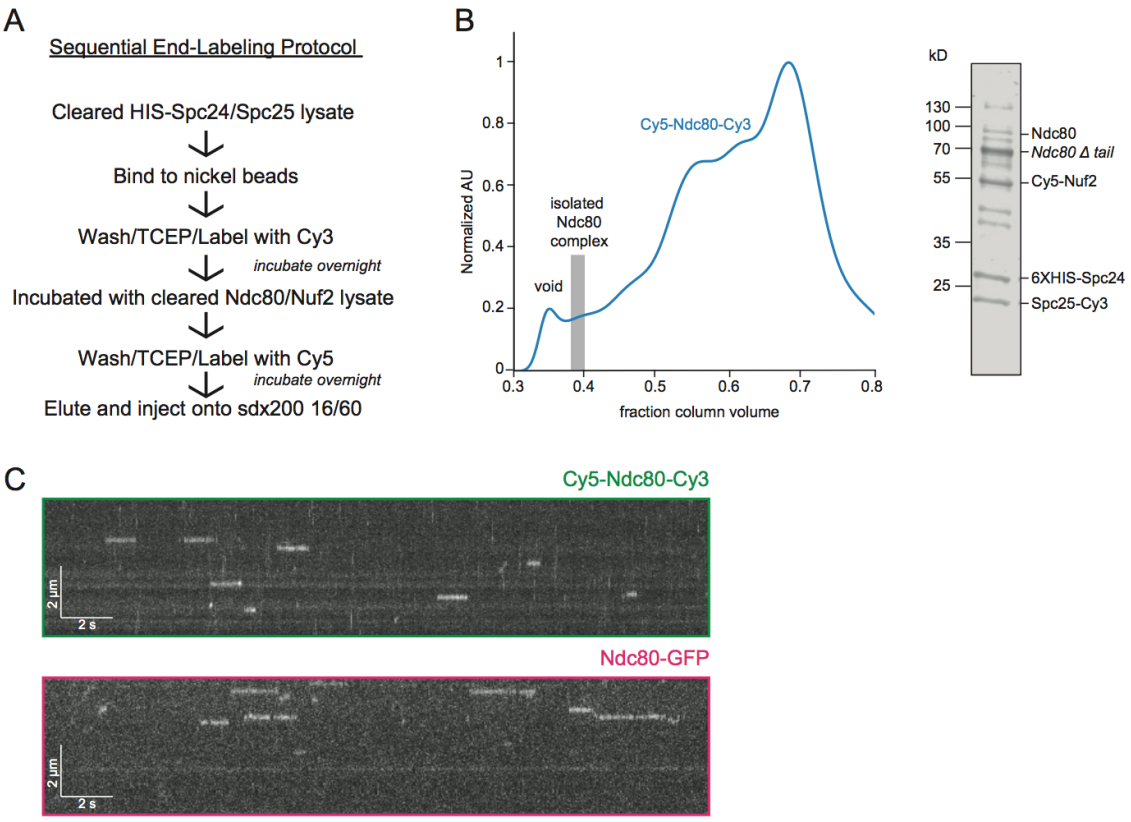

Figure 3.8. A functional Ndc80 complex can be sequentially end-labeled.
A. Schematic of sequential end-labeling procotol for the Ndc80 complex used in bulk FRET assay. B. (Left) Representative Superdex 200 16/60 elution profiles of end- labeled Ndc80 complex (Nuf2 S2C, Spc25 S154C) (blue trace) used in bulk FRET assay normalized to highest peak. Gray bar shows SEC fractions collected. (Right) Coomassie blue-stained gel showing end-labeled Ndc80 complex used in bulk FRET assay (SEC fraction shown as gray bar in elution profile to the left). Sequential overnight incubation with dyes leads to greater complex degradation, especially of the N-terminal tail on the Ndc80 protein, as seen in gel. D. Representative kymographs of Cy5-Ndc80-Cy3 (green box) and Ndc80-GFP (pink box).

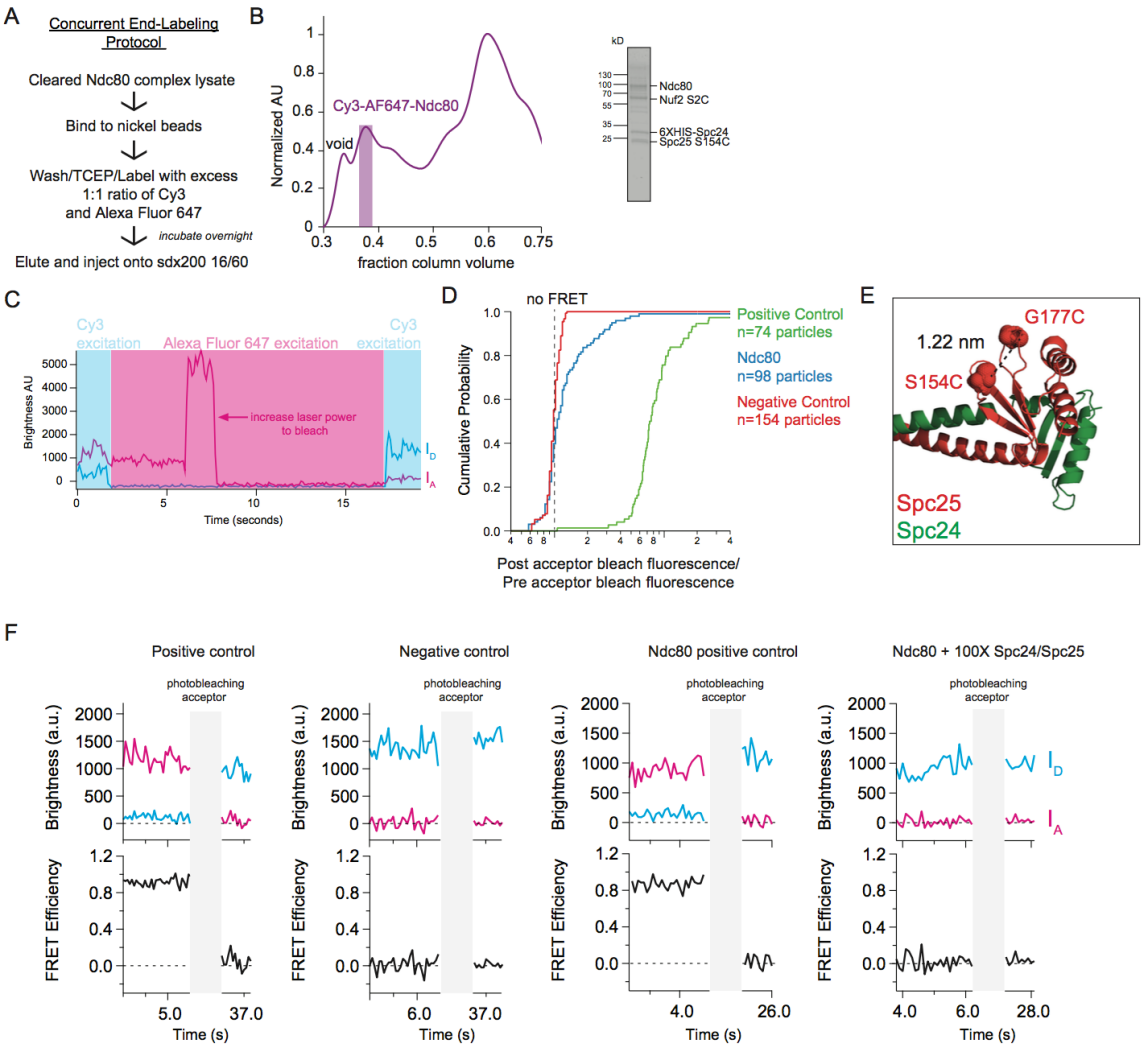

Figure 3.9. Concurrent labeling of the Ndc80 complex for single molecule FRET assays.

A. Schematic of concurrent end-labeling procotol for Ndc80 complex constructs used in single molecule FRET assays. B. (Left) Representative Superdex 200 16/60 elution profile of end-labeled Ndc80 complex (Nuf2 S2C Spc25 S154C), normalized to highest peak. Purple bar shows SEC fractions collected. (Right) Coomassie blue-stained gel showing end-labeled Ndc80 complex used in single molecule FRET assay (SEC fraction shown as purple bar in elution profile to the left). C. Example of acceptor bleaching protocol used for the single molecule FRET assay, with Ndc80 Nuf2 S2C Spc25 S154C exhibiting FRET. After an initial period of donor excitation (light blue box), where direct FRET measurements are gathered, the acceptor is directly excited at the same power as the donor excitation, and then increased to a higher power to bleach (pink box). Finally, the donor is re-excited. Blue line indicates brightness trace of donor, Cy3. Pink line indicates brightness trace of acceptor, Alexa Fluor 647. D. Cumulative probability curves for positive oligonucleotide control, Ndc80 complex Nuf2 S2C Spc25 S154C and negative oligonucleotide control of ratio of post acceptor beach fluorescence over pre-acceptor bleach fluorescence. Fluorescence values used to calculate ratio are averages of all Cy3

fluorescence values under direct excitation before and after acceptor bleaching. E. Crystal structure of yeast Spc24/Spc25 dimer (DOI: 10.2210/pdb5TCS/pdb). Space-filling model of residues Spc25 154 and Spc25 177 illustrate locations of cysteine mutations made for Ndc80 complex positive control. Dotted lines shows distance in nanometers between the two residues. F. (Top) Fluorescence traces of one representative example of a positive oligonucleotide control, negative oligonucleotide control, Ndc80 complex positive control (Ndc80 Spc25 S154C G177C) and Ndc80 complex + 100X Spc24/Spc25 before and after photobleaching acceptor (Alexa Fluor 647). (Bottom) Corresponding traces of FRET efficiency before and after photobleaching acceptor for each top example.

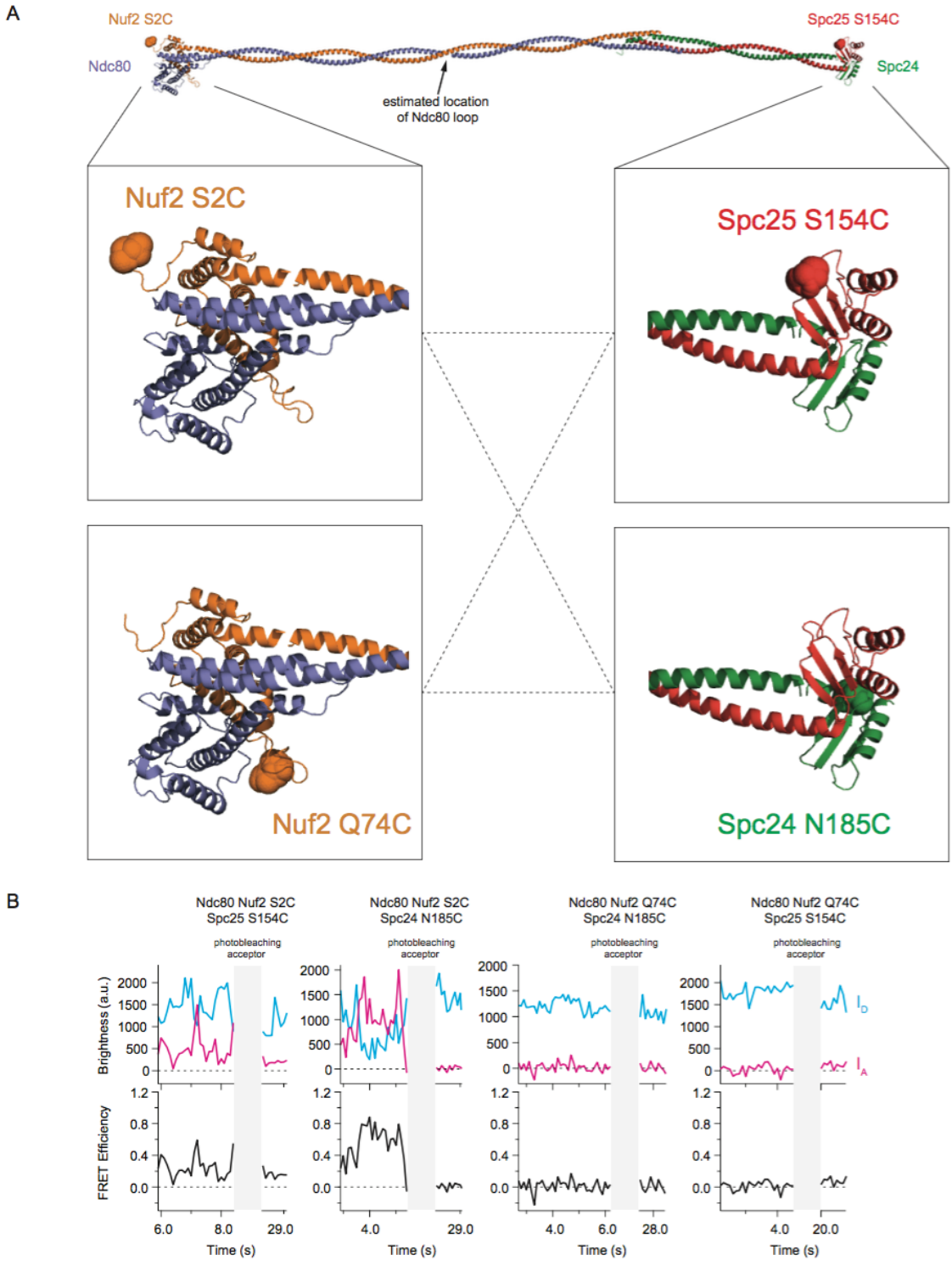

Figure 3.10. The Ndc80 complex has preferred orientations for intra-complex interactions.

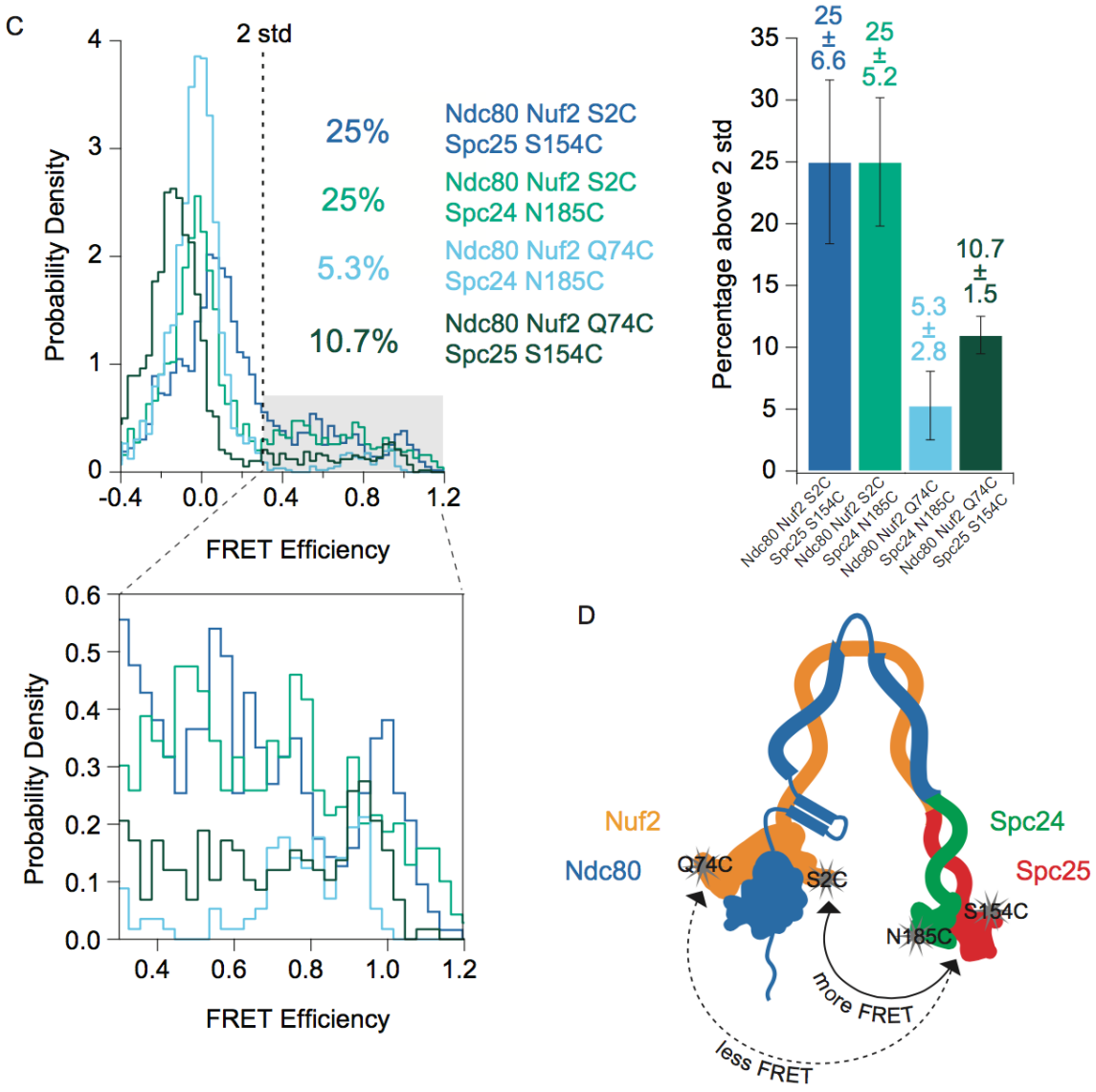

Figure 3.11. The Ndc80 complex has preferred orientations for intra-complex interactions.

A. Model of the Ndc80 complex using the dwarf tetramer structure (DOI: 10.2210/pdb5TCS/pdb) plus inserted coiled coil between the tetramerization domain and globular domain of each dimer. Break in coiled coil indicates estimated location of Ndc80 loop, as indicated by black arrow. Full-length model at top shows main Ndc80 complex construct (Nuf2 S2C, orange balls and Spc25 S154C, red balls) used throughout experiments. Zoomed in cut-outs below show all four cysteine locations used for dye placement, with dotted lines showing all four combinations of Ndc80 complex dye pairs constructed. B. (Top) Fluorescence traces for one representative example of each combination of dye pairs for end-labeled Ndc80 complexes before and after photobleaching acceptor (Alexa Fluor 647) . (Bottom) Corresponding traces of FRET efficiency before and after photobleaching acceptor for each top example. C. (Left Top) Histograms of corrected FRET values for Ndc80 complex Nuf2 S2C Spc25 S154C (n=2099, 85 particles) (data repeated from Figure 3E, Figure 4C, Figure 5D), Ndc80 complex

Nuf2 S2C Spc24 N185C (n=2319, 79 particles), Ndc80 complex Nuf2 Q74C Spc24 N185C (n=1885, 63 particles) and Ndc80 complex Nuf2 Q74C Spc25 S154C (n=1941, 72 particles). Percentage values represent the percentage of FRET values 2 standard deviations away from the mean of a Gaussian fit to the negative oligonucleotide data. “n” refers to each 0.1 second FRET measurement for each condition. (Left Bottom) Zoom in of histograms depicting FRET values over two standard deviations. (Right Top) Bar graph of the percentage of FRET values above two standard deviations. Error calculated as standard error of the mean of day to day variability of percentage above two standard deviations. D. Cartoon depicting locations of all four dye locations on a bent Ndc80 complex. When the dye is located on Nuf2 S2C, regardless of the dye location on the Spc24/Spc25 dimer, the Ndc80 complex exhibits more FRET relative to when the dye location on Nuf2 is Q74C.

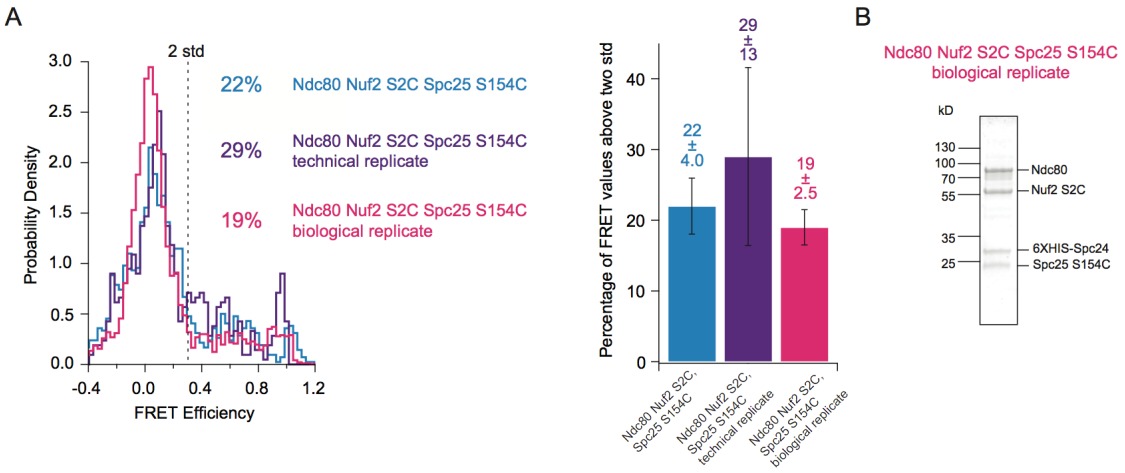

Figure 3.12. Reproducibility of Ndc80 complex single molecule FRET measurements.

A. (Left) Histograms of corrected FRET values for Ndc80 complex Nuf2 S2C Spc25 S154C (n=1395, 48 particles), Ndc80 complex Nuf2 S2C Spc25 S154C measured from slides with MIND-GFP, but not associated with MIND (n=704, 37 particles), and a separate protein and labeling prep of Ndc80 complex Nuf2 S2C Spc25 S154C (n=3224, 108 particles). Percentage values represent the percentage of FRET values 2 standard deviations away from the mean of a Gaussian fit to the negative oligonuleotide control. "n" refers to each 0.1 second FRET measurement for each condition. (Right) Bar graph of the percentage of FRET values above two standard deviations. Error calculated as standard error of the mean of day to day variability of percentage above two standard deviations. C. Coomassie blue-stained gel showing a separate protein and labeling prep of Ndc80 complex Nuf2 S2C Spc25 S154C.

Chapter 4. CHALLENGES OF USING *IN VIVO* FRET TO PROBE KINETOCHORE COMPLEX INTERACTIONS[3]

4.1 INTRODUCTION

During mitosis, chromosomes attach to microtubules emanating from the mitotic spindle poles and are pulled to opposite sides of the cell in order to equally segregate the genetic material. Kinetochores provide this linkage between chromosomes and highly dynamic microtubules. The kinetochore-microtubule attachment serves as an error correction mechanism that delays the cell cycle when erroneous microtubule attachments are detected (Biggins, 2013). Moreover, kinetochores must be able to withstand the application of forces over long periods of time while staying securely attached to growing and shrinking microtubules (Cheeseman, 2014).

In budding yeast, kinetochores are comprised of 40 proteins organized into complexes that form a hierarchy spanning the microtubule-DNA interface (Biggins, 2013). *In vitro* reconstitution of these components is valuable in that it allows us to specifically probe the component's unique contribution to the functions of the kinetochore as a whole. However, *in vitro* work is, by definition, limited in the sense that it occurs outside of the context of the cell, and thus one risks losing biologically relevant information. For instance, phosphorylation regulates many inter-complex interactions within the kinetochore, but this mode of regulation is not preserved when using recombinant protein purified from *E. coli* (Akiyoshi et al., 2013; Petrovic et al., 2016b; Sarangapani et al., 2013).

The Ndc80 complex is a heterotetrameric microtubule-binding complex in the outer kinetochore, consisting of two globular domains joined by a highly elongated coiled-coil region

[3] This section is not adapted from a publication in a scientific journal. The work in this section was performed independently.

(Lampert et al., 2013; McCleland et al., 2003). This coiled-coil region is disrupted by a flexible loop, which imparts a high degree of flexibility to the Ndc80 complex (Wang et al., 2008). The Ndc80 complex is a hub of function within the kinetochore and is directly involved in force generation and maintenance during microtubule polymerization and depolymerization, the mechanical linkage between the end-on attachments of microtubules to the rest of the kinetochore assembly, and additional vital functions within the kinetochore (Powers et al., 2009). The Dam1 complex is also found in the *S. cerevisiae* outer kinetochore and forms oligomeric rings *in vitro* (and *in vivo,* though partial rings are the dominant species) around the microtubule that help to mediate the Ndc80 complex's end-on attachment to microtubules (Ng et al., 2018; Tien et al., 2010; Umbreit et al., 2014). The Dam1 complex increases the lifetime of the Ndc80 complex's binding to the microtubule lattice (Umbreit et al., 2014). It has been suggested by multiple groups in the field that the Ndc80 complex binds one oligomeric ring of the Dam1 complex during budding yeast metaphase (Aravamudhan et al., 2015; Cheeseman & Desai, 2008; K. Tanaka, Kitamura, Kitamura, & Tanaka, 2007). However, *in vitro* work from our lab strongly suggests that the Ndc80 complex uses three separate interaction sites contained within two distinct locations on the complex (one near the hairpin loop and one between the flexible loop region and C-terminus of the Ndc80 protein) to bind up to two Dam1 complex oligomeric rings (Kim et al., 2017). Additionally, we found that a more inner kinetochore component, the MIND complex, can also increase the residence time of the Ndc80 complex on the microtubule lattice *in vitro* (Kudalkar et al., 2015). Yet, the Dam1 complex and MIND appear to activate the Ndc80 complex by dissimilar mechanisms, as suggested by their additive affect on increasing Ndc80 microtubule binding (Kudalkar et al., 2015).

The Ndc80 complex displays a variety of conformations in negative stain electron

micrographs (Wang et al., 2008; Zhang et al., 2012) and crystallized forms (Ciferri et al., 2008; Valverde et al., 2016). Studies suggest that its flexibility is important *in vivo* (Joglekar et al., 2009; Maure et al., 2011; Tien et al., 2014; Wang et al., 2008), and that both its tightly bent and more straightened conformations are necessary for the proper progression of mitosis (Tien et al., 2014). Based upon genetic evidence and *in vitro* single molecule data, we posited that MIND binding opposes a tightly bent (auto-inhibited) form of the Ndc80 complex, stabilizing a more open conformation during metaphase that leads to better microtubule binding once Ndc80 is assembled at the kinetochore (Kudalkar et al., 2015). We further hypothesized that this more open conformation would allow the Ndc80 complex to bind two Dam1 complex rings during metaphase, whereas at anaphase, a bending of the Ndc80 complex would occur such that the complex could bind only one Dam1 complex ring. Thus, we sought to characterize Ndc80-Dam1 complex interactions over the course of mitosis in live budding yeast.

Förster resonance energy transfer (FRET) is a mechanism of energy transfer between two fluorophores that is dependent on the distance between the fluorophores: it is a commonly used method to quantify distances in the cell. We reasoned that we could use *in vivo* FRET in order to map the distances of protein-protein interactions between and within the Ndc80 and Dam1 complexes. First, homologous recombination in budding yeast allows for relatively easy and fast fluorescent tagging of proteins at their endogenous loci: a PCR product containing the gene of interest with any desired modifications flanked by 50-60 base pairs of sequence homologous to the chromosomal site of insertion is transformed into yeast. Second, previous work in our lab elucidated a low resolution model of the Dam1 complex through cross-linking/mass spectrometry data, which could be used to inform where best to tag proteins (Zelter et al., 2015). Finally, this approach was previously used by our lab to establish the organization of the budding

yeast spindle pole body (Muller et al., 2005). Consequently, we considered this technique to be highly amenable to probe Ndc80-Dam1 complex interactions *in vivo*.

4.2 MATERIALS AND METHODS

Media and Strains

The compositions of synthetic dextrose minimal medium (SD), SD-complete (SDC), and yeast peptone dextrose-rich broth medium (YPD) are described in (Sundin, Chiu, Riffle, Davis, & Muller, 2004). All strains are derived from W303 (ade2-1oc, can1-100, his3-11,15, leu2-3112, trp1-1, ura3-1) and listed in Table 4.1. They share the W303 genetic markers except for the noted introduction of CFP or YFP gene cassettes fused to the targeted genes and in some cases are TRP1 and cyh^R. The gene cassettes were introduced by standard procedures (Hailey, Davis, & Muller, 2002). The C-terminal YFP cassette was inserted with either G418 (gene amplified from plasmid pDH6) or HIS3 (pDH5) selection. The C-terminal CFP cassette was inserted with either G418 (pDH3) or hygromycin-B (pBS4) selection. N-terminal fusions were introduced following the procedures of (Prein, Natter, & Kohlwein, 2000) using either plasmid pDH22 or pBS5 for the insertion of YFP or CFP, respectively. Primers for amplification were synthesized by IDT (Coralville, IA). Plasmids and standard procedures are fully described at the web site for the Yeast Resource Center (http://depts.washington.edu/~yeastrc/p_p_home.htm).

Fluorescence Microscopy

Endogenous tagging of fluorophores followed the method developed in (Longtine et al., 1998). Fresh cells were grown on solid YPD medium supplemented with additional 3× adenine overnight at 30°C. Microcolonies were scraped off the plate and suspended in 30 µl of SDC medium. A 3–4-µl aliquot was mounted on a pad of 0.9% SeaKem LE agarose (FMC

BioProducts, Rockland, ME) in SDC as described in (Sundin et al., 2004). Microscopy was performed on a DeltaVision system manufactured by Applied Precision (Issaquah, WA). The microscope was equipped with an IL-70 (Olympus, Tokyo, Japan), an Uplan Apo 100× oil objective (1.35 NA), a CoolSnap HQ digital camera from Roper Scientific (Tucson, AZ), and optical filter sets from Omega Optical (Brattleboro, VT). The 100 W mercury arc lamp was changed when YFP photosensor values dropped below 550,000 or after 150 h of usage, whichever came first. For each strain 60–100 images were captured. Exposure times were 0.4 s with 2 × 2 binning and a final image size of 512 × 512. Fields were focused manually using DIC followed by an automated capture of a single focal plane of YFP, FRET, CFP, and DIC images. The order of capture was critical because YFP photobleaches rapidly when exposed to the CFP excitation light (Hailey et al., 2002).

FRET analysis

12-bit images were converted into 16-bit Tiff format by the Java program R3DConverter (Ess, Riffle, and Muller, unpublished; as described in (Kollman et al., 2008)). The Tiff images were then analyzed by a custom Matlab program, FretSCal, that selects regions of the image to evaluate based on user-defined criteria, such as local signal strength and decay (Ess, Riffle, and Muller, unpublished; as described in (Kollman et al., 2008)). Spillover_{CFP} and Spillover_{YFP} were determined by capturing images of strain JJY53 (CFP-Nuf2) and ESY1 (YFP-Ndc80) and dividing the background subtracted FRET channel by the background subtracted YFP or CFP channel. To ensure the most reliable estimates for the spillover factors, images were captured each day experimental strains were imaged and those spillover factors were then applied individually to the data sets for that day. Over seven days, the average Spillover_{CFP} was 0.97 ± 0.16 and the average Spillover_{YFP} was 0.22 ± 0.06. FRET_R was calculated by dividing the

background corrected FRET channel image by SpilloverTotal as described in (Muller et al., 2005).

4.3 RESULTS

The Ndc80 complex and Dam1 complex are compatible with endogenous fluorophore tagging

We chose CFP and YFP as the FRET pair to specifically tag various Ndc80 and Dam1 complex proteins *in vivo*. Eleven strains were created with unique pairwise combinations of CFP and YFP tagged Ndc80 complex and Dam1 complex proteins (Table 4.1). Placement of the fluorophores was guided by a published model of the Dam1 complex on the microtubule lattice (Zelter et al., 2015) (Fig. 4.1). We reasoned that the C-termini of the proteins Spc34, Ask1, Dad1 and Dad4 within the Dam1 complex appeared to extend away from the main part of the complex, allowing greater solvent accessibility and flexibility, perhaps facilitating interactions with a neighboring Dam1 complex ring. Within the strains, the CFP or YFP tagged version of the protein was the only version of the protein present in the cell. Each CFP or YFP was linked to the protein of interest through a Gly-Ala-Gly-Ala-Gly-Ala linker to help mitigate any possible steric hindrance or disruption to the kinetochore architecture and consequently, functionality. The following were tagged: 1) N-termini of Ndc80 and Nuf2 and 2) C-termini of Ndc80 (with both CFP and YFP), Nuf2, Spc24, Spc25, Dad1, Dad4 (with both CFP and YFP), Spc34 and Ask1. All strains were viable and exhibited normal growth by estimation of colony size.

Positive and negative FRET controls at the kinetochore show predicted FRET values

As a proof of principle that our measurements at the kinetochore accurately reported energy transfer, we used the well-characterized Ndc80 complex to create three positive FRET controls and one negative FRET control. We created strains that included Spc24-YFP/Spc25-CFP,

Ndc80-YFP/Nuf2-CFP and YFP-Ndc80/CFP-Nuf2. As expected, Spc24-YFP/Spc25-CFP lead to a very high FRET signal (1.93 ± 0.35), the highest measured of any strain tested, and comparable to those strains tested in a previous similar study and categorized as "high" FRET (Muller et al., 2005) (Fig. 4.2). Ndc80-YFP/Nuf2-CFP also exhibited FRET, though to a lesser extent (1.52 ± 0.22) (Fig. 4.2). YFP-Ndc80/CFP-Nuf2 exhibited the least amount of FRET of the three positive control strains (1.26 ± 0.2), though this wasn't necessarily unexpected (Fig. 4.2). The N-terminal tail of the Ndc80 complex is disordered and highly flexible, and thus the YFP would not always be "locked" into a high-FRET position close to the CFP on the N-terminus of Nuf2.

We created a strain including YFP-Ndc80/Nuf2-CFP as a negative control. According to our method of FRET calculation, a negative control should exhibit a FRET measurement of 1.0 (See Materials and Methods). The strain containing YFP-Ndc80/Nuf2-CFP exhibited a FRET value of 1.02 ± 0.14. In summary, these four strains confirmed that this FRET-based approach is a viable way to determine kinetochore architecture (Fig. 4.2).

Precise background subtraction and measurements of signal intensity are required for accurate FRET measurements

When fluorescently-tagged, kinetochores are both larger and more diffuse (because they are not diffraction-limited spots) than spindle pole bodies under the same conditions. For this reason, we tested if image acquisition binning (when adjacent pixels are combined) and/or the pixel size of the region of interest (ROI) during analysis might be different than those settings used during the study of *in vivo* FRET of spindle pole bodies (2x2 binned images with a 5x5 ROI) (Muller et al., 2005). Improper parameters could lead to inaccurate measurements of both background subtraction and fluorescence signal intensity (and consequently FRET measurements) for these kinetochore studies. Thus, we took one negative and one positive control at the Ndc80 complex

(Y-Ndc80 Nuf2-C; Y-Ndc80 C-Nuf2) and re-imaged the strains using either unbinned or 2x2 binned, and then reanalyzed each of those data sets using either a 5x5 pixel box or a 7x7 pixel box to find ROIs (i.e. the kinetochores) (Fig. 4.3). Using our FRET calculation, a negative FRET control should have a FRET value of 1.0, whereas a positive control should exhibit FRET of at least 1.1. The binned 5x5 ROI condition leads to the most accurate measurement of FRET for the negative control (closest to a value of 1.0) (1.02 ± 0.14 vs. 0.92 ± 0.11, 1.16 ± 0.25 or 1.17 ± 0.34); the positive control also exhibits energy transfer above 1.1 using these parameters (1.26 ± 0.20) (Fig. 4.3). For all following FRET strain imaging and analysis, 2x2 image binning and a 5x5 pixel ROI during analysis were used.

Most Ndc80 complex/Dam1 complex FRET pair locations do not exhibit energy transfer during anaphase

We then tested the remaining eight strains for FRET, probing Ndc80 intra-complex, Dam1 intra-complex and Ndc80-Dam1 inter-complex interactions. Only two experimental strains showed reproducible, low-level FRET values (Spc34-YFP/Nuf2-CFP and Spc34-YFP/Dad4-CFP; 1.14 ± 0.14 and 1.11 ±0.12, respectively) (Fig. 4.2). Though these experiments were performed on an asynchronous population of cells, analysis resulted in data sets disproportionately comprised of anaphase cells (in some data sets, up to 15-fold more cells in anaphase than metaphase). This may be due to the fact that fluorescently-labeled kinetochores during anaphase result in less diffuse and essentially “more focused” puncta as compared to when kinetochores are aligned at the metaphase plate, for example. During FRET analysis, only those kinetochores most in focus are retained, leading to artificial enrichment of anaphase represented in the data set.

4.4 DISCUSSION

Previous use of this FRET-based approach probed the architecture of the spindle pole body, the budding yeast equivalent of the centrosome (Muller et al., 2005). Here, we used this technique to probe interactions between the Ndc80 complex and Dam1 complex at the budding yeast kinetochore. We were able to faithfully report *in vivo* FRET values for interactions at the budding yeast kinetochore, as assessed by negative and positive controls constructed within the Ndc80 complex. However, out of seven strains constructed to probe Dam1 intra-complex interactions and Ndc80-Dam1 inter-complex interactions, only two (Spc34-Y Nuf2-C and Spc34-Y Dad4-C) showed any appreciable FRET. In addition, these FRET values were subtle, barely above a value of 1.1. FRET between the C-termini of Nuf2 (Ndc80 complex) and Spc34 (Dam1 complex) indicate it is likely that at least in anaphase, one Dam1 complex ring occupies the site of interaction on the Ndc80 protein between its loop region and C terminus. It is unclear if the FRET that occurs between the C-termini of Spc34 and Dad4 represents an inter- or intra-Dam1 complex interaction. According to a recently published structure of the Dam1 complex, Spc34 and Spc19 extend to form a protrusion from the Dam1 complex body (Jenni & Harrison, 2018). As this protrusion is presumably flexible and conceivably could be in close proximity with either Dad4 on the same or a different Dam1 complex ring, this structure does not rule out either an inter- or intra- complex interaction.

Methods of calculating FRET rely on accurate background correction of in-focus puncta with high fluorescence signal. Background correction and fluorescence signal are influenced by changing parameters such as binning pixels to increase the signal to background ratio or the method of background subtraction. We found that unbinned images lead to an artificial enhancement of FRET in both the negative and positive control strains, and using a 7x7 ROI lead

to an artificial reduction of FRET in both the negative and positive control strains. Presumably, unbinned images are plagued by low signal to background, whereas using an inappropriate ROI makes correct background subtraction more challenging. Comparisons between data sets varying these parameters underscore the sensitivity of FRET calculations to accurate background subtractions and fluorescence signal and the necessity of control strains.

What could be the reasons for the lack of FRET within the Dam1 complex or between the Dam1 complex and the Ndc80 complex? The easiest explanation is that we did not probe enough different combinations or probed the wrong combinations of tagged proteins. For example, though we tagged 4 different proteins of the Dam1 complex at 5 unique sites, the Dam1 complex is a heterodecamer, and thus 6 proteins went unexplored. It is also possible that we limited our search space by using only the N-terminus and C-terminus of each protein to tag with fluorophores, and that internal tagging might lead to different FRET measurements of the same proteins. We initially used the model of the Dam1 complex on the microtubule lattice published from our lab to choose the proteins that would most likely lead to FRET, and it might seem surprising that so many of those strains did not exhibit FRET (Zelter et al., 2015). Yet, the newest structure of the Dam1 complex highlights that multiple proteins in the complex contain highly flexible and disordered regions (particularly Dam1, Ask1 and Duo1) and may not be in as close proximity as originally expected.

Another possibility is that these complexes at the kinetochore are highly dynamic. Recent evidence suggests that the Ndc80 complex can undergo massive structural rearrangements *in vitro*; if these conformational changes also occur *in vivo,* especially in a cell cycle-dependent manner, then it is reasonable to assume that these changes could affect FRET measurements. It is not absurd to speculate that perhaps alone or in concert with other kinetochore complexes, the

Dam1 complex also exhibits conformational changes during mitosis. Due to our method of data analysis, we essentially only examined the FRET values of cells in anaphase. It may be worthwhile to biochemically synchronize the cells in order to equally sample different stages of mitosis, such as metaphase.

In summary, *in vivo* FRET can be used to probe interactions within and between protein complexes at the budding yeast kinetochore. This was validated by the measurement of FRET for multiple control strains within the Ndc80 complex. Yet, positive FRET values proved to be elusive for the remainder of the experimental strains probing the Dam1 complex and Ndc80 complex, with the exception of two strains (Spc34-Y Nuf2-C and Spc34-Y Dad4-C) displaying low FRET values. This resulted in the inability to support or reject our original hypotheses. This project could be potentially improved with experimental techniques to synchronize the cells (i.e. bin certain cell cycle stages manually or use a chemical like α-factor). It is also very likely that more strains simply need to be constructed with different locations of fluorophores for a more thorough characterization of Ndc80-Dam1 complex interactions.

4.5 ACKNOWLEDGMENTS

Eric Muller helped immensely with the experimental and technical aspects of this project, and his previous work formed an important basis that guided this work (Muller et al., 2005). King Yabut and Kim Fong answered my numerous questions about yeast strain construction and yeast genetics.

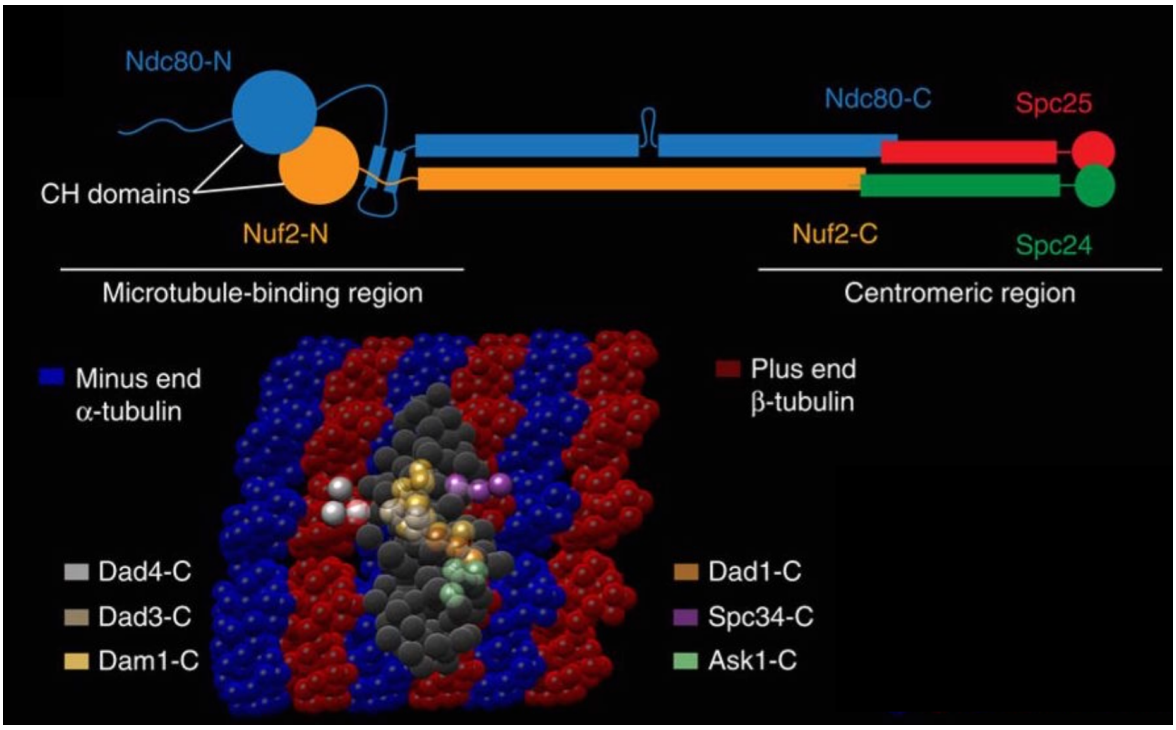

Figure 4.1. Cross-linked based flexible docking of the Dam1 complex model on the microtubules specifies a preferred orientation.
The orientation of the Dam1 complex on the MT with respect to the orientation of the Ndc80 complex. The C-terminal MT-binding region of the Ndc80 complex is nearer the minus end of the MT. (Aravamudhan et al., 2014) measured FRET between N-Nuf2 and six Dam1 complex C termini. The proteins in the key to the left and right of the model represent these results, which indicates proximity between the C termini of Dam1p, Dad4p and Dad3p to the N terminus of Nuf2, while suggesting that the C termini of Spc34p, Ask1p and Dad1p are further away. Only a Dam1 complex monomer is shown for clarity. Adapted from (Zelter et al., 2015).

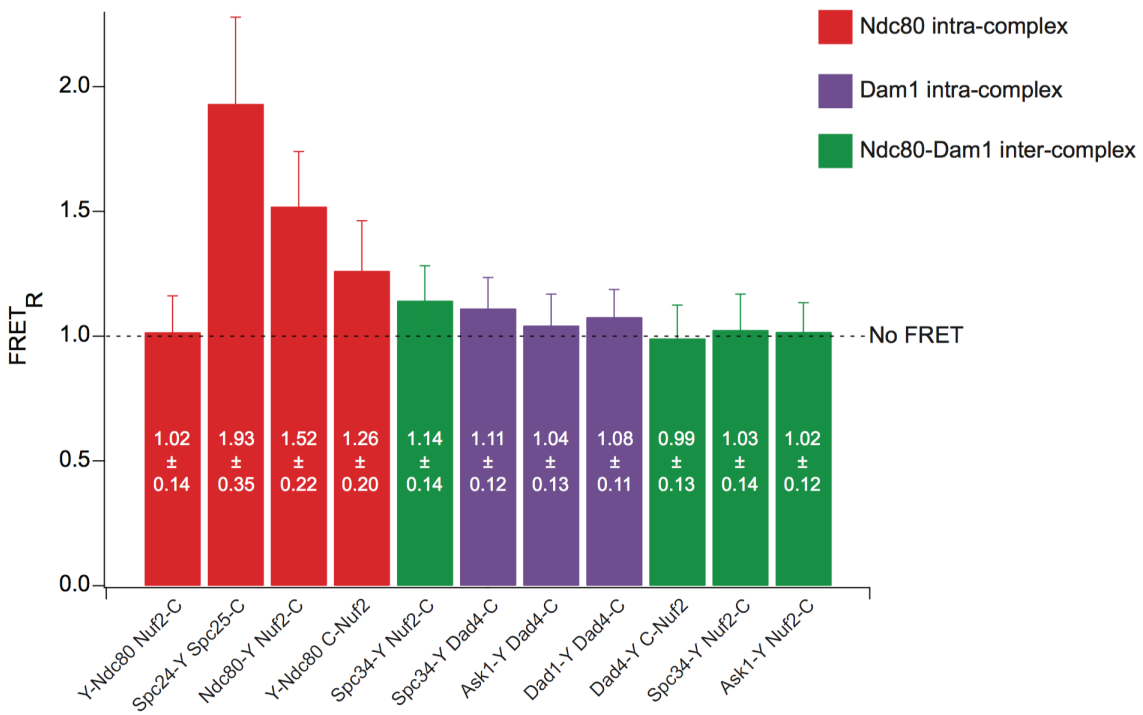

Figure 4.2. *In vivo* FRET values of the Ndc80 and Dam1 complex, and between the Ndc80 and Dam1 complex.

Calculated FRET values of 11 strains probing Ndc80 and Dam1 complex intra-complex interactions (red and purple bars, respectively) and Ndc80-Dam1 complex inter-complex interactions (green bars). Each strain was imaged at least 2 days, with an n value of at least 174. Images were acquired with 2x2 binning and analyzed with a 5x5 pixel ROI.

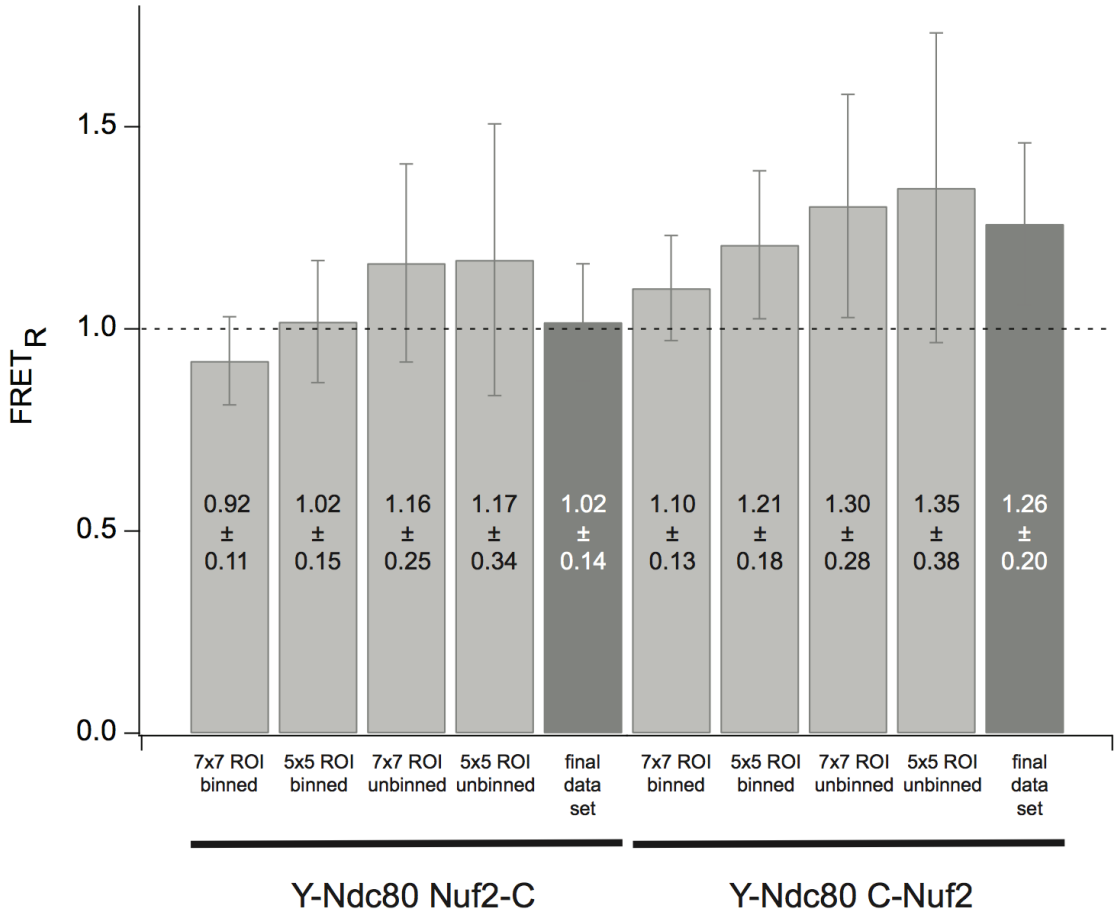

Figure 4.3. High fluorescence signal intensity and precise background subtraction are required for accurate FRET measurements.
Calculated FRET values of a negative control (YFP-Ndc80 Nuf2-C) and a positive control (Y-Ndc80 C-Nuf2) constructed within the Ndc80 complex. Gray bars for each strain (negative control, left half; positive control, right half) indicate different imaging and analysis conditions for one day of imaging (n values for each condition range from 54-131). Dark gray bars indicate complete multi-day data sets (repeated from Fig. 4.3) for each strain, analyzed using 2x2 binned imaging with a 5x5 ROI.

Table 4.1. *In vivo* FRET yeast strains used in this study.

Strain	Genotype	Reference
ESY1	*MATα ade2-1oc ade3-Δ100 can1-100 his3-11,15 leu2-3,112 trp1-1 ura3-1 YFP-NDC80::kanMX*	This study
ESY9	*ade2-1oc ade3-Δ100 can1-100 his3-11,15 leu2-3,112 trp1-1 ura3-1 ASK1-YFP::HIS3 NUF2-CFP::hphMX SPC42-mCherry::hphMX*	This study
ESY18	*MATa ade2-1oc ade3 Δ100 can1-100 his3-11,15 leu2-3,112 trp1-1 ura3-1 SPC34-YFP::HIS3 NUF2-CFP::hphMX SPC42-mCherry::hphMX*	This study
ESY19	*MATα ade2-1oc ade3-Δ100 can1-100 his3-11,15 leu2-3,112 trp1-1 ura3-1 DAD4-CFP::hphMX SPC34-YFP::HIS3 SPC42-mCherry::hphMX*	This study
ESY20	*ade2-1oc ade3-Δ100 can1-100 his3-11,15 leu2-3,112 trp1-1 ura3-1 SPC34-YFP::HIS3 CFP-NUF2::kanMX SPC42-mCherry::hphMX*	This study
ESY23	*MATa ade2-1oc ade3-Δ100 can1-100 his3-11,15 leu2-3,112 trp1-1 ura3-1 DAD4-YFP::HIS3 CFP-NUF2::kanMX*	This study
ESY25	*ade2-1oc ade3-Δ100 can1-100 his3-11,15 leu2-3,112 trp1-1 ura3-1 DAD1-YFP::HIS3 NUF2-CFP::hphMX*	This study
ESY27	*ade2-1oc ade3-Δ100 can1-100 his3-11,15 leu2-3,112 trp1-1 ura3-1 NUF2-CFP::hphMX YFP-NDC80::HIS3*	This study
ESY28	*ade2-1oc ade3-Δ100 can1-100 his3-11,15 leu2-3,112 trp1-1 ura3-1 YFP-NDC80::kanMX CFP-NUF2::kanMX*	This study
ESY32	*ade2-1oc ade3-Δ100 can1-100 his3-11,15 leu2-3,112 trp1-1 ura3-1 ASK1-YFP::HIS3 DAD4-CFP::hphMX*	This study
ESY33	*ade2-1oc ade3-Δ100 can1-100 his3-11,15 leu2-3,112 trp1-1 ura3-1 NUF2-CFP::hphMX NDC80-YFP::HIS3*	This study
ESY34	*ade2-1oc ade3-Δ100 can1-100 his3-11,15 leu2-3,112 trp1-1 ura3-1 SPC24-YFP::HIS3 SPC25-CFP::hphMX*	This study
JJY53	*MATα ade2-1oc ade3-Δ100 can1-100 his3-11,15 leu2-3,112 trp1-1 ura3-1 NUF2-CFP::hphMX*	This study

Chapter 5. CONCLUSIONS AND FUTURE DIRECTIONS

5.1 CONFORMATIONAL CHANGES OF THE NDC80 COMPLEX WITHIN THE KINETOCHORE

We examined the functional significance of conformational changes of the Ndc80 complex. We showed that the Ndc80 complex dynamically fluctuates around its loop region, adopting open and closed conformations, both in solution and when specifically tethered to a coverslip. The tightly bent conformation brings both ends of the complex into close proximity. However, it is still unknown if this specific conformation is compatible within the context of the whole kinetochore, or if the Ndc80 complex can only explore this tightly bent structure prior to assembly at the kinetochore. Labs have succeeded in purifying whole kinetochore particles from yeast (Akiyoshi et al., 2010; Gupta, Evans, Koch, Littleton, & Biggins, 2018). Though this allows for the fluorescent labeling of specific components within the kinetochore, standard labeling and purification methods are traditionally limited by protein fluorophores, such as GFP or mCherry, which generally have inferior photophysical characteristics, such as fast photobleaching, relative to organic fluorophores (though SNAP and CLIP methods of fluorescently labeling proteins allow for the use of superior fluorophores, they are still quite bulky). Purified recombinant Ndc80 complexes specifically labeled with organic fluorophores at multiple sites within the complex (such as Cy3 and Alexa Fluor 647 as used in other chapters) could be "added back" to purified kinetochores. Then, in this context of the entirety of the budding yeast kinetochore, one could measure conformational changes of the Ndc80 complex during precise application of force. Moreover, under these conditions, one can make specific mutations or post-translational modifications mimics within the added-back purified Ndc80 complex that are precisely known, which is not always easily ascertained with proteins *in vivo*.

The kinetochore is assembled such that inner-most kinetochore components are assembled first, and then outer components are built upon them in a step-wise fashion according to their spatial arrangement (Musacchio & Desai, 2017). However, this assembly is not a simple linear chain. There are multiple pathways of assembly and multiple receptors for the Ndc80 complex (Lang et al., 2018; Malvezzi et al., 2013). In yeast, the Ndc80 complex can bind to Cnn1 (CENP-T) instead of MIND, though unlike MIND, Cnn1 is non-essential (Malvezzi et al., 2013). It is unknown if Cnn1 has the capacity to allosterically regulate the Ndc80 complex. Current data suggest that these different pathways of Ndc80 assembly are phospho-regulated in such a way that the same kinase promotes the association of the Ndc80 complex to one receptor as it weakens the interaction with the other, implying the potential of a "hand-off" from one to the other (Hara, Ariyoshi, Okumura, Hori, & Fukagawa, 2018). To further speculate, if MIND and Cnn1 affect the conformation of the Ndc80 complex dissimilarly, this "hand-off" could represent coordination between mitotic progression and structural changes of the Ndc80 complex. If so, it will be interesting to investigate why the kinetochore might use different receptors, at distinct times, which regulate the Ndc80 complex conformations in unique ways.

Overall, next steps should focus on understanding the *in vivo* importance of Ndc80 auto-inhibition and establishing how this intrinsic regulation of conformational changes is integrated with extrinsic Ndc80 regulation in the cell: how do these methods of regulation work in concert? Are any of these mechanisms redundant? Are some mechanisms of regulation only important during specific cellular contexts? Combining *in vitro* assays with the advantages of budding yeast may be effective first steps to begin to answer these questions.

5.2 CONFORMATIONAL CHANGES OF KINETOCHORE COMPONENTS ON THE MICROTUBULE

We developed the first *in vitro* assay using FRET at the single molecule level to measure conformational changes and intra-complex interactions of a kinetochore component. We found that the Ndc80 complex can undergo dynamic fluctuations between open and closed conformations when specifically bound to a coverslip. We extended these measurements to microtubule-bound Ndc80 complexes, showing that microtubule binding selects for the open conformation of Ndc80. However, these experiments were limited for technical reasons in that only the FRET of non-diffusing Ndc80 complexes residing on the microtubule for long period of times could be measured. In the future, it would be valuable to repeat these experiments on diffusing, short-lived Ndc80 complexes (which are generally the majority species in TIRF microscopy microtubule binding assays). Perhaps under these conditions, it would be possible to see the occurrence of FRET (indicating a tightly bent conformation, which according to our model, is incompatible with stable microtubule binding) immediately prior to dissociation from the microtubule surface. Furthermore, this assay could be expanded to other kinetochore components (such as the Dam1 complex) and to inter-complex interactions of kinetochore components (such as using FRET to probe Ndc80-Dam1 complex interactions on the microtubule surface). To do this, optimization of both the oxygen-scavenging system (to be able to image under short wavelength excitation, the "FRET channel," for longer periods of time) and Labview software (to be able to measure the fluorescence intensity of diffusing particles) will be required.

5.3 EXTENDING THESE STUDIES TO KINETOCHORES OF OTHER SPECIES

The Ndc80 complex is highly conserved, both functionally and structurally, from yeast to humans. It is unknown if Ndc80 auto-inhibition is a conserved mechanism of regulation. Due to a high degree of structural similarity between the yeast and human Ndc80 complexes, it seems most likely that the human Ndc80 complex is also able to tightly bend around its loop region. Moreover, data suggest that the *C. elegans* version of Ndc80 may be auto-inhibited (Cheeseman et al., 2006). More direct measurements, most likely using single molecule techniques, must be performed on these Ndc80 complexes of different species to more fully elucidate mechanistic details.

5.4 THE KINETOCHORE AS A TENSION SENSOR

When sister chromatids are properly bioriented between two spindles, this creates tension across the spindle, kinetochores and DNA. It is thought that this tension is a signal to the cell that the chromosomes are properly congressed and ready for anaphase. But how precisely does tension translate into a chemical signal for the cell? The Ndc80 complex is an attractive target for the mitotic tension-sensor due to its central role in chromosome segregation and its flexibility: coiled coils (of which the Ndc80 complex is primarily composed of) can be modeled as springs (which presumably would be responsive to force and tension) and its loop region defines a joint around which the complex can bend. Direct *in vivo* measurements of tension across the kinetochore or other components of the mitotic spindle are complicated by the many contributors to force generation as well as the number of potential pathways of force transduction within the cell. Moreover, even if one can precisely control tension and force within a living cell, it is technically difficult to achieve the resolution needed to track the conformational changes of one protein or

complex over time in such an environment, and thus, many unanswered questions remain: does the Ndc80 complex change conformations when force is applied? Does the Ndc80 complex change conformation when force is applied with the addition of other kinetochore components (such as those that comprise a minimal pathway of force within the budding yeast kinetochore)? Instruments such as optical trap can apply very small (biologically-relevant) amounts of force on a variety of substrates, from single proteins to whole cells, *in vitro* in a precisely controlled and quantified manner. By pairing Ndc80 complexes end-labeled with a FRET pair and optical trap, it may be possible to address these basic questions of tension in a highly rigorous manner.

BIBLIOGRAPHY

Akiyoshi, B., Nelson, C. R., & Biggins, S. (2013). The aurora B kinase promotes inner and outer kinetochore interactions in budding yeast. *Genetics, 194*(3), 785-789. doi:10.1534/genetics.113.150839

Akiyoshi, B., Nelson, C. R., Ranish, J. A., & Biggins, S. (2009). Analysis of Ipl1-mediated phosphorylation of the Ndc80 kinetochore protein in Saccharomyces cerevisiae. *Genetics, 183*(4), 1591-1595. doi:10.1534/genetics.109.109041

Akiyoshi, B., Sarangapani, K. K., Powers, A. F., Nelson, C. R., Reichow, S. L., Arellano-Santoyo, H., . . . Biggins, S. (2010). Tension directly stabilizes reconstituted kinetochore-microtubule attachments. *Nature, 468*(7323), 576-579. doi:10.1038/nature09594

Alushin, G. M., Musinipally, V., Matson, D., Tooley, J., Stukenberg, P. T., & Nogales, E. (2012). Multimodal microtubule binding by the Ndc80 kinetochore complex. *Nat Struct Mol Biol, 19*(11), 1161-1167. doi:10.1038/nsmb.2411

Alushin, G. M., Ramey, V. H., Pasqualato, S., Ball, D. A., Grigorieff, N., Musacchio, A., & Nogales, E. (2010). The Ndc80 kinetochore complex forms oligomeric arrays along microtubules. *Nature, 467*(7317), 805-810. doi:10.1038/nature09423

AMBROSE, E. J. (1956). A surface contact microscope for the study of cell movements. *Nature, 178*(4543), 1194.

Aravamudhan, P., Felzer-Kim, I., Gurunathan, K., & Joglekar, A. P. (2014). Assembling the protein architecture of the budding yeast kinetochore-microtubule attachment using FRET. *Curr Biol, 24*(13), 1437-1446. doi:10.1016/j.cub.2014.05.014

Aravamudhan, P., Goldfarb, A. A., & Joglekar, A. P. (2015). The kinetochore encodes a mechanical switch to disrupt spindle assembly checkpoint signalling. *Nat Cell Biol, 17*(7), 868-879. doi:10.1038/ncb3179

Ashkin, A. (1970). Acceleration and trapping of particles by radiation pressure. In (Vol. 24, pp. 156-159): Phys Rev Lett.

Biggins, S. (2013). The composition, functions, and regulation of the budding yeast kinetochore. *Genetics, 194*(4), 817-846. doi:10.1534/genetics.112.145276

Biggins, S., & Murray, A. W. (2001). The budding yeast protein kinase Ipl1/Aurora allows the absence of tension to activate the spindle checkpoint. *Genes Dev, 15*(23), 3118-3129. doi:10.1101/gad.934801

Block, S. M., Goldstein, L. S., & Schnapp, B. J. (1990). Bead movement by single kinesin molecules studied with optical tweezers. *Nature, 348*(6299), 348-352. doi:10.1038/348348a0

Bock, L. J., Pagliuca, C., Kobayashi, N., Grove, R. A., Oku, Y., Shrestha, K., . . . De Wulf, P. (2012). Cnn1 inhibits the interactions between the KMN complexes of the yeast kinetochore. *Nat Cell Biol, 14*(6), 614-624. doi:10.1038/ncb2495

Boveri, T. (1902). Ueber mehrpolige Mitosen als Mittel zur Analyse des Zellkerns. In (Vol. 35, pp. 67-90): Verh Phys-med Ges Würzburg NF.

Brown, M. L., Lipscomb, J., & Snyder, C. (2001). The burden of illness of cancer: economic cost and quality of life. *Annu Rev Public Health, 22*, 91-113. doi:10.1146/annurev.publhealth.22.1.91

Bütschli, O. (1876). Studien über die ersten Entwicklungsvorgänge der Eizelle, die

Zelltheilung und die Conjugation der Infusorien. In *Abhandlungen der Senckenbergischen Naturforschenden Gesellschaft Frankfurt am Main* (Vol. 10, pp. 1-250).
Camahort, R., Li, B., Florens, L., Swanson, S. K., Washburn, M. P., & Gerton, J. L. (2007). Scm3 is essential to recruit the histone h3 variant cse4 to centromeres and to maintain a functional kinetochore. *Mol Cell, 26*(6), 853-865. doi:10.1016/j.molcel.2007.05.013
Carter, A. P., Garbarino, J. E., Wilson-Kubalek, E. M., Shipley, W. E., Cho, C., Milligan, R. A., . . . Gibbons, I. R. (2008). Structure and functional role of dynein's microtubule-binding domain. *Science, 322*(5908), 1691-1695. doi:10.1126/science.1164424
Chacón, J. M., Mukherjee, S., Schuster, B. M., Clarke, D. J., & Gardner, M. K. (2014). Pericentromere tension is self-regulated by spindle structure in metaphase. *J Cell Biol, 205*(3), 313-324. doi:10.1083/jcb.201312024
Cheeseman, I. M. (2014). The kinetochore. *Cold Spring Harb Perspect Biol, 6*(7), a015826. doi:10.1101/cshperspect.a015826
Cheeseman, I. M., Chappie, J. S., Wilson-Kubalek, E. M., & Desai, A. (2006). The conserved KMN network constitutes the core microtubule-binding site of the kinetochore. *Cell, 127*(5), 983-997. doi:10.1016/j.cell.2006.09.039
Cheeseman, I. M., & Desai, A. (2008). Molecular architecture of the kinetochore-microtubule interface. *Nat Rev Mol Cell Biol, 9*(1), 33-46. doi:10.1038/nrm2310
Chrétien, D., Fuller, S. D., & Karsenti, E. (1995). Structure of growing microtubule ends: two-dimensional sheets close into tubes at variable rates. *J Cell Biol, 129*(5), 1311-1328.
Ciferri, C., De Luca, J., Monzani, S., Ferrari, K. J., Ristic, D., Wyman, C., . . . Musacchio, A. (2005). Architecture of the human ndc80-hec1 complex, a critical constituent of the outer kinetochore. *J Biol Chem, 280*(32), 29088-29095. doi:10.1074/jbc.M504070200
Ciferri, C., Musacchio, A., & Petrovic, A. (2007). The Ndc80 complex: hub of kinetochore activity. *FEBS Lett, 581*(15), 2862-2869. doi:10.1016/j.febslet.2007.05.012
Ciferri, C., Pasqualato, S., Screpanti, E., Varetti, G., Santaguida, S., Dos Reis, G., . . . Musacchio, A. (2008). Implications for kinetochore-microtubule attachment from the structure of an engineered Ndc80 complex. *Cell, 133*(3), 427-439. doi:10.1016/j.cell.2008.03.020
Coy, D. L., Hancock, W. O., Wagenbach, M., & Howard, J. (1999). Kinesin's tail domain is an inhibitory regulator of the motor domain. *Nat Cell Biol, 1*(5), 288-292. doi:10.1038/13001
Deng, Y., & Asbury, C. L. (2017). Simultaneous Manipulation and Super-Resolution Fluorescence Imaging of Individual Kinetochores Coupled to Microtubule Tips. *Methods Mol Biol, 1486*, 437-467. doi:10.1007/978-1-4939-6421-5_17
Diaz-Rodríguez, E., Sotillo, R., Schvartzman, J. M., & Benezra, R. (2008). Hec1 overexpression hyperactivates the mitotic checkpoint and induces tumor formation in vivo. *Proc Natl Acad Sci U S A, 105*(43), 16719-16724. doi:10.1073/pnas.0803504105
Dimitrova, Y. N., Jenni, S., Valverde, R., Khin, Y., & Harrison, S. C. (2016a). Structure of the MIND Complex Defines a Regulatory Focus for Yeast Kinetochore Assembly. *Cell, 167*(4), 1014-1027 e1012. doi:10.1016/j.cell.2016.10.011
Dimitrova, Y. N., Jenni, S., Valverde, R., Khin, Y., & Harrison, S. C. (2016b). Structure of the MIND Complex Defines a Regulatory Focus for Yeast Kinetochore Assembly. *Cell, 167*(4), 1014-1027.e1012. doi:10.1016/j.cell.2016.10.011
Donovan, K. W., & Bretscher, A. (2015). Head-to-tail regulation is critical for the in vivo function of myosin V. *J Cell Biol, 209*(3), 359-365. doi:10.1083/jcb.201411010

Doxsey, S. (2001). Re-evaluating centrosome function. *Nat Rev Mol Cell Biol, 2*(9), 688-698. doi:10.1038/35089575

Duncan, A. W., Hanlon Newell, A. E., Bi, W., Finegold, M. J., Olson, S. B., Beaudet, A. L., & Grompe, M. (2012). Aneuploidy as a mechanism for stress-induced liver adaptation. *J Clin Invest, 122*(9), 3307-3315. doi:10.1172/JCI64026

Erickson, H. P. (2009). Size and shape of protein molecules at the nanometer level determined by sedimentation, gel filtration, and electron microscopy. *Biol Proced Online, 11*, 32-51. doi:10.1007/s12575-009-9008-x

Etemad, B., Kuijt, T. E., & Kops, G. J. (2015). Kinetochore-microtubule attachment is sufficient to satisfy the human spindle assembly checkpoint. *Nat Commun, 6*, 8987. doi:10.1038/ncomms9987

Flemming, W. (1882). *Zellsubstanz, Kern und Zelltheilung*. Leipzig,: Vogel.

Franck, A. D., Powers, A. F., Gestaut, D. R., Davis, T. N., & Asbury, C. L. (2010). Direct physical study of kinetochore-microtubule interactions by reconstitution and interrogation with an optical force clamp. *Methods, 51*(2), 242-250. doi:10.1016/j.ymeth.2010.01.020

Friedman, D. S., & Vale, R. D. (1999). Single-molecule analysis of kinesin motility reveals regulation by the cargo-binding tail domain. *Nat Cell Biol, 1*(5), 293-297. doi:10.1038/13008

Friedman, L. J., Chung, J., & Gelles, J. (2006). Viewing dynamic assembly of molecular complexes by multi-wavelength single-molecule fluorescence. *Biophys J, 91*(3), 1023-1031. doi:10.1529/biophysj.106.084004

Furuyama, S., & Biggins, S. (2007). Centromere identity is specified by a single centromeric nucleosome in budding yeast. *Proc Natl Acad Sci U S A, 104*(37), 14706-14711. doi:10.1073/pnas.0706985104

Gestaut, D. R., Cooper, J., Asbury, C. L., Davis, T. N., & Wordeman, L. (2010). Reconstitution and functional analysis of kinetochore subcomplexes. *Methods Cell Biol, 95*, 641-656. doi:10.1016/S0091-679X(10)95032-2

Gireesh, K. K., Shine, A., Lakshmi, R. B., Vijayan, V., & Manna, T. K. (2018). GTP-binding facilitates EB1 recruitment onto microtubules by relieving its auto-inhibition. *Sci Rep, 8*(1), 9792. doi:10.1038/s41598-018-28056-y

Gräf, R. (2018). Comparative Biology of Centrosomal Structures in Eukaryotes. *Cells, 7*(11). doi:10.3390/cells7110202

Gupta, A., Evans, R. K., Koch, L. B., Littleton, A. J., & Biggins, S. (2018). Purification of kinetochores from the budding yeast Saccharomyces cerevisiae. *Methods Cell Biol, 144*, 349-370. doi:10.1016/bs.mcb.2018.03.023

Hailey, D. W., Davis, T. N., & Muller, E. G. (2002). Fluorescence resonance energy transfer using color variants of green fluorescent protein. *Methods Enzymol, 351*, 34-49.

Hanahan, D., & Weinberg, R. A. (2011). Hallmarks of cancer: the next generation. *Cell, 144*(5), 646-674. doi:10.1016/j.cell.2011.02.013

Hanks, S., Coleman, K., Reid, S., Plaja, A., Firth, H., Fitzpatrick, D., . . . Rahman, N. (2004). Constitutional aneuploidy and cancer predisposition caused by biallelic mutations in BUB1B. *Nat Genet, 36*(11), 1159-1161. doi:10.1038/ng1449

Hara, M., Ariyoshi, M., Okumura, E. I., Hori, T., & Fukagawa, T. (2018). Publisher Correction: Multiple phosphorylations control recruitment of the KMN network onto kinetochores. *Nat Cell Biol, 20*(12), 1434. doi:10.1038/s41556-018-0252-7

He, X., Rines, D. R., Espelin, C. W., & Sorger, P. K. (2001). Molecular analysis of kinetochore-microtubule attachment in budding yeast. *Cell, 106*(2), 195-206.

Hooke, R. (1665). *Micrographia, or, Some physiological descriptions of minute bodies made by magnifying glasses*

with observations and inquiries thereupon. London: Printed by J. Martyn and J. Allestry.

Hornung, P., Maier, M., Alushin, G. M., Lander, G. C., Nogales, E., & Westermann, S. (2011). Molecular architecture and connectivity of the budding yeast Mtw1 kinetochore complex. *J Mol Biol, 405*(2), 548-559. doi:10.1016/j.jmb.2010.11.012

Hung, C. Y., Volkmar, B., Baker, J. D., Bauer, J. W., Gussoni, E., Hainzl, S., . . . Bodamer, O. A. (2017). A defect in the inner kinetochore protein CENPT causes a new syndrome of severe growth failure. *PLoS One, 12*(12), e0189324. doi:10.1371/journal.pone.0189324

Janke, C., Ortíz, J., Tanaka, T. U., Lechner, J., & Schiebel, E. (2002). Four new subunits of the Dam1-Duo1 complex reveal novel functions in sister kinetochore biorientation. *EMBO J, 21*(1-2), 181-193. doi:10.1093/emboj/21.1.181

Jenni, S., & Harrison, S. C. (2018). Structure of the DASH/Dam1 complex shows its role at the yeast kinetochore-microtubule interface. *Science, 360*(6388), 552-558. doi:10.1126/science.aar6436

Joglekar, A. P., Bloom, K., & Salmon, E. D. (2009). In vivo protein architecture of the eukaryotic kinetochore with nanometer scale accuracy. *Curr Biol, 19*(8), 694-699. doi:10.1016/j.cub.2009.02.056

Joglekar, A. P., Bouck, D. C., Molk, J. N., Bloom, K. S., & Salmon, E. D. (2006). Molecular architecture of a kinetochore-microtubule attachment site. *Nat Cell Biol, 8*(6), 581-585. doi:10.1038/ncb1414

Johnston, K., Joglekar, A., Hori, T., Suzuki, A., Fukagawa, T., & Salmon, E. D. (2010). Vertebrate kinetochore protein architecture: protein copy number. *J Cell Biol, 189*(6), 937-943. doi:10.1083/jcb.200912022

Joo, C., & Ha, T. (2012). Labeling Proteins for Single-Molecule FRET. In. Cold Spring Harbor, NY, USA: Cold Spring Harbor Laboratory Press.

Kaan, H. Y., Hackney, D. D., & Kozielski, F. (2011). The structure of the kinesin-1 motor-tail complex reveals the mechanism of autoinhibition. *Science, 333*(6044), 883-885. doi:10.1126/science.1204824

Kellermayer, M. S., Smith, S. B., Granzier, H. L., & Bustamante, C. (1997). Folding-unfolding transitions in single titin molecules characterized with laser tweezers. *Science, 276*(5315), 1112-1116.

Kim, J. O., Zelter, A., Umbreit, N. T., Bollozos, A., Riffle, M., Johnson, R., . . . Davis, T. N. (2017). The Ndc80 complex bridges two Dam1 complex rings. *Elife, 6*. doi:10.7554/eLife.21069

Kingsbury, M. A., Yung, Y. C., Peterson, S. E., Westra, J. W., & Chun, J. (2006). Aneuploidy in the normal and diseased brain. *Cell Mol Life Sci, 63*(22), 2626-2641. doi:10.1007/s00018-006-6169-5

Knouse, K. A., Wu, J., Whittaker, C. A., & Amon, A. (2014). Single cell sequencing reveals low levels of aneuploidy across mammalian tissues. *Proc Natl Acad Sci U S A, 111*(37), 13409-13414. doi:10.1073/pnas.1415287111

Kollman, J. M., Zelter, A., Muller, E. G., Fox, B., Rice, L. M., Davis, T. N., & Agard, D. A. (2008). The structure of the gamma-tubulin small complex: implications of its

architecture and flexibility for microtubule nucleation. *Mol Biol Cell, 19*(1), 207-215. doi:10.1091/mbc.e07-09-0879
Kremers, G. J., Gilbert, S. G., Cranfill, P. J., Davidson, M. W., & Piston, D. W. (2011). Fluorescent proteins at a glance. *J Cell Sci, 124*(Pt 2), 157-160. doi:10.1242/jcs.072744
Kudalkar, E. M., Scarborough, E. A., Umbreit, N. T., Zelter, A., Gestaut, D. R., Riffle, M., . . . Davis, T. N. (2015). Regulation of outer kinetochore Ndc80 complex-based microtubule attachments by the central kinetochore Mis12/MIND complex. *Proc Natl Acad Sci U S A, 112*(41), E5583-5589. doi:10.1073/pnas.1513882112
Lampert, F., Mieck, C., Alushin, G. M., Nogales, E., & Westermann, S. (2013). Molecular requirements for the formation of a kinetochore-microtubule interface by Dam1 and Ndc80 complexes. *J Cell Biol, 200*(1), 21-30. doi:10.1083/jcb.201210091
Lang, J., Barber, A., & Biggins, S. (2018). An assay for de novo kinetochore assembly reveals a key role for the CENP-T pathway in budding yeast. *Elife, 7*. doi:10.7554/eLife.37819
Levine, M. S., & Holland, A. J. (2018). The impact of mitotic errors on cell proliferation and tumorigenesis. *Genes Dev, 32*(9-10), 620-638. doi:10.1101/gad.314351.118
Longtine, M. S., McKenzie, A., Demarini, D. J., Shah, N. G., Wach, A., Brachat, A., . . . Pringle, J. R. (1998). Additional modules for versatile and economical PCR-based gene deletion and modification in Saccharomyces cerevisiae. *Yeast, 14*(10), 953-961. doi:10.1002/(SICI)1097-0061(199807)14:10<953::AID-YEA293>3.0.CO;2-U
Malvezzi, F., Litos, G., Schleiffer, A., Heuck, A., Mechtler, K., Clausen, T., & Westermann, S. (2013). A structural basis for kinetochore recruitment of the Ndc80 complex via two distinct centromere receptors. *EMBO J, 32*(3), 409-423. doi:10.1038/emboj.2012.356
Mandelkow, E. M., Mandelkow, E., & Milligan, R. A. (1991). Microtubule dynamics and microtubule caps: a time-resolved cryo-electron microscopy study. *J Cell Biol, 114*(5), 977-991.
Margolin, W., & Bernander, R. (2004). How do prokaryotic cells cycle? *Curr Biol, 14*(18), R768-770. doi:10.1016/j.cub.2004.09.017
Martin-Fernandez, M. L., Tynan, C. J., & Webb, S. E. (2013). A 'pocket guide' to total internal reflection fluorescence. *J Microsc, 252*(1), 16-22. doi:10.1111/jmi.12070
Maskell, D. P., Hu, X. W., & Singleton, M. R. (2010). Molecular architecture and assembly of the yeast kinetochore MIND complex. *J Cell Biol, 190*(5), 823-834. doi:10.1083/jcb.201002059
Matsuura, S., Matsumoto, Y., Morishima, K., Izumi, H., Matsumoto, H., Ito, E., . . . Kajii, T. (2006). Monoallelic BUB1B mutations and defective mitotic-spindle checkpoint in seven families with premature chromatid separation (PCS) syndrome. *Am J Med Genet A, 140*(4), 358-367. doi:10.1002/ajmg.a.31069
Maure, J. F., Komoto, S., Oku, Y., Mino, A., Pasqualato, S., Natsume, K., . . . Tanaka, T. U. (2011). The Ndc80 loop region facilitates formation of kinetochore attachment to the dynamic microtubule plus end. *Curr Biol, 21*(3), 207-213. doi:10.1016/j.cub.2010.12.050
Mayzel, W. (1875). Ueber eigenthümliche Vorgänge bei der Theilung der Kerne in
Epithelialzellen. In *Zentralblatt für die Medizinischen Wissenschaften* (pp. 849-850).
McCleland, M. L., Gardner, R. D., Kallio, M. J., Daum, J. R., Gorbsky, G. J., Burke, D. J., & Stukenberg, P. T. (2003). The highly conserved Ndc80 complex is required for kinetochore assembly, chromosome congression, and spindle checkpoint activity. *Genes Dev, 17*(1), 101-114. doi:10.1101/gad.1040903

Mirzaa, G. M., Vitre, B., Carpenter, G., Abramowicz, I., Gleeson, J. G., Paciorkowski, A. R., . . . O'Driscoll, M. (2014). Mutations in CENPE define a novel kinetochore-centromeric mechanism for microcephalic primordial dwarfism. *Hum Genet, 133*(8), 1023-1039. doi:10.1007/s00439-014-1443-3

Mitchison, T., & Kirschner, M. (1984). Dynamic instability of microtubule growth. *Nature, 312*(5991), 237-242.

Muller, E. G., Snydsman, B. E., Novik, I., Hailey, D. W., Gestaut, D. R., Niemann, C. A., . . . Davis, T. N. (2005). The organization of the core proteins of the yeast spindle pole body. *Mol Biol Cell, 16*(7), 3341-3352. doi:10.1091/mbc.E05-03-0214

Musacchio, A., & Desai, A. (2017). A Molecular View of Kinetochore Assembly and Function. *Biology (Basel), 6*(1). doi:10.3390/biology6010005

Nannas, N. J., O'Toole, E. T., Winey, M., & Murray, A. W. (2014). Chromosomal attachments set length and microtubule number in the Saccharomyces cerevisiae mitotic spindle. *Mol Biol Cell, 25*(25), 4034-4048. doi:10.1091/mbc.E14-01-0016

Naylor, R. M., & van Deursen, J. M. (2016). Aneuploidy in Cancer and Aging. *Annu Rev Genet, 50*, 45-66. doi:10.1146/annurev-genet-120215-035303

Neuman, K. C., & Block, S. M. (2004). Optical trapping. *Rev Sci Instrum, 75*(9), 2787-2809. doi:10.1063/1.1785844

Ng, C. T., Deng, L., Chen, C., Lim, H. H., Shi, J., Surana, U., & Gan, L. (2018). Electron cryotomography analysis of Dam1C/DASH at the kinetochore-spindle interface in situ. *J Cell Biol*. doi:10.1083/jcb.201809088

Nishino, T., Rago, F., Hori, T., Tomii, K., Cheeseman, I. M., & Fukagawa, T. (2013). CENP-T provides a structural platform for outer kinetochore assembly. *EMBO J, 32*(3), 424-436. doi:10.1038/emboj.2012.348

Obuse, C., Iwasaki, O., Kiyomitsu, T., Goshima, G., Toyoda, Y., & Yanagida, M. (2004). A conserved Mis12 centromere complex is linked to heterochromatic HP1 and outer kinetochore protein Zwint-1. *Nat Cell Biol, 6*(11), 1135-1141. doi:10.1038/ncb1187

Omer Javed, A., Li, Y., Muffat, J., Su, K. C., Cohen, M. A., Lungjangwa, T., . . . Jaenisch, R. (2018). Microcephaly Modeling of Kinetochore Mutation Reveals a Brain-Specific Phenotype. *Cell Rep, 25*(2), 368-382.e365. doi:10.1016/j.celrep.2018.09.032

Papi, L., Montali, E., Marconi, G., Guazzelli, R., Bigozzi, U., Maraschio, P., & Zuffardi, O. (1989). Evidence for a human mitotic mutant with pleiotropic effect. *Ann Hum Genet, 53*(3), 243-248.

Petrovic, A., Keller, J., Liu, Y., Overlack, K., John, J., Dimitrova, Y. N., . . . Musacchio, A. (2016a). Structure of the MIS12 Complex and Molecular Basis of Its Interaction with CENP-C at Human Kinetochores. *Cell, 167*(4), 1028-1040 e1015. doi:10.1016/j.cell.2016.10.005

Petrovic, A., Keller, J., Liu, Y., Overlack, K., John, J., Dimitrova, Y. N., . . . Musacchio, A. (2016b). Structure of the MIS12 Complex and Molecular Basis of Its Interaction with CENP-C at Human Kinetochores. *Cell, 167*(4), 1028-1040.e1015. doi:10.1016/j.cell.2016.10.005

Petrovic, A., Pasqualato, S., Dube, P., Krenn, V., Santaguida, S., Cittaro, D., . . . Musacchio, A. (2010). The MIS12 complex is a protein interaction hub for outer kinetochore assembly. *J Cell Biol, 190*(5), 835-852. doi:10.1083/jcb.201002070

Polka, J. K., Kollman, J. M., Agard, D. A., & Mullins, R. D. (2009). The structure and assembly dynamics of plasmid actin AlfA imply a novel mechanism of DNA segregation. *J Bacteriol, 191*(20), 6219-6230. doi:10.1128/JB.00676-09

Powers, A. F., Franck, A. D., Gestaut, D. R., Cooper, J., Gracyzk, B., Wei, R. R., . . . Asbury, C. L. (2009). The Ndc80 kinetochore complex forms load-bearing attachments to dynamic microtubule tips via biased diffusion. *Cell, 136*(5), 865-875. doi:10.1016/j.cell.2008.12.045

Prasher, D. C., Eckenrode, V. K., Ward, W. W., Prendergast, F. G., & Cormier, M. J. (1992). Primary structure of the Aequorea victoria green-fluorescent protein. *Gene, 111*(2), 229-233.

Prein, B., Natter, K., & Kohlwein, S. D. (2000). A novel strategy for constructing N-terminal chromosomal fusions to green fluorescent protein in the yeast Saccharomyces cerevisiae. *FEBS Lett, 485*(1), 29-34.

Rago, F., Gascoigne, K. E., & Cheeseman, I. M. (2015). Distinct organization and regulation of the outer kinetochore KMN network downstream of CENP-C and CENP-T. *Curr Biol, 25*(5), 671-677. doi:10.1016/j.cub.2015.01.059

Rehen, S. K., McConnell, M. J., Kaushal, D., Kingsbury, M. A., Yang, A. H., & Chun, J. (2001). Chromosomal variation in neurons of the developing and adult mammalian nervous system. *Proc Natl Acad Sci U S A, 98*(23), 13361-13366. doi:10.1073/pnas.231487398

Renz, M. (2013). Fluorescence microscopy-a historical and technical perspective. *Cytometry A, 83*(9), 767-779. doi:10.1002/cyto.a.22295

Rice, S., Lin, A. W., Safer, D., Hart, C. L., Naber, N., Carragher, B. O., . . . Vale, R. D. (1999). A structural change in the kinesin motor protein that drives motility. *Nature, 402*(6763), 778-784. doi:10.1038/45483

Rieder, C. L. (1982). The formation, structure, and composition of the mammalian kinetochore and kinetochore fiber. *Int Rev Cytol, 79*, 1-58.

Roy, R., Hohng, S., & Ha, T. (2008). A practical guide to single-molecule FRET. *Nat Methods, 5*(6), 507-516. doi:10.1038/nmeth.1208

Saade, M., Blanco-Ameijeiras, J., Gonzalez-Gobartt, E., & Martí, E. (2018). A centrosomal view of CNS growth. *Development, 145*(21). doi:10.1242/dev.170613

Sapp, J. (1998). Freewheeling centrioles. *Hist Philos Life Sci, 20*(3), 255-290.

Sarangapani, K. K., Akiyoshi, B., Duggan, N. M., Biggins, S., & Asbury, C. L. (2013). Phosphoregulation promotes release of kinetochores from dynamic microtubules via multiple mechanisms. *Proc Natl Acad Sci U S A, 110*(18), 7282-7287. doi:10.1073/pnas.1220700110

Schleiffer, A., Maier, M., Litos, G., Lampert, F., Hornung, P., Mechtler, K., & Westermann, S. (2012). CENP-T proteins are conserved centromere receptors of the Ndc80 complex. *Nat Cell Biol, 14*(6), 604-613. doi:10.1038/ncb2493

Schmidt, J. C., Arthanari, H., Boeszoermenyi, A., Dashkevich, N. M., Wilson-Kubalek, E. M., Monnier, N., . . . Cheeseman, I. M. (2012). The kinetochore-bound Ska1 complex tracks depolymerizing microtubules and binds to curved protofilaments. *Dev Cell, 23*(5), 968-980. doi:10.1016/j.devcel.2012.09.012

Schwann, T., & Schleiden, M. J. (1847). *Microscopical researches into the accordance in the structure and growth of animals and plants*. London: The Sydenham Society.

Screpanti, E., De Antoni, A., Alushin, G. M., Petrovic, A., Melis, T., Nogales, E., & Musacchio, A. (2011). Direct binding of Cenp-C to the Mis12 complex joins the inner and outer kinetochore. *Curr Biol, 21*(5), 391-398. doi:10.1016/j.cub.2010.12.039

Selvin, P. R., & Ha, T. *Single-molecule techniques : a laboratory manual*.

Shivaraju, M., Camahort, R., Mattingly, M., & Gerton, J. L. (2011). Scm3 is a centromeric nucleosome assembly factor. *J Biol Chem, 286*(14), 12016-12023. doi:10.1074/jbc.M110.183640

Sun, Y., Wallrabe, H., Seo, S. A., & Periasamy, A. (2011). FRET microscopy in 2010: the legacy of Theodor Förster on the 100th anniversary of his birth. *Chemphyschem, 12*(3), 462-474. doi:10.1002/cphc.201000664

Sundin, B. A., Chiu, C. H., Riffle, M., Davis, T. N., & Muller, E. G. (2004). Localization of proteins that are coordinately expressed with Cln2 during the cell cycle. *Yeast, 21*(9), 793-800. doi:10.1002/yea.1133

Tadir, Y., Wright, W. H., Vafa, O., Ord, T., Asch, R. H., & Berns, M. W. (1989). Micromanipulation of sperm by a laser generated optical trap. *Fertil Steril, 52*(5), 870-873.

Tanaka, K., Kitamura, E., Kitamura, Y., & Tanaka, T. U. (2007). Molecular mechanisms of microtubule-dependent kinetochore transport toward spindle poles. *J Cell Biol, 178*(2), 269-281. doi:10.1083/jcb.200702141

Tanaka, T. U., Rachidi, N., Janke, C., Pereira, G., Galova, M., Schiebel, E., . . . Nasmyth, K. (2002). Evidence that the Ipl1-Sli15 (Aurora kinase-INCENP) complex promotes chromosome bi-orientation by altering kinetochore-spindle pole connections. *Cell, 108*(3), 317-329.

Tang, N. H., & Toda, T. (2015). MAPping the Ndc80 loop in cancer: A possible link between Ndc80/Hec1 overproduction and cancer formation. *Bioessays, 37*(3), 248-256. doi:10.1002/bies.201400175

Tien, J. F., Fong, K. K., Umbreit, N. T., Payen, C., Zelter, A., Asbury, C. L., . . . Davis, T. N. (2013). Coupling unbiased mutagenesis to high-throughput DNA sequencing uncovers functional domains in the Ndc80 kinetochore protein of Saccharomyces cerevisiae. *Genetics, 195*(1), 159-170. doi:10.1534/genetics.113.152728

Tien, J. F., Umbreit, N. T., Gestaut, D. R., Franck, A. D., Cooper, J., Wordeman, L., . . . Davis, T. N. (2010). Cooperation of the Dam1 and Ndc80 kinetochore complexes enhances microtubule coupling and is regulated by aurora B. *J Cell Biol, 189*(4), 713-723. doi:10.1083/jcb.200910142

Tien, J. F., Umbreit, N. T., Zelter, A., Riffle, M., Hoopmann, M. R., Johnson, R. S., . . . Davis, T. N. (2014). Kinetochore biorientation in Saccharomyces cerevisiae requires a tightly folded conformation of the Ndc80 complex. *Genetics, 198*(4), 1483-1493. doi:10.1534/genetics.114.167775

Tsuji, A., Sato, Y., Hirano, M., Suga, T., Koshimoto, H., Taguchi, T., & Ohsuka, S. (2001). Development of a time-resolved fluorometric method for observing hybridization in living cells using fluorescence resonance energy transfer. *Biophys J, 81*(1), 501-515. doi:10.1016/S0006-3495(01)75717-7

Umbreit, N. T., Gestaut, D. R., Tien, J. F., Vollmar, B. S., Gonen, T., Asbury, C. L., & Davis, T. N. (2012). The Ndc80 kinetochore complex directly modulates microtubule dynamics. *Proc Natl Acad Sci U S A, 109*(40), 16113-16118. doi:10.1073/pnas.1209615109

Umbreit, N. T., Miller, M. P., Tien, J. F., Ortolá, J. C., Gui, L., Lee, K. K., . . . Davis, T. N. (2014). Kinetochores require oligomerization of Dam1 complex to maintain microtubule attachments against tension and promote biorientation. *Nat Commun, 5*, 4951. doi:10.1038/ncomms5951

Valverde, R., Ingram, J., & Harrison, S. C. (2016). Conserved Tetramer Junction in the Kinetochore Ndc80 Complex. *Cell Rep, 17*(8), 1915-1922. doi:10.1016/j.celrep.2016.10.065

van Hooff, J. J. E., Snel, B., & Kops, G. J. P. L. (2017). Unique Phylogenetic Distributions of the Ska and Dam1 Complexes Support Functional Analogy and Suggest Multiple Parallel Displacements of Ska by Dam1. *Genome Biol Evol, 9*(5), 1295-1303. doi:10.1093/gbe/evx088

Verhey, K. J., & Hammond, J. W. (2009). Traffic control: regulation of kinesin motors. *Nat Rev Mol Cell Biol, 10*(11), 765-777. doi:10.1038/nrm2782

Viswanath, S., Bonomi, M., Kim, S. J., Klenchin, V. A., Taylor, K. C., Yabut, K. C., . . . Muller, E. G. (2017). The molecular architecture of the yeast spindle pole body core determined by Bayesian integrative modeling. *Mol Biol Cell, 28*(23), 3298-3314. doi:10.1091/mbc.E17-06-0397

Wang, H. W., Long, S., Ciferri, C., Westermann, S., Drubin, D., Barnes, G., & Nogales, E. (2008). Architecture and flexibility of the yeast Ndc80 kinetochore complex. *J Mol Biol, 383*(4), 894-903. doi:10.1016/j.jmb.2008.08.077

Wang, H. W., Ramey, V. H., Westermann, S., Leschziner, A. E., Welburn, J. P., Nakajima, Y., . . . Nogales, E. (2007). Architecture of the Dam1 kinetochore ring complex and implications for microtubule-driven assembly and force-coupling mechanisms. *Nat Struct Mol Biol, 14*(8), 721-726. doi:10.1038/nsmb1274

Wei, R. R., Al-Bassam, J., & Harrison, S. C. (2007). The Ndc80/HEC1 complex is a contact point for kinetochore-microtubule attachment. *Nat Struct Mol Biol, 14*(1), 54-59. doi:10.1038/nsmb1186

Wei, R. R., Schnell, J. R., Larsen, N. A., Sorger, P. K., Chou, J. J., & Harrison, S. C. (2006). Structure of a central component of the yeast kinetochore: the Spc24p/Spc25p globular domain. *Structure, 14*(6), 1003-1009. doi:10.1016/j.str.2006.04.007

Wei, R. R., Sorger, P. K., & Harrison, S. C. (2005). Molecular organization of the Ndc80 complex, an essential kinetochore component. *Proc Natl Acad Sci U S A, 102*(15), 5363-5367. doi:10.1073/pnas.0501168102

Winey, M., Mamay, C. L., O'Toole, E. T., Mastronarde, D. N., Giddings, T. H., McDonald, K. L., & McIntosh, J. R. (1995). Three-dimensional ultrastructural analysis of the Saccharomyces cerevisiae mitotic spindle. *J Cell Biol, 129*(6), 1601-1615.

Zaytsev, A. V., Mick, J. E., Maslennikov, E., Nikashin, B., DeLuca, J. G., & Grishchuk, E. L. (2015). Multisite phosphorylation of the NDC80 complex gradually tunes its microtubule-binding affinity. *Mol Biol Cell, 26*(10), 1829-1844. doi:10.1091/mbc.E14-11-1539

Zaytsev, A. V., Sundin, L. J., DeLuca, K. F., Grishchuk, E. L., & DeLuca, J. G. (2014). Accurate phosphoregulation of kinetochore-microtubule affinity requires unconstrained molecular interactions. *J Cell Biol, 206*(1), 45-59. doi:10.1083/jcb.201312107

Zelter, A., Bonomi, M., Kim, J., Umbreit, N. T., Hoopmann, M. R., Johnson, R., . . . Davis, T. N. (2015). The molecular architecture of the Dam1 kinetochore complex is defined by cross-linking based structural modelling. *Nat Commun, 6*, 8673. doi:10.1038/ncomms9673

Zhang, G., Kelstrup, C. D., Hu, X. W., Kaas Hansen, M. J., Singleton, M. R., Olsen, J. V., & Nilsson, J. (2012). The Ndc80 internal loop is required for recruitment of the Ska complex to establish end-on microtubule attachment to kinetochores. *J Cell Sci, 125*(Pt 13), 3243-3253. doi:10.1242/jcs.104208

Zhao, G., Cheng, Y., Gui, P., Cui, M., Liu, W., Wang, W., . . . Yao, X. (2018). Dynamic acetylation of the kinetochore-associated protein HEC1 ensures accurate microtubule-kinetochore attachment. *J Biol Chem*. doi:10.1074/jbc.RA118.003844

VITA

Emily Anne Scarborough

EDUCATION

University of Pennsylvania - College of Arts and Sciences, Philadelphia, PA
- B.A. in Chemistry August 2008-May 2012
  - Relevant Coursework: Organic Chemistry, Inorganic Chemistry, Biochemistry, Advanced Organic Chemistry Lab, Physical Chemistry, Physical Chemistry Lab, Comparative Medicine, Biology of Human Disease

University of Washington – University of Washington Medical School, Seattle, WA
- Ph.D. graduate student in Biochemistry September 2013-March 2019
  - Relevant Coursework: Structural Biology, Technologies of Molecular Biology, Molecular Medicine, Topics of Molecular Medicine, Introduction to Systems Biology

RESEARCH AND PROFESSIONAL EXPERIENCE

University of Washington School of Medicine, University of Washington, Biochemistry Department, Davis Lab, *Graduate Student*, Seattle, WA
March 2014-2019
- Studying how kinetochores form load-bearing attachments to dynamic microtubules
- Uncovered a mechanism for regulation of kinetochore assembly

Perelman School of Medicine, University of Pennsylvania, Biochemistry and Biophysics Department, Shorter Lab, *Lab Manager/Research Specialist*, Philadelphia, PA
May 2012-May 2013
- Responsible for ordering all supplies for the laboratory, acted as main liaison between the laboratory and supply partners and maintained instruments and equipment
- Created all shared competent cells and common buffers/reagents
- Designed independent research project and also collaborated with other laboratories
- Continued the research project started as an undergraduate researcher

Perelman School of Medicine, University of Pennsylvania, Biochemistry and Biophysics Department, Shorter Lab, *Undergraduate Researcher*, Philadelphia, PA
March 2011-May 2012
- Used *in vitro* assays to characterize stability or misfolding of proteins implicated in human neurodegenerative diseases

PUBLICATIONS

1. Maria Armakola, Matthew J Higgins, Matthew D Figley, Sami J Barmada, **Emily A Scarborough**, Zamia Diaz, Xiaodong Fang, James Shorter, Nevan J Krogan, Steven Finkbeiner, Robert V Farese Jr & Aaron D Gitler. "Inhibition of RNA lariat debranching enzyme suppresses TDP-43 toxicity in ALS disease models." *Nature Genetics*. 2012 October.
2. Hong Joo Kim*, Nam Chul Kim*, Yong-Dong Wang*, **Emily A Scarborough***, Jennifer Moore*, Zamia Diaz*, Kyle S MacLea, Brian Freibaum, Songqing Li, Amandine Molliex, Anderson P. Kanagaraj, Rober Carter, Kevin B Boylan, Aleksandra M Wojtas, Rosa Rademakers, Jack L Pinkus, Steven A Greenberg, John Q Trojanowski, Bryan J Traynor, Bradley N Smith, Simon Topp, Athina-Soragia Gkazi, Jack Miller, Christopher E Shaw, Michael Kottlors, Janbernd Kirschner, Alan Pestronk, Yun R Li, Alice Flynn Ford, Aaron D Gitler, Michael Benatar, Oliver D King, Virginia E Kimonis, Eric D Ross, Conrad C Weihl, James Shorter & J Paul Taylor. ***Authors contributed equally to this work**. "Mutations in prion-like domains in hnRNPA2B1 and hnRNPA1 cause multisystem proteinopathy and ALS." *Nature*. 2013 March.
3. Emily M Kudalkar, **Emily A Scarborough**, Neil T Umbreit, Alex Zelter, Daniel R Gestaut, Michael Riffle, Richard S Johnson, Michael J MacCoss, Charles L Asbury & Trisha N Davis. "The inner kinetochore Mis12/MIND complex allosterically enhances microtubule attachments." *PNAS.* 2015 October.
4. **Emily A Scarborough**, Trisha N Davis, Charles L Asbury,. "Tight bending of the Ndc80 complex regulates its microtubule binding." *Under review, eLife*.